Analysis of ICRF Heating Schemes for Tokamaks using Predictive Integrated Plasma Modelling

Tomás Bensadón Oliart

Supervisor: Mervi Mantsinen

Advisor: Lluís Batet Miracle

Department of Nuclear Engineering
Universitat Politècnica de Catalunya

This dissertation is submitted for the degree of
Doctor of Nuclear Engineering and Ionising Radiations

May 2024

Me gustaría dedicar esta tesis a mis padres, Leo y Carmen, a mis abuelxs, Alberto, Carmen, Elsie y Sam, y a Sandra.

Declaration

I hereby declare that except where specific reference is made to the work of others, the contents of this dissertation are original and have not been submitted in whole or in part for consideration for any other degree or qualification in this, or any other university. This dissertation is my own work and contains nothing which is the outcome of work done in collaboration with others, except as specified in the text and Acknowledgements.

Tomás Bensadón Oliart
May 2024

Acknowledgements

Even though I am aware that very few people are going to read this, I would like to take this opportunity to thank the people that have helped me, academically and personally, over these last 4 years.

Thank you Mervi for your guidance, in a literal and figurative way, thank you for being stern when you needed to and laughing with me when we could. Thank you for sharing your wisdom and your apparently endless knowledge of physics. It makes me feel curious and small in the best possible way.

Thank you Dani for your patience, your understanding and your kindness, they're hard to find and you have plenty, I really appreciate it.

Thank you Thomas for being the only teacher I've really had during my PhD, and one I really needed. Even though we have never met in person I really care for you and I appreciate what you have done for me.

Thank you Jordi for holding my hand and taking me step by step right at the beginning, even though it would take a week for me to understand everything you said in a sentence, you treated me well and welcomed me. It amazes and scares me how smart you are and how you will decide to use it.

Thank you Martí and Todor for the conversations, walks and coffees, I hope that you're as happy with your PhDs as I've been with mine.

Thank you Mireille, Dmitriy, Ruben, Joaquín, Lluís, Olga and Xavi. This thesis would not be here without you.

This work has been carried out within the framework of the EUROfusion Consortium, funded by the European Union via the Euratom Research and Training Programme (Grant Agreement No 101052200 — EUROfusion). Views and opinions expressed are however those of the author(s) only and do not necessarily reflect those of the European Union or the

European Commission. Neither the European Union nor the European Commission can be held responsible for them.

Gracias papa por ser un ejemplo a seguir. Gracias madre por el apoyo incondicional. Gracias Miguel por el regalo de tu compañía, espero que sepas que nunca la doy por supuesta y que la agradezco cada día.

Gracias Sole por la ilusión con la que ves el mundo. Gracias Juan por saber escuchar. Gracias Diego por despertar al aventurero en mi y por vivir tu vida como lo haces, me inspiras y te admiro.

Gracias Alia por todo lo que me has enseñado, me has convertido en quien soy hoy. Gracias Juana por acompañarme y prestarme un poco de tu fuerza. Gracias Serena por tu cariño y tu sabiduría. Gracias Cris por tu energía y tus ganas de vivir. Gracias Maite por ser quien eres sin complejos. Gracias Fer por las reflexiones, aprendo más de mi en cada conversación. Gracias Simo por las risas y las aventuras, por ser mi amigo y mi hermano.

Thank you Toby for your kindness. Thank you Ed for your temperance. Thank you Alexios for your love. Thank you Julius for your care. Thank you Tareq for your esteem.

Gracias Sandra, Maider, Silvia y Errando. Aunque no signifique mucho, esto es para vosotras.

Gracias Júlia por todo. No podría haberlo hecho sin ti. Eres mi hogar y siempre te querré.

Abstract

Heating plasmas to fusion-relevant temperatures stands as a pivotal factor in magnetically confined fusion plasmas. The application of radio frequency (RF) heating through electromagnetic waves in the ion cyclotron range of frequencies (ICRF) has demonstrated its efficacy as an auxiliary method in existing fusion devices such as tokamaks. Moreover, ITER will incorporate ICRF antennas as a primary heating mechanism. Consequently, investigating various heating schemes to enhance fusion performance becomes critically significant. This thesis presented the development and assessment of theoretical models for ICRF heating at two operational devices, i.e JET and AUG, and at the ITER upcoming tokamak, with a special focus on this last one.

The main objective of this thesis was to use, for the first time, the heating code PION [1, 2] integrated into the European Transport Solver (ETS) [3, 4] to study and predict how the plasma parameters would be affected and evolve when ICRF heating was applied to ITER Pre-Fusion Power Operation (PFPO), non-active plasmas. Special attention was given to bulk ion heating, temperature enhancement, sensitivity of the ICRF power partition to minority concentration, and to the comparison between the results obtained in this thesis and the results obtained in [5–8]. The presence of ICRF physics such as Doppler effects, finite orbit width (FOW) effects and finite Larmor radius (FLR) effects were studied, and their impact was discussed. In order to prove the feasibility of using the integration of PION into ETS (PION+ETS) on currently working reactors, PION+ETS was used to study a JET baseline scenario and an AUG D plasma, even though the emphasis was on the predictions of the ITER non-active phase.

The results presented in this thesis are the first results obtained with the PION+ETS integration. Considering the dependence of ITER on every unit of auxiliary heating power that can be introduced into the plasma, it is essential to conduct both numerical and experimental investigations of this nature. The efforts in this thesis were directed towards testing and enhancing the performance of ICRF scenarios. Such endeavours play a critical role in ensuring the successful operation of ITER during its early phase. On this basis, this

thesis offered valuable insights into optimising plasma performance through various heating schemes. The results presented here serve as a guide for maximising absorption, bulk ion heating, and final temperature by appropriately configuring the ICRF heating schemes.

Of special relevance for the ITER PFPO phase was the study of fundamental minority H heating in ^{4}He plasma at 2.65 T (referred to as Scenario 1), second harmonic minority H heating in ^{4}He plasma at 1.8 T (Scenario 2), and fundamental ^{3}He heating in a three-ion scheme in H plasma at 3.3 T (Scenario 3). This analysis compared those three ICRF schemes on ITER non-active plasmas. In terms of power density absorbed, single-pass absorption (SPA) coefficients, and final thermal ion temperature, Scenario 1 presented the best alternative as compared to the other two ITER scenarios, with appropriate results obtained with the smallest minority concentration of 1.0%. Scenario 2 showed the highest electron temperature and the largest thermal ion temperature enhancement, with an interesting possibility of using only a minority concentration of 1.0% as well. Finally, the three-ion scheme in Scenario 3 presented the best bulk ion heating for a minority concentration below 0.2%. FOW and FLR effects were present in all simulations, most notably affecting Scenario 2, where the FLR effects caused the wave-particle interaction to become weak at certain energies, limiting the range of energies that the resonating ions could reach. This was the case because the main absorption mechanism in Scenario 2 was second harmonic H damping, and hence FLR effects played an important role. The relevance of the results for the ITER PFPO scenario design are discussed.

Table of contents

List of figures

List of tables

Nomenclature

$\mathbf{x}$	Volume of $\mathbf{x} = x_i x_j x_k$
$\bar{x}$	Tensor of x
$\vec{x}$	Vector of x
ε	$= \varepsilon_r \varepsilon_0 \; Fm^{-1}$ Absolute permittivity
ε_0	$\simeq 8.85 \cdot 10^{-12} \; Fm^{-1}$ Vacuum permittivity
i	$= \sqrt{-1}$ Unit imaginary number
μ	$= \mu_r \mu_0 \; Hm^{-1}$ Absolute magnetic permeability
μ_0	$\simeq 4\pi \cdot 10^{-7} \; Hm^{-1}$ Magnetic permeability
π	$\simeq 3.14$
r_L	Larmor radius
ω_c	Cyclotron frequency
AUG	Axially Symmetric Divertor Experiment Upgrade
CCFE	Culham Centre for Fusion Energy
DEMO	DEMOnstration Power Plant
ECRH	Electron Cyclotron Resonance Frequency Heating

ELD Electron Landau Damping

FLR Finite Larmor Radius

FOW Finite Orbit Widths

FPO Fusion Power Operation

GHG Greenhouse Gases

HFS High-Field Side

ICF Inertial Confinement Fusion

ICRF Ion Cyclotron Range of Frequencies

ICRH Ion Cyclotron Resonance Frequency Heating

JET Joint European Torus

LFS Low-Field Side

LHCD Lower Hybrid Current Drive

MCF Magnetic Confinement Fusion

NBI Neutral Beam Injection

PFPO PreFusion Power Operation

RF Radio Frequency

SPA Single Pass Absorption

TTMP Transit Time Magnetic Pumping

Chapter 1

Introduction

1.1 Motivation for Alternative Energy Research

The planetary boundaries framework [9] sets limits on human activities based on Earth's natural processes to ensure stability. Exceeding these limits, i.e. the nine planetary boundaries, risks destabilizing the Earth system, in which our society exists [10]. Six of these boundaries have already been surpassed [11], along with regional climate tipping points, key for planetary resilience [12]. Tackling climate change is therefore urgent. Given the significant role of the energy sector in climate change [13] and the rising energy demand [14], transitioning to sustainable energy is vital. Developing and improving clean energy technologies is therefore essential for this transition to take place on time, and for it to be conducted in a responsible and accessible way.

The demand for electricity has increased dramatically in the last 34 years, the global consumption growing more than 150% since 1990 [14]. In July 2023, fossil fuels, namely carbon and natural gas, accounted for the majority of the electricity generation, producing 51.6% of the global total. Renewable energies accounted for 30.3%, where the main contributions came from hydropower (11.4%), solar (8.0%) and wind (7.9%). Nuclear energy generated 15.6% of the total.

In 2019, almost 80% of global greenhouse gases (GHG) emissions came from the sectors of energy, transport, industry and buildings [13]. Although it is important to remember that all electricity generation technologies emit GHG at some point in their life-cycle, over 40% of energy-related CO_2 emissions are due to the burning of fossil fuels for electricity generation [15]. Renewable energy technologies are not yet ready to cope with the increasing

energy demand, due mainly to their dependency on weather forecasts and lack of power load robustness [13], even though they are now producing almost 50% more energy than 10 years ago [14]. Nuclear energy does provide a mostly clean energy source in terms of GHG emissions, however waste management and the possibility of proliferation are still an issue.

The present world energy scenario calls for an alternative, non-climate-change contributing energy source. Nuclear fusion would be a non-carbon emitting, practically unlimited energy source. It should be noted, however, that in light of current and past socio-economic, political and sustainability research [16–21], any solution to the environmental crisis that does not contemplate degrowth, i.e. radical political economic reorganization leading to reduced resource and energy use [22], is likely to fail. Nuclear fusion presents an interesting alternative to the current energy scenario for three reasons; firstly, it does not use any fossil fuels to generate energy. This does not mean that the life-cycle of a nuclear fusion power plant would be carbon neutral, but that there would be no GHG emissions associated to electricity production. Secondly, fusion is a very efficient process in terms of energy produced per unit of fuel used. In a typical fusion reaction, one nucleon potentially emits 1 MeV of energy, in comparison with the burning of gasoline, for example, which produces 1 eV of energy per atom, i.e. a million times higher [23]. Finally, it does not share the setbacks of traditional nuclear energy related to long-lived radioactively dangerous waste and the potential of a meltdown due to an uncontrolled chain reaction [24]. This is on account of two factors; i) a fusion reaction produces waste that is radioactively dangerous for $\sim$100 years, compared to a fission reaction, where the waste is radioactively dangerous for $\sim$1000 years [25], and ii) a fusion reactor needs to be constantly fuelled, as opposed to a fission nuclear power reactor, where the fuel is typically changed every 12 to 24 months.

Many of the products of the fission reaction in traditional nuclear energy are radioactive and have long half-lives. Nuclear fission uses uranium-235 (^{235}U) as the main fuel of a controlled nuclear chain reaction to achieve sustained and safe fission. This process takes place when a ^{235}U nucleus absorbs a neutron and becomes uranium-236 (^{236}U), which is an unstable isotope of uranium and will therefore eventually decay, releasing energy along the way. As mentioned above, fission waste is radioactively dangerous for $\sim$1000 years [25]. Waste-management in fusion devices presents specific challenges, different from the ones found in fission devices. The plasma-facing components of the fusion devices themselves, where the fusion reactions take place, are activated due to the neutron bombardment (this will be expanded upon in later subsections). There are also toxic products involved in fusion, both radioactive, such as, but not limited to, tritium, which decays into a helium-3 (^{3}He) nucleus, an electron and a neutrino via beta decay, and not radioactive, such as beryllium [26]. In this aspect, it is worth mentioning the JET Decommissioning and Repurposing Project

[27]. This program aims to undertake first-of-a-kind decommissioning for a tritiated fusion reactor and ancillary buildings, which represents the next stage of the life cycle of JET [28], aims to regenerate the site and provide valuable insights for the broader fusion community. This comprehensive effort, encompassing design, construction, isolations, deplanting, waste treatment, processing, and land remediation, will provide valuable insight into making future fusion devices more sustainable and cost-effective.

Therefore, nuclear fusion presents itself as a promising alternative in the transition to a sustainable energy framework, which would help substitute fossil fuels and work alongside renewable energies to cope with the increasing global electricity demand. A commercial fusion power plant is, however, not available at present, and most probably will not be in the near future either. This thesis attempts to bring clean, safe and accessible nuclear fusion energy a step closer to reality.

1.2 Outline of this thesis

The thesis research is carried out in the field of fusion plasma engineering for tokamaks. The main part of the work is developed using computer simulations. The topic of this thesis is plasma heating using radiofrequency waves. To be more precise, the modelling of ion cyclotron resonance frequency heating (ICRH), i.e. heating ions in a tokamak with electromagnetic waves in the ion cylotron range of frequencies (ICRF).

The main objective of this thesis is to use for the first time the heating code PION [1, 2] integrated into the European Transport Solver (ETS) [3, 4] to study and predict how the plasma parameters will be affected and evolve when Ion Cyclotron Resonance Frequency Heating (ICRH) is applied to ITER (*the way* in latin) [29] Pre-Fusion Power Operation (PFPO), non-active plasmas. The effect of the heating on the evolution of the plasma parameters, namely the temperature and the density, will be studied in the modelling of two devices in operation, i.e. the Joint European Torus (JET) [28] and the Axially Symmetric Divertor Experiment (ASDEX) Upgrade (AUG) [30], and in the predictions of the ITER non-active phase.

The results presented in this thesis are the first results obtained with the PION+ETS integration. Considering the dependence of ITER on every unit of auxiliary heating power that can be introduced into the plasma, it is essential to conduct both numerical and experimental investigations of this nature. The efforts in this thesis are directed towards testing and

enhancing the performance of ICRF scenarios. Such endeavors play a critical role in ensuring the successful operation of ITER during its early phase.

Following the introduction to the principles of the fusion process and RF heating in this Chapter, in Chapter 2 an overview of the basic physics of ICRF heating is presented, including wave propagation, damping mechanisms, the effect of ICRF heating on the distribution function and the models used to describe ICRF heating. Chapter 3 is dedicated to the numerical tools employed in the research. The main features of the heating code PION and the transport modelling workflow European Transport Simulator are outlined. Chapter 4 contains the main findings and results of this research. In Chapter 5 the results are discussed and the conclusions of the thesis are presented.

1.3 Fusion Process

So how does nuclear fusion work? Where does it happen? And what is the difference with nuclear fission? In this section these questions will be addressed.

Nuclear fusion takes place when two light nuclei combine to make a heavier nucleus. This process happens naturally inside of stars. The immense heat and pressure at the core of the star create the necessary conditions for light nuclei to overcome the repelling electrostatic forces, collide and fuse together. The fusion of hydrogen nuclei to form helium, through what is known as the proton-proton chain reaction, is the main source of energy of the Sun (and most main sequence stars). In its core, nuclei keep fusing to create heavier nuclei such as oxygen, carbon and neon. Larger stars can produce higher temperatures at their core and therefore synthetize heavier nuclei. The heaviest nuclei, such as uranium or thorium, are produced at supernovas. The energy released by fusion creates an outward force which counteracts the inward force of the gravitational pull. As the star consumes the available hydrogen, the energy released by fusion decreases and the gravitational pull leads to the collapse of the star. Depending on the size of the star, this collapse can lead to a white dwarf, neutron star or black hole.

On Earth, different methods are being investigated to achieve nuclear fusion in laboratory settings. The most studied techniques are inertial confinement fusion (ICF) and magnetic confinement fusion (MCF). It should be noted, however, that there are more methods to achieve fusion currently under test [31–33], but here the main focus is given to MCF and ICF. The most extended approach to achieve nuclear fusion by both of these techniques is through the deuterium-tritium (D-T) reaction

$$D + T \rightarrow^4 He(3.5MeV) + n(14.1MeV)$$

which produces ^{4}He and a highly energetic neutron. The total reaction energy is given by the sum of the values in brackets. An alternative approach, developed by e.g. [34] in a field reversed configuration plasma, uses D and ^{3}He as fuel. The D-^{3}He reaction

$$D + {}^3He \rightarrow^4 He(3.7MeV) + p(14.7MeV),$$

produces ^{4}He and a highly energetic proton. This ^{4}He is a charged ion that can be used to generate electricity directly by induction [34].

These reactions are of interest mainly due to two factors: the cross-section and the temperature. The cross-section is a measure of the probability of a certain process taking place; the higher the cross-section the higher the probability. The temperature needed for these reactions to take place is also a determining factor, due to the challenge of achieving very high temperatures for a sustained amount of time. Figure 1.1 shows the cross-section and centre-of-mass kinetic energy for the fusion reaction pathways described above and some other examples. As it can be seen, the D-T reaction combines a high energetic yield and a high cross-section with a moderately high energy needed in the centre-of-mass reference frame. This makes D and T the most commonly used reactants in fusion experiments [23].

1.4 Brief Description of a Plasma

Reaching fusion relevant conditions, a temperature of the order of about $\sim$10 keV or above is typically needed, which is equivalent to $\sim$100 million K. At such temperatures, particles become ionised. The state of matter where all electrons and nuclei in a gas are free is known as plasma. The behaviour of a plasma is no longer dominated by short-ranged, collisional Coulomb forces, but by long-range, collective effects, such as electric and magnetic forces. All the physics described in this thesis consider matter to be in a plasma state.

1.5 On the Importance of Modelling

All of the work presented in this thesis is carried out through the modelling of fusion processes and computational simulations. Before delving further into the intricacies of fusion and

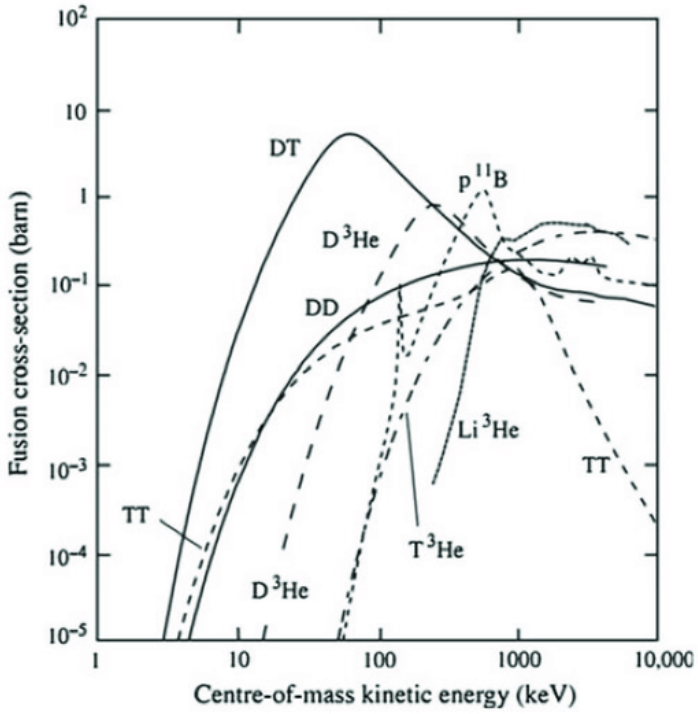

Fig. 1.1 *Cross sections of the different fusion reaction pathways [35].*

how it can be carried out in laboratory settings, a brief note on the importance of physical modelling.

Modelling and simulations are integral to comprehending complex physical processes and advancing scientific knowledge. Models serve as tools for simplification of intricate natural phenomena involving numerous variables and interactions, enabling a more manageable representation of underlying mechanisms. They facilitate the prediction of system behaviors under different conditions, allowing the testing of hypotheses and refining theories based on observed outcomes. Beyond cost-time efficiency and allowing access to extreme or inaccessible environments, simulations offer a safe and iterative approach to experimentation, refining models as more data becomes available. Simulations are instrumental in the design and testing of new technologies, contributing to the optimization of structures and devices. Overall, modelling and simulations have become indispensable tools for scientific and technological development, providing a deeper understanding of the physical world.

Regarding fusion, the dynamics of the plasma in fusion machines pose a considerable challenge due to the complexity of a hot, magnetized plasma that is far from thermal equilibrium and possesses numerous degrees of freedom. The interdependence of physical quantities significantly influences the evolution of each variable, up to a certain point. Therefore, the

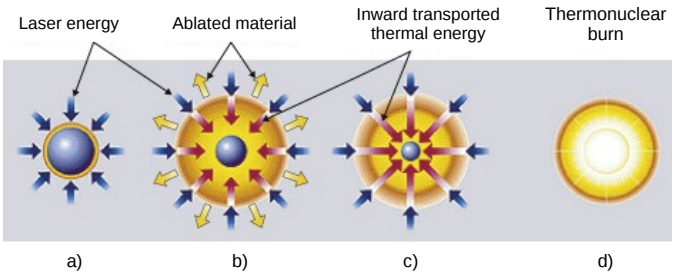

Fig. 1.2 *The four stages of a fusion process in an inertial confinement fusion capsule [37].*

bridge between modelling and experimental approaches is essential in understanding fusion-relevant scenarios. Experimental evidence aids in identifying key parameters for inclusion in models, as attempting to capture every individual aspect of charged particle dynamics in computational models would be impractical due to prohibitively long run times. Consequently, models must make assumptions to produce results in a reasonable time. However, modelling provides a profound understanding of plasma behavior, offering valuable insights and guiding exploration along potential experimental pathways [36].

1.6 Fusion Methods

As mentioned in Section 1.2, two of the methods through which energy from fusion can be achieved in laboratory settings are ICF and MCF. In this subsection an overview of both is given, as well as a description of the main magnetic confinement device types, i.e. tokamaks and stellarators.

Inertial confinement fusion (ICF) attempts to achieve fusion through the heating and compression of a fuel pellet, which acts as a target, using highly energetic beams, which act as an energy driver [38]. High-energy beams of electrons or ions can be used, although laser beams are most commonly used. The goal of ICF is to compress the pellet to such an extent that fusion conditions are achieved at its core. This is achieved by irradiating the surface of the pellet from all sides, increasing its temperature and producing a plasma envelope that surrounds the target. The plasma then expands rapidly outwards, producing an inward, rocket-like force in the form of shock waves that compresses the fuel. This outward plasma jet causes the pellet to accelerate inwards and implode, increasing the density dramatically and achieving the thermonuclear conditions necessary for fusion. Figure 1.2 shows an schematic of the four stages of ICF described above; a) laser heating of the outer layer, b) compression of the capsule by the ablation of the outer layer, c) density and temperature for ignition

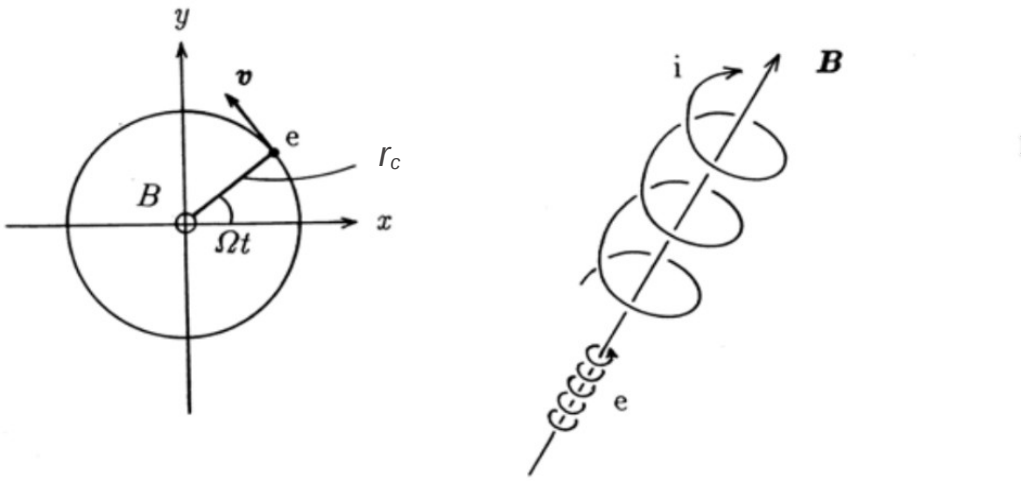

Fig. 1.3 *Larmor motion of a charged particle in a magnetic field [39].*

reached in the core, and d) rapid spread of the fusion reaction through the compressed fuel [37].

Magnetic confinement fusion (MCF) attempts to achieve fusion by confining the fuel in the form of a plasma. A plasma is composed of free electrons and free ions whose motion can be manipulated by external fields. As the temperature increases, the plasma naturally attempts to expand. When an external magnetic field is applied, the charged particles experience a Lorentz force perpendicular to their velocity and to the magnetic field [39]. Consequently, charged particles spiral along the magnetic field lines, following helical trajectories, in what is known as cyclotron or Larmor motion. This is shown in Figure 1.3, where B is the background magnetic field, Ω is the angular velocity, r_c is the Larmor radius and $\boldsymbol{v}$ (or $v_\perp$) is the velocity perpendicular to the magnetic field. The Larmor radius is given by $r_c = v_\perp/\omega_c$, where ω_c is the so-called cyclotron frequency. The cyclotron frequency is given by $\omega_c = Z_s eB/m_s$, where $Z_s e$ and m_s are the charge (which includes the sign, i.e. negative for electrons and positive for ions) and the mass of the particles species s, respectively. It follows that the motion of particles is confined by magnetic field lines until it is perturbed by collisions with other particles, the wall or other mechanisms [39] (fields gradients, toroidal Alfvén eigenmodes [40], etc). MCF research has developed two main device types that are capable of confining the particles in the plasma by producing twisted field lines that bent over themselves and do not intersect at any point: stellarators and tokamaks.

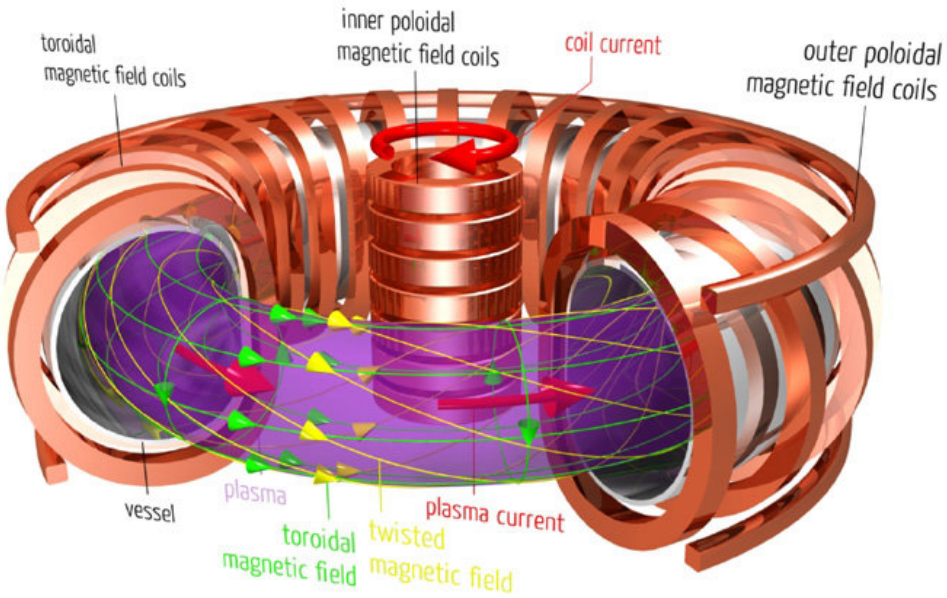

Fig. 1.4 *Main scheme of a tokamak. Courtesy of the Max Planck Institute for Plasma Physics.*

The tokamak was first conceived by Soviet physicists in the 1950s. It is a toroidal device which has axial symmetry. As is shown in Figure 1.4, it is constituted by a toroidal plasma enclosed by a large toroidal magnetic field (B_T) generated by coils situated outside the vacuum vessel. Additionally, a smaller poloidal magnetic field ($B_\theta << B_T$) is created by a toroidal current (I_p) through the plasma [26]. The central solenoid is used to drive said electric current in the plasma by transformer principle, and therefore the tokamak operation is pulsed. External toroidal coils create a magnetic field to shape and position the plasma. The poloidal magnetic field prevents outward radial particle drift, ensuring radial equilibrium within the plasma [23]. Since the toroidal magnetic field coils are closer to each other in the inside of the torus, the toroidal magnetic field is not homogeneous through the entire volume of the plasma, but varies as $B_T \propto 1/R$, where R is the radial distance to the torus axis. The gradient of the magnetic field ∇B is the cause of several particle drifts which are the source of certain confinement complications [23, 26].

This layout allows the confinement of the particles and prevents them from drifting outwards. The main innovation of the tokamak consisted on increasing the twist of the field in comparison to its predecessors, thus increasing the number of times that the particles transit from the inside to the outside of the toroidal section in each orbit. The ratio of twists to magnetic field lines is known as the safety factor. This innovation considerably reduced the instabilities in the plasma and allowed tokamaks to be the leading device in MCF research.

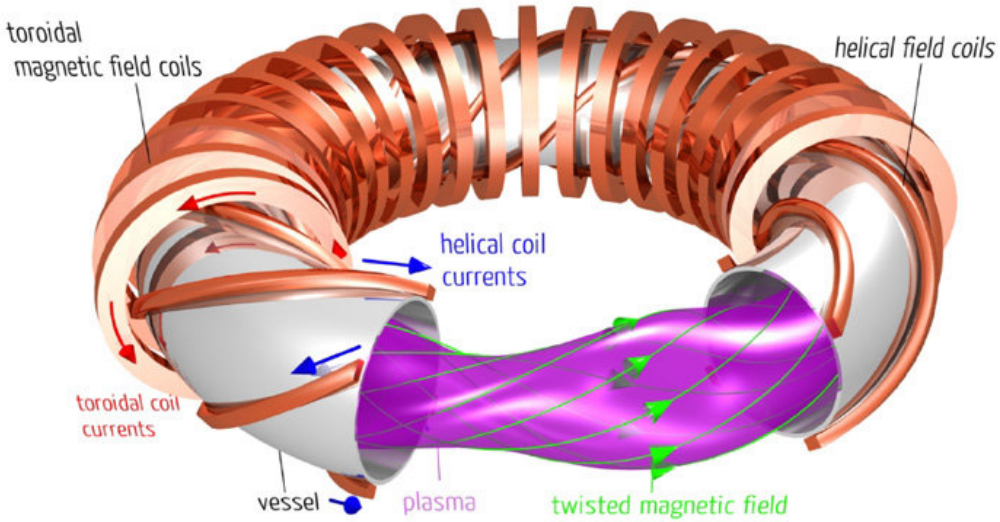

Fig. 1.5 *Main scheme of a stellarator. Courtesy of the Max Planck Institute for Plasma Physics.*

The stellarator was first conceived by Lyman Spitzer in 1951 at Princeton University. It is a toroidal device which has no axial symmetry and it is not a pulsed machine, i.e. it can work continuously. As can be seen in Figure 1.5, it is constituted by toroidal magnetic field coils and helical field coils [41]. The combined induced magnetic field also results in twisted magnetic field lines, although in this case the twist is achieved through the mechanical arrangement of the helical coils and not through an induced electrical plasma current. The layout of the stellarator addresses the unwanted particle drift through its mechanical design, and the lack of induced current in the plasma reduces the potential for instabilities and allows longer operation times for the machine. However, losses due to energy transport are generally larger in stellators and their design is more complicated than that of tokamaks, hence there have been fewer experiments in stellarators than in tokamaks so far.

The main goal of fusion research is to achieve electricity-producing fusion power stations that can provide energy reliably, safely and efficiently. Significant advances have been made in the technological development of the MCF devices for that purpose. The long-term purpose of fusion research is to achieve ignition ($Q \to \infty$). Here we have used the Q-factor, which stands for the ratio of fusion power produced to the power required to maintain the plasma in a steady state. Ignition takes place when the plasma uses its own energy to keep producing fusion, leading to self-heating and eventually to a self-sustained reaction. Until

recently, no device had ever achieved $Q \to 1$. However, an inertial fusion experiment carried out on August 8, 2021 at the National Ignition Facility generated over a megajoule of fusion yield [42]. This was the first time that the fusion breakeven had ever been surpassed. It should be noted, however, that this is true if only the beam energy is taken into account, rather than the energy required for the laser source to produce the beam, in which case $Q < 1$.

1.7 Fusion Reactors

The work in this thesis focuses on fusion experiments carried out in tokamaks, i.e. on the modelling of AUG, JET and ITER. Of these three devices, AUG is still in operation, JET has recently ended its operations [43], and ITER is under construction. The main difference between these tokamaks, as can be seen in Table 1.1, is in their size; ITER will be twice the size of JET, whilst JET is almost twice the size of AUG. In this thesis, special attention is given to ITER modelling and predictions, as physical and technological development is still needed before it starts operating. A brief overview of the main parameters and background information of these fusion tokamak reactors is given in this section. Their parameters and dimensions are summarised in Table 1.1.

Table 1.1 *Fusion reactors main parameters and dimensions. The major radius (R_0) and minor radius (r) are defined in Figure 1.6.*

Parameters	ITER	JET	AUG
Major radius R_0 (m)	6.2	2.96	1.65
Minor radius r (m)	2	1.25-2.10	0.5-0.8
Toroidal magnetic field B_0 (T)	5.3	3.45	3.1
Plasma current I_p (MA)	15	4.8	1.6
Fusion power (MW)	400-500	16	-

ITER [29] is the largest tokamak nuclear fusion reactor in the world. It is being built in the south of France. The aim is for ITER to maintain $Q > 5$ and to reach $Q \to 10$, demonstrating the feasibility of fusion power and of a ten-fold gain of plasma heating power. The operations at ITER will follow a staged approach, according to the ITER Research Plan [29]; starting with two Pre Fusion Power Operation (PFPO I and II), or non-active phases. During this stage, the objective is to assess the behavior of the plasma and its fundamental properties as the complete heating capability becomes accessible. The aim is to conduct these tests in a less harsh environment compared to that of a burning plasma. To prevent premature activation of the machine, the primary gasses used in this initial phase will be H and He instead of D and T. The next stage is the Fusion Power Operation (FPO) phase, where a

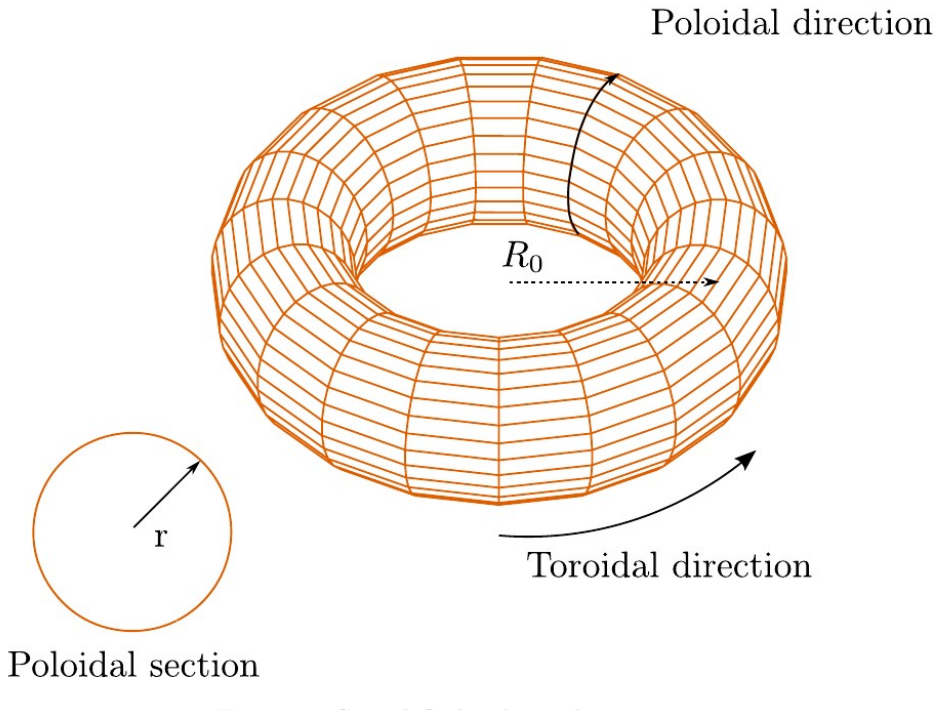

Fig. 1.6 *Simplified tokamak geometry. R_0 stands for the major radius and r for the minor radius [44].*

transition will be made to D, T and D-T plasmas. It should be noted that the ITER Research Plan is currently under review. The technological and physical knowledge and experience obtained through the expected success of ITER will then be used to build the DEMOnstration Power Station (DEMO), the next largest fusion reactor and the first to produce electricity, which will be, in principle, the last step before a commercial station.

The Joint European Torus (JET) [28] was the largest working tokamak in Europe until December 2023 [43]. It is located at the Culham Campus, near Oxford, United Kingdom, and operated by the United Kingdom Atomic Energy Authority (UKAEA). It began operating in 1983 and it currently holds the record for the highest energy achieved through sustained fusion at 69 megajoules [45], breaking its own previous 2022, 59 megajoules record [46]. For this latest 2023 record, they used a D-T fuel mix in a six second plasma pulse and only 0.21 milligrams of fuel. The JET tokamak is the main predecessor of ITER, and some of the concepts for the ITER design have been tested at JET, such as the beryllium-tungsten wall.

The Axially Symmetric Divertor Experiment (ASDEX) Upgrade (AUG) [30] is located at the Max Planck Institute for Plasma Physics, in Garching, Germany. It started operating in 1991, it is, compared to ITER and JET, a midsize reactor, and is equipped with a tungsten first wall. The essential plasma properties are matched to the conditions in ITER to contribute to the preparation for its physics base.

1.8 Plasma Heating Methods

As it was explained in Sections 1.3 and 1.4, in order for fusion to take place, extremely high temperatures of the order of $\sim 10^8$ K need to be reached. There are three methods to heat a magnetically confined plasma: Ohmic heating, neutral beam injection (NBI) and radio frequency (RF) heating. In this section, an overview of these heating methods, their structure and basic physics is given.

In general, Ohmic heating takes place when a current is induced in a conductor. The induced electric current produces heat proportional to the square of the current intensity and the resistivity. Magnetically confined plasmas are subject to Ohmic heating due to the induced plasma current. However, the resistivity of the plasma decreases as its temperature increases, hence Ohmic heating can only increase the plasma temperature to a certain extent, and further heating is required for fusion conditions to take place. This is achieved via NBI and RF heating.

NBI consists of high energy neutral particles being injected into the plasma to increase the overall temperature. Firstly, ions are accelerated using charged plates. Then, the ions are re-neutralized by adding opposite charged particles. Lastly, the high energy neutral beam is tangentially injected into the device across the magnetic field. These particles are ionized inside the plasma due to the charge exchange, and transfer their energy to the plasma particles through Coulomb collisions. As a result of this ionization, they are also confined by the magnetic field and can remain in the plasma and continue to transfer their energy.

RF heating consists of producing high-frequency electromagnetic waves and launching them into the plasma from an external source and through a launcher. The energy of the wave is subsequently transmitted to the plasma through different mechanisms, depending on the RF method. The kinetic energy of the plasma ions increases due to the absorption of the electromagnetic radiation. The frequency of the wave is chosen depending on the resonant frequency of interest. The main RF methods are ion cyclotron resonance heating (ICRH), electron cyclotron resonance heating (ECRH) and lower hybrid current drive (LHCD) [48].

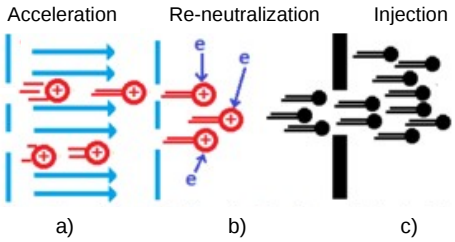

Fig. 1.7 *The three stages of the injection of neutral beam particles into the plasma in NBI heating [47].*

1.8.1 RF Heating Types and Structure

All RF heating devices share a common basic design. They are constituted by a high-voltage power supply, which in turn drives a RF source. The source sends electromagnetic waves through a transmission path to a launcher, where they are launched into the plasma. The types of source, transmission line and launcher vary depending on the RF method employed. They are presented below.

The source type depends on the targeted resonant frequency. As it was explained in Section 1.6, the cyclotron frequency of a certain particle in a magnetic field B is given by $\omega_c = Z_s eB/m_s$. It can be seen that, for a given B, the frequency depends on the mass, and, therefore, ions and electrons will have different cyclotron frequencies.

In the case of ECRH, the cyclotron frequency of electrons is targeted, which usually lies in the $f_{ce} \sim 150$ GHz scale. The source needed for this frequency is a gyrotron, which generally generates frequencies in the $f \sim 10 - 300$ GHz range, corresponding to the sub millimetre waves scale. Further optimization of gyrotrons remains an active area of research, with considerable efforts directed towards this goal [49].

In the case of ICRH, the ion cyclotron frequency is targeted, which, due to the large mass of the ions, results in a smaller value, usually in the $f_{ci} \sim 50$ MHz scale. The source needed in this instance is a high power vacuum tube, which produces frequencies in the $f < 100$ MHz range.

Lastly, LHCD uses lower hybrid waves that propagate around the torus, dragging electrons that produce the current drive. This waves lie in an intermediate frequency, commonly in the $f_{lh} = 3$ GHz scale. The source used to produce this type of wave is a klystron, which generates frequencies in the $f \sim 1 - 10$ GHz range, corresponding to the microwave regime. Both high power vacuum tubes and klystrons are sufficiently developed technologically to be available for steady state operation [23].

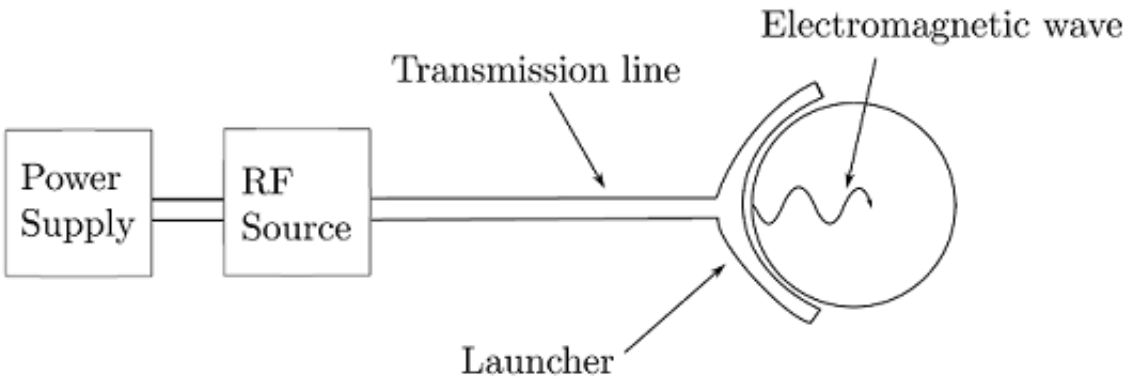

Fig. 1.8 *Main scheme of a RF launching structure [23].*

There are several factors that should be taken into consideration when choosing a transmission line, such as attenuation, impedance matching or power handling capability [50]. In order to select the dimensions of the transmission line, the frequency of the electromagnetic wave that it transports from the source can be compared to the characteristics of the transmitting circuit. There are several ways in which the transmission can be performed. Here we will consider in more detail the standard electrical wire, the two-wire transmission line and waveguides. A two-wire transmission line should be used when the wavelength of the wave meets the following requirement:

$$L \geq \lambda \gg L_t$$

where L is the length of the transmission path, λ is the wavelength and L_t is the transverse dimension of the transmission line. In the case of ICRH, for $f_{ci} \sim 50$ MHz, we obtain $\lambda = c/f = 6$ m, where c is the speed of light, which satisfies the inequality above. In this instance, the wave does not have any component in the direction of propagation and thus propagates as a pure transverse electromagnetic wave.

Waveguides should be used when the electromagnetic wave satisfies the following requirement:

$$L \gg \lambda \sim L_t$$

As mentioned above, ECRH commonly uses waves in the $f_{ce} \simeq 150$ GHz scale, which corresponds to $\lambda = c/f = 2$ mm, satisfying the inequality. This is also the case for LHCD, as $f_{lh} = 3$ GHz corresponds to a wavelength $\lambda = c/f = 10$ cm, also appropriate for this

transmission method. Even though both ECRH and LHCD utilize waveguides, ECRH requires a waveguide with a smaller cross section compared to LHCD.

Lastly, the launcher acts as an interface between the transmission line and the plasma. The type of launcher should also be chosen depending on the frequency of the wave it transmits [26]. In the case of ICRH, waves are launched using an antenna situated inside of the vacuum chamber. In the ECRH case they are launched through open guides, and a RF mirroring system is used to steer the beam. LHCD utilizes a waveguide array. For geometric accessibility reasons, all of the described methods strongly prefer the waves to be launched from outside of the plasma. However, this is not the only requirement, and each launcher presents specific issues.

The ICRH antenna needs to be in close proximity to the plasma edge, because otherwise the waves do not couple strongly to the plasma. This proximity is the source of several issues. In order to be able to launch large amounts of power into the plasma, high voltages are required. These voltages can cause plasma breakdown and arcing, which are undesirable effects. It is worth noting that, in the same way as the RF source determines the frequency of the wave, the geometric structure of the antenna determines the parallel wavenumber $k_{\|}$.

Regarding LHCD, the launching structure also needs to be close to the plasma in order to obtain good coupling. This requirement, combined with the small size of the transverse dimensions of the waveguide, poses a difficulty to spread the RF power over an area large enough that high-voltage breakdowns do not take place. In order to address this problem, a large number of waveguides need to be used in the launching array. Furthermore, the waveguides require an isolated vacuum interface between themselves and the plasma. This isolation can be achieved by inserting sealed windows at the end of each waveguide in the array. This windows must be made of a material that is able to sustain large amounts of RF power travelling through. The material cannot absorb or reflect said power, as this could lead to thermal stress or loss of efficiency. Synthetic diamonds, such as Chemical Vapor Deposition diamonds [51], have been successfully used for this purpose in fusion conditions [52, 53].

1.8.2 Ion Cyclotron Resonance Frequency Heating (ICRH)

The heating of tokamak plasmas using ICRF heating is the main focus of this thesis. The basic mechanism by which the plasma absorbs energy from ICRF waves is through a wave-particle resonance. This resonance takes place when the Doppler shifted frequency of the

ICRF wave is equal to an exact harmonic of the ion cyclotron frequency. This condition is described by

$$\omega = k_{\|} v_{\|} + l\omega_c \qquad l = 0, 1, 2, ... \tag{1.1}$$

where ω is the frequency of the wave, $k_{\|}$ is the wavenumber parallel to the background magnetic field, $v_{\|}$ is the parallel velocity, ω_c is the ion cyclotron frequency and l represents the harmonics of the wave. The $l = 0$ resonance is known as Landau damping, the $l = 1$ resonance corresponds to the fundamental and the $l = 2$ to the second harmonic. As mentioned in Section 1.6, the cyclotron frequency is given by $\omega_c = Z_s eB/m_s$, where B is proportional to the inverse of the radial distance from the tokamak axis, R, as $B \propto 1/R$. Due to this correlation, the exact location where the wave is absorbed can be selected, which allows heating precise areas of the plasma.

The capacity of a wave to produce an effective wave particle resonance depends on the frequency and the polarization of said electromagnetic wave. Polarization indicates the orientation of the electric field. A more detailed description of polarization is discussed in Subection 2.1.3. Circularly polarized waves have an electric field component that rotates in a plane as the wave propagates. Depending on the direction of this rotation, the wave can have either right circular polarisation (E_-) or left circular polarisation (E_+). In fusion physics, polarization can also describe the wave in terms of the electric field components that are parallel to the background magnetic field. If the parallel component is zero ($E_{\|} = 0$) then the wave is extraordinary and corresponds to the X mode. If the component is non-zero ($E_{\|} \neq 0$), then the wave is ordinary and corresponds to the O mode. Waves in the ICRH range of frequencies have negligible parallel electric field components and are thus considered to be in X mode.

Therefore, ICRH waves are constituted by an electric field component perpendicular to the background magnetic field that is, at the same time, constituted by a left circularly and a right circularly polarised component. Ions rotate in the same direction as the left component, hence the wave particle resonance is proportional to the amplitude of the left circularly polarised component of the wave, E_+. The interaction between the E_+ field vector and the particle velocity vector changes between the fundamental ($l = 1$) and the harmonic ($l > 1$) ion cyclotron resonance.

In the case of the fundamental resonance, the orientation of the E_+ vector remains at a constant angle of the velocity vector for the complete duration of the ion cyclotron period. This means that the particle will undergo net acceleration, mainly in the perpendicular velocity

direction. This acceleration will often modify the high-energy part of the velocity distribution function, creating what is referred to as a high-energy *tail* (this will be expanded upon in Section 2.3). Assuming that the perpendicular wave vector is $k_\perp \simeq 0$ and $v_\perp = v_x + iv_y$, the solution to the velocity evolution differential equation is

$$v_\perp = v_0 e^{-i\omega_c t} + \frac{eE_+}{m} t e^{-i\omega_c t} \tag{1.2}$$

where v_0 is the initial velocity and m is the mass of the ion. The first and second terms are always in phase, resulting in net acceleration.

To explain the resonance at the harmonics, let us consider the case of the second harmonic ion cyclotron resonance ($l = 2$). In this case, the orientation of the E_+ vector with respect to the velocity vector changes every period. The particle will therefore be accelerated over half of its trajectory across the orbit and decelerated over the other half. Whether the particle is accelerated or decelerated will depend on the variation of the wave amplitude in the direction perpendicular to the background magnetic field lines. If the amplitude is constant in space and only changes in time, the acceleration and deceleration will be equal and no net acceleration will take place. If, however, the amplitude varies across the orbit, then net acceleration can take place. The change in space of the wave amplitude depends on the Larmor radius r_c. The Larmor radius, as defined in Section 1.6, is the radius with which the ion orbits around the magnetic field lines in the ion cyclotron motion. The resonance is subject to the Larmor radius being comparable to the perpendicular wavelength $\lambda_\perp$. The perpendicular wavelength refers to the wavelength associated with the perpendicular wave vector $k_\perp$ of the wave. Absorption at the harmonics of the ion cyclotron frequency only takes place if the division of r_c by $\lambda_\perp$ is finite. Absorption in this regime is therefore considered a finite Larmor radius (FLR) effect.

Let us consider a plasma composed of ion species X. Heating at the fundamental X harmonic results in a wave with $E_+ = 0$ at the point of resonance, thus the plasma-wave coupling vanishes due to this opposite polarisation. Heating at the second harmonic leads to a wave with $E_+ \neq 0$ and satisfactory heating. However, this type of heating is not as reliable as desired due to a sensitive dependence on temperature and density. Another option is the so called minority heating. This method consists on inserting a small population of non-X particles into the plasma (Y). The fundamental heating of the minority Y species is then targeted. The opposite polarisation issue is resolved as the actual polarisation of the plasma is determined by the majority X species. The minority species Y is thus heated and the energy is transferred to the bulk X plasma through Coulomb collisions. The most efficient heating

takes place when the cyclotron frequency of the minority species Y is higher than that of X. Minority heating is further discussed in Subsection 2.1.7.

It should be noted that ICRF heating is anticipated to be the only auxiliary heating method in ITER with the capability to predominantly heat bulk ions. A large bulk ion heating fraction is important for an improved control over the plasma ramp-up, for access to a regime with good confinement as well as for improved steady-state fusion performance. In contrast, alternative methods like ECRH and NBI, which utilize ions in the MeV energy range, are primarily expected to contribute towards electron heating. This unique capability of ICRF heating to focus on bulk ion heating distinguishes it as a crucial heating and current drive (H&CD) method for ITER. Consequently, ICRF plays a pivotal role in establishing the essential conditions for sustained and controlled fusion reactions within ITER, contributing significantly to overall plasma performance.

The modelling of ICRF is essential for the development of ITER, as it serves as a vital tool for predicting and understanding the behavior of plasmas under ICRF heating scenarios. Through comprehensive modelling, the complex interactions between ICRF waves and the ions in the plasma can be simulated, enabling the optimization of heating performance and the identification of potential challenges. The modelling process is necessary to design efficient ICRF heating schemes tailored to the specific requirements of the ITER tokamak, providing insights into the physics of e.g. power deposition, collisional equipartition and plasma temperature evolution. This predictive capability contributes to guiding experimental setups, refining operational parameters and enhancing overall performance, all of which work towards ensuring the success of ICRF heating as a key component in the quest for controlled fusion energy.

Chapter 2

The Physics of Ion Cyclotron Resonance Frequency Heating

At the end of Chapter 1 the heating of magnetically confined plasmas in tokamaks using ICRF waves was introduced. But, how do these waves propagate through the plasma? How do they transfer their energy to the particles in the plasma? And how can we effectively model this process in order to carry out computational simulations that properly describe ICRF heating? In this Chapter the propagation of a wave in a plasma will be explained and the basic physics and formalisms of ICRF will be provided. The first step is to describe the plasma through the Cold Plasma model and to introduce the basic concepts of wave propagation, i.e. resonances and cutoffs, polarization, mode conversion, accessibility and ICRF heating schemes. The next step is to understand how the wave is absorbed by the plasma. Ion and electron damping mechanisms, as well as basic notions of the distribution function, are explained in the following subsections. Finally, an account of the modelling of the power deposition and the evolution of the ICRF distribution function is given.

2.1 Basic Concepts of Wave Propagation

2.1.1 The Cold Plasma Model

Let us start by using a simplified model to describe the plasma and the propagation of the wave. In the cold plasma approximation, we assume that the thermal velocity of the particles is much lower than the phase velocity of the waves. The cold plasma model provides a good enough approximation to the physics of wave propagation. However, there are some critical

regions where this approximation breaks down. This happens in the resonance regions, where the phase velocity of the waves tends to zero. The cold plasma model does nevertheless provide an appropriate description of the propagation of wave energy to the resonance region. Therefore, this model can be used to determine the accessibility of the resonance regions for waves in the ion cyclotron (IC) range of frequencies. This accessibility will be described further on.

The propagation of a wave in a plasma is described by the general wave equation [26]

$$\nabla \times \nabla \times \mathbf{E} = -\frac{1}{c^2}\frac{\partial^2 \mathbf{E}}{\partial t^2} - \mu_0 \frac{\partial \mathbf{j}}{\partial t} \tag{2.1}$$

where $\mathbf{E}$ stands for the wave electric field, c is the speed of light and $\mathbf{j}$ is the current. Applying the Fourier analysis in space and time, we obtain a reduced version of the wave equation

$$-\mathbf{k} \times \mathbf{k} \times \mathbf{E} - \frac{\omega^2}{c^2}\varepsilon \cdot \mathbf{E} = i\omega\mu_0 \mathbf{j}_A \tag{2.2}$$

where $\mathbf{k}$ is the wave vector, ω is the wave frequency and $\mathbf{j}_A$ is the external antenna current. ε stands for the dielectric tensor, which describes the response of the plasma to the wave electric field. We obtain the dispersion relation by solving for the non trivial solution of the wave equation

$$det[n^2(\hat{\mathbf{n}}\hat{\mathbf{n}} - I) + \varepsilon] = 0 \tag{2.3}$$

where I is the identity matrix and $\hat{\mathbf{n}}$ stands for the refraction index, which is given by $\hat{\mathbf{n}} = \vec{n}/|n|$, where $\vec{n}$ is related to the wave vector as $\vec{n} = \vec{k}c/\omega$.

The dielectric tensor in the dispersion relation above can be expressed in the cold plasma model as [54]

$$\varepsilon = \begin{pmatrix} \varepsilon_\perp & -i\varepsilon_{xy} & 0 \\ i\varepsilon_{xy} & \varepsilon_\perp & 0 \\ 0 & 0 & \varepsilon_\parallel \end{pmatrix} \tag{2.4}$$

Here the elements of the dielectric tensor are expressed in a geometry such that the x-axis goes along the radial direction of the tokamak, the y-axis goes along the poloidal direction and the z-axis goes along the direction of the background magnetic field. The elements of the dielectric tensor are given by

$$\begin{aligned}
\varepsilon_{\perp} = \varepsilon_{xx} = \varepsilon_{yy} &= 1 - \sum_s \frac{\omega_{ps}^2}{\omega^2 - \omega_{cs}^2} \\
\varepsilon_{xy} = -\varepsilon_{yx} &= -\sum_s \frac{\omega_{ps}^2 \omega_{cs}}{\omega(\omega^2 - \omega_{cs}^2)} \\
\varepsilon_{\parallel} = \varepsilon_{zz} &= 1 - \sum_s \frac{\omega_{ps}^2}{\omega^2}
\end{aligned} \tag{2.5}$$

where $\omega_{cs} = Z_s eB/m_s$ is the cyclotron frequency, $\omega_{ps} = n_s(Z_s e)^2/\varepsilon_0 m_s$ is the plasma frequency and n_s, $Z_s e$ and m_s are the density, charge and mass of particle species s. The charge $Z_s e$ includes the negative sign for electrons and positive for ions. The summation is over all particle species.

We now take into account three conditions; (i) the wave frequency can be approximated to the IC frequency, (ii) the IC frequency is much smaller than the ion plasma frequency, and (iii) the electron plasma frequency and cyclotron frequency are much larger than that of ions. Therefore, the expression for the parallel component of the dielectric tensor above can be approximated to $\varepsilon_{\parallel} \simeq -\omega_{pe}^2/\omega^2 \simeq -\omega_{pe}^2/\omega_{ci}^2 \propto O(m_i^2/m_e^2)$. We know that $\varepsilon_{\perp}$ and ε_{xy} are of the order of (m_i/m_e), so $\varepsilon_{\parallel}$ will be much larger than the other two elements.

We can now find the solutions of the determinant defining the dispersion relation. There exist many solutions for this determinant, each of these solutions is called a mode, and each mode represents a different type of wave with a different perpendicular refractive index. For the conditions defined above, the dispersion relation gives two cold plasma modes; the slow wave or shear Alfvén (equation 2.6) and the fast wave or compressional Alfvén (equation 2.7). The squared perpendicular refractive indexes for the slow and fast waves are given, respectively, by

$$n_{\perp}^2 = \frac{\left(\varepsilon_{\perp} - n_{\parallel}^2\right)\varepsilon_{\parallel}}{\varepsilon_{\perp}} \tag{2.6}$$

$$n_{\perp}^2 = \frac{(\varepsilon_{\perp} - n_{\parallel}^2)^2 - \varepsilon_{xy}^2}{\varepsilon_{\perp} - n_{\parallel}^2} \tag{2.7}$$

2.1.2 Resonances and Cutoffs

After determining the two modes propagating in the IC range of frequencies in Subsection 2.1.1, we must evaluate their capability to reach the wave-particle resonance before reaching specific regions in the plasma with undesirable changes in energy or wave properties. In the cold plasma limit, plasma surfaces where the square of the perpendicular refractive index $\hat{n}^2$, or equivalently the wave vector $\vec{k}$, tends to infinity or zero, define resonance and cut-off regions, respectively.

Surfaces where $n_\perp^2 \to 0$ are known as cutoff regions, where the wave transforms from evanescent to propagative or vice versa. Here, the phase velocity of the wave goes to infinity and the group velocity remains finite. Regions where $n_\perp^2 < 0$ cannot support wave propagation, and the waves that go through this region decay exponentially. These are known as evanescent regions. When the evanescent region is large, the wave is totally reflected. However, if the evanescent region is small enough, some of the power can tunnel through this region and propagate on the other side.

Surfaces where $n_\perp^2 \to \infty$ are known as resonance regions, where the cold plasma model approximation fails. In the hot plasma model, where kinetic effects are taken into account, the propagating wave is converted into another wave at the resonance through mode conversion. Where the mode-converted power is absorbed will be determined by the propagation characteristics of the new wave. In the resonance regions, both the phase and group velocity tend to zero.

Looking at the perpendicular refractive indexes of the slow and fast waves defined in Subsection 2.1.1 above, we see that neither of them diverge at the cyclotron frequencies and their harmonics, therefore no wave resonance will take place. However, as the resonances at the cyclotron frequencies and their harmonics take place in the particle motion and not in the wave field, they are known as particle resonances.

2.1.3 Polarization

Following with the basic concepts of wave propagation, we arrive at polarization. As it will be explained later on, understanding wave polarization is crucial when aiming to optimize ion absorption.

Electromagnetic polarization refers to the direction in which the electric field oscillates. In optics it is defined as the ratio of the perpendicular components of the electric field to the wave vector. Waves exhibiting an electric field component parallel to the wave vector are

termed longitudinal waves, commonly observed in plasmas. For a typical wave propagating in the direction perpendicular to the background magnetic field, there are two methods to define its polarisation.

The first method takes into account the components of the electric field that are perpendicular to the background magnetic field. The polarisation is therefore defined as

$$P = i\frac{E_x}{E_y} \tag{2.8}$$

The second method takes into account the components of the electric field aligned in the direction of the background magnetic field and was mentioned in Subsection 1.8.2. Waves with an electric field component in this direction are referred to as ordinary waves, or O mode. Waves without this component are known as extraordinary waves, or X mode.

2.1.4 Mode Conversion

As mentioned in Subsection 2.1.2, in the hot plasma model mode conversion takes place at the resonance regions. For mode conversion to take place, we need two propagating plasma waves that are both solutions (or modes) to the same dispersion relation. This means that they will both have the same frequency ω and the same parallel component of the wave vector $k_{\parallel}$, but different perpendicular component $k_{\perp}$. As the waves propagate through the plasma, the $k_{\perp}$ profile will evolve. If, at some point, the $k_{\perp}$ values of both waves coincide, then mode conversion can take place. As mentioned in Subsection 2.1.2, in the hot plasma model this mode conversion takes place at the resonance regions. It is through this mode conversion that the first wave transfers some of its energy to the second wave, which will have different dispersion properties and will propagate through the plasma correspondingly.

2.1.5 Accessibility

So far in this section we have defined a wave in the cold plasma model, the regions of the plasma where this wave can propagate or be reflected, how polarization works and when does mode conversion take place. The final step is to assess whether the wave is able to reach the wave-particle resonance.

The accessibility of a wave refers to its potential to reach the desired location of absorption in the plasma. It depends on the compressional Alfvén or fast wave in equation 2.7 (this will be expanded upon later on). A wave is said to have good accessibility when it has a large

probability of arriving at the centre of the plasma. Whether a certain wave can reach the desired location will depend on both its dispersion characteristics and the plasma propagation traits. Reaching the resonance regions whilst avoiding the cutoff regions is a challenging matter.

There are two regions of interest in tokamaks where the waves will be expected to arrive; the low-field side (LFS) and the high-field side (HFS). HFS refers to the inner part of the torus where $R < R_0$, where the major radius R_0 is the radial distance from the center of the tokamak to the center of the poloidal section, and LFS refers to the outer part of the torus where $R > R_0$.

The accessibility of the waves to these regions will also depend on the position of the antenna. Where the waves are launched from is an important factor in avoiding certain cutoff regions. Positioning the ICRH antennas in the HFS would induce technical difficulties, such as limited access and high heat fluxes and radiation levels [39], so the antennas are typically located in the LFS.

2.1.6 Accessibility of Fast and Slow Waves

We can now consider the accessibility of slow waves and fast waves. In order to do so let us make two approximations. The first one is to use simplified forms of the elements of the dielectric tensor ε defined in Subsection 2.1.1. Using the small electron mass expansion we obtain the following

$$\begin{aligned} \frac{\omega_{pe}^2}{\omega_{ce}^2} &\simeq O(1), \\ \frac{\omega_{pi}^2}{\omega_{ci}^2} &\simeq O\left(\frac{m_i}{m_e}\right), \\ \frac{\omega^2}{\omega_{ci}^2} &\simeq O(1), \\ \frac{\omega_{pe}^2}{\omega^2} &\simeq O\left(\frac{m_i}{m_e}\right)^2. \end{aligned} \tag{2.9}$$

The second one concerns the parallel component of the refractive index. Since the influence of $n_{\parallel}$ at the frequencies considered is negligible, we can work with the approximation

$n_\parallel = 0$. Using these two approximations let us now consider the resonances and cutoffs of the slow and fast waves.

In the case of slow waves, employing these assumptions we obtain

$$n_\perp^2 = \frac{-\omega_{pe}^2}{\omega^2} \tag{2.10}$$

From the negative value of $n_\perp^2$ we can infer that the plasma is not able to support wave propagation and the wave is exponentially attenuated. A more detailed analysis considering $n_\parallel \neq 0$ shows that $n_\parallel^2$ is positive only when the condition $\omega^2 < \omega_{ci}^2 - \omega_{pi}^2/n_\parallel^2$ is satisfied. This suggests that the slow wave will only propagate through the plasma if the wave frequency is smaller than the cyclotron frequency. For a given frequency this places ω to the left of ω_c, which would mean launching the wave from the HFS of the plasma. It should be noted, however, that the slow waves can propagate in the LFS in the low-density scrape-off layer, and that they are generally believed to be responsible for RF sheath interactions [55]. RF sheaths can impact energy flux and develop high-voltage gradients at the boundary of the plasma, which might result in undesirable sputtering of material and the erosion of the surface [56]. Apart from the technical difficulties that HFS antennas entail, we also note that slow waves have a resonance surface at $\varepsilon_\perp = 0$ in the LFS of the plasma, so they would not be able to propagate to the main plasma. Studying cutoff surfaces is not necessary in the case of slow waves as there are no possible resonances.

Let us now regard fast waves. Using the approximations given above and considering a one ion plasma we obtain

$$n_\perp^2 = \frac{\omega_{pi}^2}{\omega_{ci}^2} \tag{2.11}$$

Since the perpendicular refractive index is positive we assume good accessibility to the centre of the plasma. For a more detailed analysis let us again consider $n_\parallel \neq 0$. With a non negligible $n_\parallel$ the wave resonance occurs at $\varepsilon_\perp = n_\parallel^2$. For a one ion plasma, this condition results in the Alfvén resonance frequency given by $\omega^2 = \omega_{ci}^2 k^2 c^2/(k^2 c^2 + \omega_{pi}^2)$. This frequency is always smaller than the IC frequency, so it would again mean that the resonance would take place, if it does, near the inner boundary of the plasma, in the HFS. For a multiple species plasma, using again the $n_\parallel \neq 0$ approximation, we find additional resonances of the fast wave. These resonances happen to be identical to the ion-ion hybrid resonances. Ion-ion hybrid resonances take place when a fast wave is coupled through mode

conversion to a short-wavelength mode referred to as the ion Bernstein wave. These waves, which are not described by the cold plasma model, are then rapidly absorbed via electron Landau damping. The ion-ion hybrid resonances, as well as the minority IC resonance layer (which will be explained in the next subsection), the cutoff surfaces and the evanescent regions are shown in Figure 2.1. The ion-ion hybrid resonance frequency for a two ion plasma is given by

$$\omega_{ii}^2 = \omega_{c1}^2 \frac{1 + f_1 Z_1 \left(\frac{Z_2 m_1}{Z_1 m_2} - 1\right)}{1 + f_1 Z_1 \left(\frac{Z_1 m_2}{Z_2 m_1} - 1\right)} \tag{2.12}$$

In order to obtain this expression we have used the charge neutrality condition given by $Z_1 f_1 + Z_2 f_2 = 1$ where $f_j = n_j / n_e$.

Let us now consider the cutoff regions of fast waves. There are two cutoff regions given by $n_\parallel^2 = \varepsilon_\perp + \varepsilon_{xy} = R$ and $n_\parallel^2 = \varepsilon_\perp - \varepsilon_{xy} = L$. R results in a cutoff layer (R-cutoff) in the LFS of the plasma. When considering $n_\perp^2 > 0$ and a one ion plasma, a boundary condition for the plasma density arises, which is given by

$$\omega_{pi}^2 > (\omega + \omega_{ci}) \omega_{ci} n_\parallel^2 \tag{2.13}$$

This expression suggests that, in order to avoid the cutoff layer and the corresponding wave evanescence region, the plasma density needs to stay above this threshold. This condition and the LFS cutoff layer mean that the antenna would need to be placed as close as possible to the plasma, inside the vacuum vessel, in order to achieve efficient coupling. The second cutoff region given by L (L-cutoff) is associated with the ion-ion hybrid resonance frequency. For a two ion plasma the cutoff frequency is given by

$$\omega_{cutoff} = \omega_{c1} \left[1 + f_1 Z_1 \left(\frac{Z_2 m_1}{Z_1 m_2} - 1\right)\right] \tag{2.14}$$

Looking at the expression for ω_{ii} provided above one realises that $\omega_{ii} < \omega_{cutoff}$ for a given background magnetic field. Therefore, for a given frequency, ω_{ii} is located to the left of ω_{cutoff} and the antenna would need to be placed in the HFS of the plasma in order to operate in the mode-conversion regime. In the mode-conversion regime, the fast wave is coupled to the ion Bernstein wave at the ion-ion hybrid resonance. However, in practice, limited space and access to the inside of the torus result in too many technical problems and the mode-conversion regime is not used for the heating of tokamaks.

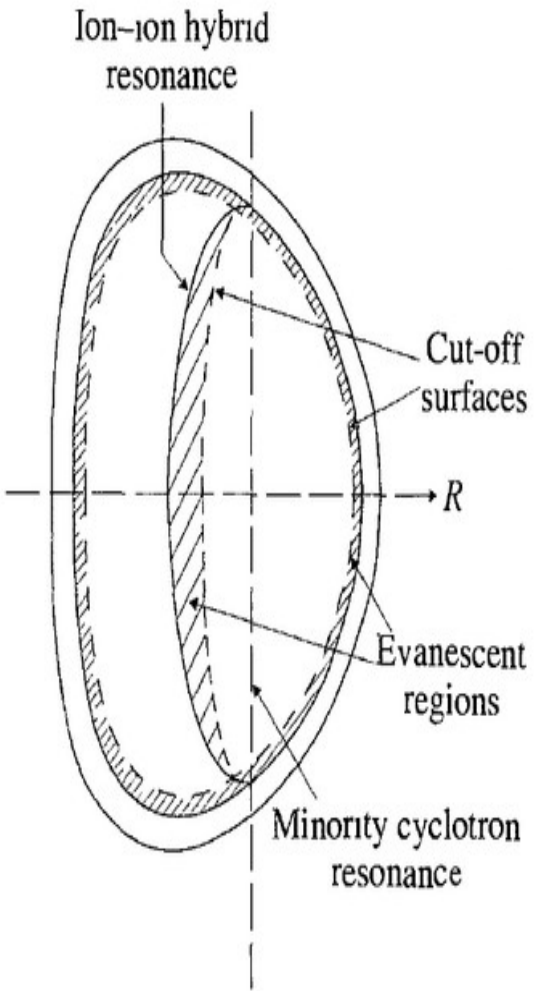

Fig. 2.1 *Poloidal section of a tokamak showing the location of the ion-ion hybrid resonance, cut-off surfaces, evanescent regions and minority cyclotron resonance [26].*

2.1.7 Minority Heating

So how does plasma heating with RF waves actually work? How can we use ICRF waves to achieve the correct polarization and accessibility to reach the resonance region of interest?

Due to the technical issues mentioned in Subsection 2.1.6 above, plasma heating in tokamaks relies on fast wave energy absorption at the IC resonance rather than in the mode-conversion regime. In the previous section we learned that fast wave resonance takes place in the HFS of the plasma, if at all. Placing the antenna in the LFS of the plasma would therefore result in the wave reaching the IC resonance first. However, heating the plasma via fundamental IC resonance with a LFS antenna does not work due to unfavourable polarisation.

As discussed in Subsection 1.8.2, the strength of the IC damping is proportional to the amplitude of the left circularly polarised component of the wave, E_+. The efficiency of the damping will therefore depend on the ratio of E_+ to the counter-rotating component of the electric field, E_-. For a one ion plasma in the cold plasma approximation this relation is given by

$$\frac{E_+}{E_-} \simeq \frac{\varepsilon_{xy}+\varepsilon_\perp}{\varepsilon_{xy}-\varepsilon_\perp} = \frac{\omega-\omega_{ci}}{\omega+\omega_{ci}} \tag{2.15}$$

It can be seen from this equation that when the wave frequency is the same as the IC frequency ($\omega = \omega_c$), the left circularly polarised component vanishes. Right handed polarisation of the wave means very poor absorption at the fundamental IC resonance. There are three main solutions to this problem; using the higher harmonics, working in the minority heating regime and using the three-ion scheme.

Let us start with the higher harmonics. Using the higher harmonics and taking equation 1.1 into consideration, expression 2.14 above becomes

$$\frac{E_+}{E_-} = \frac{l-1}{l+1} \tag{2.16}$$

In this scenario E_+ is no longer 0 and absorption can take place.

The second solution to the polarization problem is working on the minority heating regime. Minority heating consists of adding a small percentage of another ion species with a higher IC frequency to the plasma. The fundamental resonance of the minority species needs to be inside of the plasma. The dispersion relation of the wave is mostly determined by the

majority ion species, so the E_+ of the wave will not vanish. We are now, however, working with a two ion plasma, so the locations of the ion-ion hybrid resonance and its associated cutoff region must be considered. Looking at equations 2.11 and 2.13 we can see that, for a given background magnetic field, both the ion-ion hybrid resonance and the associated cutoff resonance are smaller than the fundamental minority resonance frequency. This means that the resonance will be located to the right of these regions, towards the outer side of the plasma. An antenna in the LFS of the plasma can launch a fast wave with good accessibility that reaches the fundamental minority resonance and heats the minority ions. This is only true if the charge-to-mass ratio ($\mathcal{Z} = (Z/A)_i$) of the minority species is larger than that of the majority species.

A more thorough analysis of equation 2.14 reveals that, in the cold plasma approximation, the left circularly polarised component of the wave vanishes in the minority heating regime as well. However, the Doppler effect needs to be taken into account. The polarisation close to the minority fundamental frequency of the wave evolves more rapidly in a two ion plasma than in a single species plasma. This allows Doppler broadening of the resonance, which creates a widening in the resonance large enough for reasonable absorption to take place. It should be noted that the harmonics of an IC frequency can be used to heat the ions in both a majority and minority scenario. However, fundamental IC resonance heating can only be used in a minority scenario. As the minority concentration is increased, the wave polarisation becomes unfavourable and mode-conversion to ion Bernstein wave can take place. Finding the appropriate minority concentration to allow the appearance of a region with higher E_+ polarization is not trivial.

The third solution is the so called three-ion-scheme. Even though absorption via fundamental IC resonance heating in the minority heating regime can take place through Doppler broadening, absorption is limited by the ratio of left-hand to right-hand polarization [57], as

$$\left|\frac{E_+}{E_-}\right|_{\omega=\omega_{c2}} \sim \left|\frac{\mathcal{Z}_2-\mathcal{Z}_1}{\mathcal{Z}_2+\mathcal{Z}_1}\right| < 1 \tag{2.17}$$

where equation 2.17 has been evaluated at the IC resonance of minority ions ($\omega = \omega_{c2}$).

From the definitions of the R and L cutoff regions above and expression 2.15, it can be seen that a fast wave in the R-cutoff region will have $E_+ = 0$. A fast wave in the L-cutoff region, however, will have $E_- = 0$ and favour ion heating. Introducing a third ion species with a IC resonance at the L-cutoff region can lead to very efficient ICRF heating. This method of achieving a favourable polarisation and maximizing E_+ is known as the three-ion scheme.

The three-ion scheme consists of adding a third minority ion species (Z) to the main ion species (X and Y). This solution is based on the idea that placing the left hand polarised fast wave L-cutoff close to the fundamental IC resonance of the minority species Z ($\omega = \omega_{c3}$) largely increases the field component E_+ [58]. In order to locate the L-cutoff at the desired region, the density ratio between the main two ion species in the plasma can be adjusted. Similarly to the minority heating regime, the two main ion species X and Y determine the wave polarization. The third ion species Z then absorbs almost all of the incoming RF power by profiting from the E_+ enhancement close to the L-cutoff region. Extremely small concentrations of species Z can be used to absorb most of the ICRF power due to the fact that $|E_+/E_-| >> 1$ close to the L-cutoff . A necessary condition for this scheme to lead to a E_+ enhancement is that the IC resonance of the species Z is located between the IC resonances of the species X:Y, i.e. $min\{Z_1, Z_2\} < Z_3 < max\{Z_1, Z_2\}$. The combination of a large power absorbed and a very small concentration of resonant ions leads to a very high power per resonant ion, which means that the three-ion scheme has been found to facilitate the generation of fast ions in ICRF heated plasmas.

Finding the optimal X:Y ratio for the most efficient absorption by the Z resonant ions is a relevant matter. Let us consider a H:^{4}He plasma where a very small concentration of ^{3}He is introduced as the species Z. This scenario will be studied in Chapter 4. The frequencies of the ion-ion hybrid resonance (ω_{ii}) and the L-cutoff (ω_{cutoff}) depend on the plasma composition and the parallel refractive index of the fast wave [59]. As explained above in this subsection, resonance takes place when the L-cutoff matches the fundamental resonance of species Z ($\omega_{cutoff} = \omega_{c3}$). The optimal X:Y ratio can be calculated from this equality as derived in [60]

$$\omega_{cutoff} \sim \omega_{c2} + (\omega_{c1} - \omega_{c2}) Z_2 f_2 + \frac{\alpha(\omega_{c1} - \omega_{c2})^2 Z_2 f_2 (1 - Z_2 f_2)}{\omega_{cH}} = \omega_{c3} \tag{2.18}$$

where $\alpha = (\omega_{cH}^2/\omega_{pH}^2) n_\parallel^2$ and $\omega_{pH} = (4\pi n_e e^2/m_H)^{1/2}$. The first two terms of equation 2.18 describe the gradual shift of the L-cutoff frequency from ω_{c1} to ω_{c2} for $n_\parallel = 0$. The last term describes the upshift of the L-cutoff frequency due to $n_\parallel \neq 0$. Using the $n_\parallel = 0$ approximation, a first order expression for the X:Y optimal mix is given by

$$\begin{aligned} f_2^* &\sim \frac{Z_3 - Z_2}{Z_1 - Z_2} \\ f_1^* = 1 - f_2^* &= \frac{Z_1 - Z_3}{Z_1 - Z_2} \end{aligned} \tag{2.19}$$

where $f_n^* = Z_n f_n$. Taking into account $n_\parallel \neq 0$, the next order correction is given by

$$f_2^* = \frac{Z_3 - Z_2}{Z_1 - Z_2} - \frac{(Z_1 - Z_3)(Z_3 - Z_2)}{Z_1 - Z_2}\alpha \tag{2.20}$$

This next order correction is small for fusion relevant parameters [58].

2.2 Damping Mechanisms

Now that we have defined the basic concepts of how a wave propagates in the cold plasma model, let us progress to the next step and understand how the wave is absorbed by the plasma.

The fast wave carries an important fraction of its energy in the component of the electric field perpendicular to the background magnetic field. As discussed in Subsection 2.1.7, this component rotates in the same direction as the ions, so there is a strong absorption of the fast wave energy in the fundamental and harmonics. This absorption is referred to as damping in the IC resonance and will be discussed in this section. The other method of absorption discussed in this section is direct electron damping. Direct electron damping depends on the component of the electric field parallel to the background magnetic field. As this component is relatively small in the fast wave, direct electron damping is normally small. Apart from these two processes and as mentioned in Subsection 2.1.4, the fast wave can undergo mode conversion. When this happens, the physical properties governing the new mode-converted wave can differ greatly from the physics of the original fast wave. Therefore, the new wave can be absorbed in a different part of the plasma.

2.2.1 Damping at the Ion Cyclotron Resonance

Damping of the electromagnetic wave at the IC resonance depends on the Larmor radius r_c. As discussed in Subsection 1.8.2, when the Larmor radius is negligible, i.e. the wavelength perpendicular to the background magnetic field is much larger than the Larmor radius, damping at the IC resonance takes place when the frequency of the wave is the same as the IC frequency. In the case of damping at the fundamental cyclotron resonance, if the ion is in phase with the wave, it will remain in phase over the complete period and experience net acceleration. This happens because the wave electric field in the perpendicular direction to the magnetic field does not vary in space over the period, so the kick in energy that the ion experiences is always positive.

When the Larmor radius is finite with respect to the perpendicular wavelength, the wave electric field does vary in space and the kick in energy can be either positive or negative. The ions can therefore win or lose energy. This means that FLR effects are relevant for damping at both the fundamental and the harmonic IC resonance. Not only this, but in the FLR regime, the electric field component rotating in the opposite direction to the ions, E_-, can give rise to absorption as well as the E_+ electric field component.

The general expression for the kick in energy in the perpendicular direction to the magnetic field that a particle experiences when going through a resonance region after taking into account FLR effects and both components of the electric field E_+ and E_- scales as

$$\Delta v_\perp \propto \left[E_+ J_{n-1}\left(\frac{k_\perp v_\perp}{\omega_{ci}}\right) + E_- J_{n+1}\left(\frac{k_\perp v_\perp}{\omega_{ci}}\right)\right] \tag{2.21}$$

Here, J_n is a Bessel function of the first kind, $k_\perp$ is the perpendicular wave vector and n stands for the cyclotron harmonic number. In theory, the relative phase of the ions and the wave can be preserved between the transits of the ion through the resonance region. If this happens, the wave creates a phase-space island where the ion oscillates, gaining no net energy. In practice, however, non-linearity caused by the wave-particle interaction between successive transits and collisions modify the relative phase of the wave and the Larmor motion of the particle. This means that the ion can experience random kicks that can lead to either energy gains or losses from the wave. If more ions are decelerated, then they lose energy and the amplitude of the wave grows, leading to an energy gain for the wave and possible instabilities. If more ions are accelerated, then the wave power is absorbed by the resonating ions. This is the usual case due to the fact that the velocity distribution function of the ions follows a Maxwellian distribution and hence decreases with velocity. There will therefore be more ions with low perpendicular velocities than with high perpendicular velocities and the energy of the wave will tend to flow to the ions.

There are three main physical effects that can be drawn from equation 2.16. Firstly, in the case of the fundamental IC resonance, the kick that the particles will experience in the perpendicular velocity is quite uniform. This means that the low energy ions will be efficiently accelerated by the ICRF wave. Secondly, the absorption at the higher harmonics ($n > 2$) is weak for low perpendicular velocities, so low energy ions will not be efficiently accelerated by the ICRF wave. The strength of the absorption increases with the increasing perpendicular velocity until it reaches a maximum in the MeV range and then starts decreasing. Therefore, thermal plasmas will not be efficiently heated by the harmonic IC resonance as the higher

harmonic damping is rather weak. Lastly, the damping strength decreases as the harmonic number increases, although it typically increases in the presence of higher energy ions.

Although neutral beam injected particles are sometimes used to alleviate this issue, no external methods are needed to heat the plasma at higher harmonics. Given that the plasma is hot and dense enough, that is, that it has a sufficiently large perpendicular velocity and perpendicular wave vector, a high-energy tail will start to develop in the velocity distribution function of the ions. If the machine parameters allow the energetic ions to be confined, the wave will interact with more high-energy ions, a high-energy tail in the distribution function will evolve and the damping will be enhanced. Consequently, higher harmonics can be used to heat the plasma even if the distribution function of the resonating ions is Maxwellian at the beginning.

Finally, it should be noted that there are certain ion velocities at which the contributions by the rotating and counter-rotating electric field components in equation 2.15 can cancel each other out. This means that there is no net acceleration, which can lead to a so-called barrier. This barrier can prevent resonating ions from reaching higher energies.

2.2.2 Direct Electron Damping

Fast ICRF waves can also interact and heat electrons, which act as a competing absorption mechanism against damping at the IC resonance. Direct electron damping can take place through two different mechanisms; electron Landau damping (ELD) and transit-time magnetic pumping (TTMP).

Electron Landau damping takes place when the parallel electric field component of the wave accelerates the electrons in the direction parallel to the background magnetic field. Landau damping is usually weak due to the fact that the parallel electric field component of the fast wave is normally quite small. TTMP arises from the magnetic moment associated with the cyclotron motion of the electrons. This means that the parallel gradient of the wave magnetic field will also accelerate the electrons along the magnetic field. These two acceleration processes counteract each other, reducing the overall absorption. Direct electron damping can, however, be relevant for plasmas with high electron density and temperature, and for ICRF waves with a large parallel electric field component.

2.3 The Distribution Function

We have in previous sections spoken about the distribution function, but we will now use this section to deal with it explicitly. Treating a plasma as a system composed of N particles where the equations of motion $F_i = m_i a_i$ need to be solved for all particles in a $6N$ space knowing the initial positions and velocities is prohibitive both analytically and computationally. Instead, in kinetic theory the system is described macroscopically through magnitudes that can depict the system locally, such as flow, density or temperature. The distribution function $f(\mathbf{r}, \mathbf{v}, t)$ is the most important magnitude in this description. It represents the particle density in a six-dimensional phase space and expresses the probability of finding a particle in a volume $d\mathbf{r}d\mathbf{v}$ when normalised as $\int d\mathbf{r}d\mathbf{v}f = 1$.

Now let us consider a plasma heated by ICRF waves. The distribution function will be modified by the interaction of the ICRF waves with the plasma particles and will therefore evolve in time. In order to conserve the number of particles, f must satisfy the kinetic continuity equation

$$\frac{\partial f}{\partial t} + \nabla_{\mathbf{r},\mathbf{v}}((\vec{v}, \vec{a})f) = 0 \tag{2.22}$$

Taking into account that the Hamiltonian continuity equations must also be satisfied, the continuity equation above is hence modified to the Boltzmann equation [61]

$$\frac{\partial f}{\partial t} + \vec{v} \cdot \nabla_r f + \frac{\vec{F}}{m} \cdot \nabla_v f = \left.\frac{\partial f}{\partial t}\right|_{coll} \tag{2.23}$$

Here, we have introduced two new relevant terms. $\vec{F}$ expresses the contributions from external forces, including the electromagnetic Lorentz force due to externally applied electric fields, whilst the term on the right-hand side of the equation expresses the contributions from particle collisions, or internal forces.

A series of assumptions have been made in order to derive the Boltzmann collision term [61]; i) only binary collisions are considered, neglecting higher-order interactions, ii) the velocities of interacting particles before collisions are uncorrelated, and iii) external forces are ignored in determining the collision cross-sections. The Boltzmann collision term can serve as the initial step in deriving the Fokker-Planck collision term, under the premise that each individual long-range interaction induces only minor deviations (small-angle deflections) in particle trajectories. Given that individual interactions are quite weak, the collective impact of numerous simultaneous interactions can be viewed as a cumulative succession of weak

binary collisions, and function as a valid representation of the multiple Coulomb interaction [61].

Using the arbitrary function of velocity $\chi(\mathbf{v})$, for weak binary collisions where the change in velocity is assumed to be small, then $\chi' = \chi(\mathbf{v}') = \chi(\mathbf{v}+\Delta\mathbf{v})$, which can be expanded in a Taylor series about $\mathbf{v}$ and substituted into equation 2.23. Let us now factor out the arbitrary function $\chi(\mathbf{v})$ by integrating by parts, and define the modified averages over the scattering angle $\langle \Delta X \rangle$ and the velocity distribution function of the scatterers $\langle \Delta X \Delta X \rangle$. It should be noted that both these quantities are in between brackets because they represent the mean values during a time Δt, and that they are written in terms of the position of the particle in the phase-space X. We now obtain the formal expression of the Fokker-Planck equation [61]

$$\frac{\partial f}{\partial t} = \frac{\partial}{\partial X} \cdot (\langle \Delta X \rangle f) + \frac{1}{2} \frac{\partial^2}{\partial X^2} : (\langle \Delta X \Delta X \rangle f) \tag{2.24}$$

The Fokker-Planck equation describes how the distribution function of the resonating ions will evolve in time in the ICRH field. Here, ΔX is known as the friction coefficient and $\Delta X \Delta X$ is known as the diffusion coefficient. ΔX tends to accelerate or decelerate the particles until they reach the average equilibrium velocity, whereas $\Delta X \Delta X$ represents the diffusion in velocity space until equilibrium is reached [61]. The friction coefficient is given by

$$\langle \Delta X \rangle = \frac{1}{\Delta t} \int d(\Delta \mathbf{X}) \Delta X \, \psi(X, \Delta X) \tag{2.25}$$

Here, the probability that X changes by ΔX is given by the function $\psi(X, \Delta X)$.

The evolution of the distribution function is determined by the influence of two factors; the collisional relaxation and the heating of the resonating particles. These factors will be treated in the following subsections.

2.3.1 Collisional Heating

Let us start with collisional relaxation. After the resonating ions have been heated by the ICRF wave they will slow down via collisions. Whether they collide with other ions or with electrons is determined by the critical energy. The critical energy is a threshold energy given by

$$E_{crit} = 14.8AT_e \left[\sum_j \frac{n_j Z_j^2}{n_e A_j} \right]^{\frac{2}{3}} \tag{2.26}$$

Here, A stands for the atomic number and T_e for the electron temperature. The sum in the equation is over all thermal ion species. When the energy of the ions is the same as the critical energy, the rate of loss of energy to electrons and ions is equal. When the energy of the resonating ions is larger than the critical energy, the ions will collide mainly with the background electrons and electron heating will dominate. This happens because, at high energies, the massive ions will not change their trajectories significantly and will therefore collide with the smaller electrons as they are decelerated. This can be expressed in terms of the pitch angle $cos\theta = v_{\|}/v$. When $E > E_{crit}$, there will not be any meaningful scattering and the pitch angle will remain almost constant. When the energy of the resonating ions is lower than the critical energy, they will mainly collide with the thermal ions and bulk ion heating will dominate. In this case, both pitch angle scattering and energy diffusion become relevant. Consequently, it is important to keep the energy of the resonating ions below the critical energy in order to achieve good bulk ion heating.

However, collisions are often not fast enough to thermalize the fast ions. This is due to the fact that the collision frequency decreases sharply at high velocities, scaling as v^{-3}, modifying the velocity distribution function, which becomes strongly non-Maxwellian. As mentioned previously in this section, the fast ICRF wave accelerates the resonating ions mainly in the direction perpendicular to the background magnetic field. Therefore, the perpendicular velocity of the ions will increase to $v_{\perp} >> v_{\|}$ in the high-energy, low-scattering angle regime. This condition produces an anisotropic tail in the direction perpendicular to the magnetic field, where a large fraction of trapped ions is present.

Let us now consider heating at the harmonics of the IC frequency. As mentioned in Subsection 2.2.1, low energy ions are not efficiently accelerated in this regime and the strength of the absorption increases with the increasing perpendicular velocity. This produces a high-energy tail in the velocity distribution function with a small number of very high-energy trapped ions. The turning points of the drift orbits of these trapped ions gradually move towards the IC frequency or one of its harmonics. The ICRF modelling of such ions is quite challenging as their drift orbits are usually spread over more than one flux surface.

Finally, it should be noted that the resonating ions that collide and heat the bulk ions also enhance fusion reactivity. This is due to the fact that, in the low energy regime, the fusion

reactivity increases with the increasing centre-of-mass energy of the fusion-reacting ions. ICRF heated ions can therefore increase the fusion yield.

2.3.2 Fast Ions

We have so far explained how the distribution function is affected by collisional relaxation. Let us now consider the second factor; the heating of resonating particles.

Fast ions are produced when the resonating ions absorb the energy in the ICRF wave. The fast ions will then produce a tail in the distribution function, which will become non-Maxwellian if the velocities of the fast ions are too high for collisional relaxation to take place. The efficiency of the bulk ion heating and, consequently, the fusion reactivity, depend strongly on the behaviour of fast ions. Here, we will define some fast ion parameters that will be used in later sections.

The density of the fast ions is expressed by n_f, which is relevant to compute the energy of the fast ions. $\langle E_{fast,i} \rangle$ stands for the average energy of the fast resonating ion i, which should stay below E_{crit} in order to achieve good bulk ion heating. The mean time that the fast ions need to undergo collisional relaxation and become thermal is known as the slow-down time, expressed by τ_s. The slow-down time is used in the computation of the fast ions distribution function, as the distribution function is proportional to $f \propto exp(-E_\perp / T_{tail})$, where $T_{tail} \simeq E_{fast}/n_{fast}$ and $E_{fast} \simeq P_{abs}\tau_s/2$. Lastly, as mentioned in Subsection 2.3.1, the drift orbits of trapped ions can change of magnetic surface. The width of these drift orbits is referred to as the orbit shift from the magnetic flux surface, given by δ_p/a.

2.4 Modelling of ICRF Heating

As explained in Section 1.4 and Subsection 1.8.2, the modelling of ICRF heating is a crucial step in understanding the interaction between the ICRF waves and the plasma. It plays a pivotal role in determining the power absorption for each resonant species and predicting the evolution of the velocity distribution function of the resonant ions in ICRF heated plasmas. This information is essential for calculating various critical parameters, including neutron yield, plasma energy and the collisional transfer of energy from ions to background electrons and bulk ions. By employing ICRF modelling, we gain valuable insights into plasma behavior under external heating conditions, such as ICRF heating.

The modelling of ICRF heating can be decomposed into two parts: i) the modelling of the power deposition, which encompasses the coupling, propagation and absorption of the wave, and ii) the modelling of the evolution of the distribution function of the resonating ions. In order to compute the coupling and propagation of the wave, the distribution function is needed, and in order to compute the distribution function, the absorbed power is needed. These problems are therefore coupled and can only be solved self-consistently.

2.4.1 Modelling of the Power Deposition

For the purpose of evaluating the coupling, propagation and absorption of the fast wave, the general wave equation (2.1) needs to be solved and, hence, the dielectric tensor must be known. In order to do so, let us decompose the dielectric tensor into a Hermitian and an anti-Hermitian component $\varepsilon = \varepsilon^H + i\varepsilon^A$. The Hermitian component is defined as $\varepsilon^H = (\varepsilon + \varepsilon^\dagger)/2$, whilst the anti-Hermitian component is defined as $\varepsilon^A = (\varepsilon - \varepsilon^\dagger)/2i$, where † stands for *adjoint* [62]. ε^H describes the wave propagation, whilst ε^A describes the absorption. This means that both components are linked through the causality principle, and in practice, ε^H can be evaluated assuming that ω is real in the conductivity tensor σ (defined as $j = \sigma \cdot \mathbf{E}$, where j is the current density and $\mathbf{E}$ is the electric field), and ε^A can be deduced by appending an imaginary part to the frequency. It should be noted that, in the cold plasma model, the anti-Hermitian part of the dielectric tensor is zero because the particle trajectories are unperturbed and perfectly deterministic, and collisional heating as a mechanism of irreversible power transfer needed to be added to the cold plasma model in order for this model to describe wave power absorption [62]. The irreversible dissipation of the wave is hence governed by the anti-Hermitian part of the dielectric tensor ε^A. Although deviations from the thermal equilibrium do not particularly affect the Hermitian component of the dielectric tensor, they do have significant effect on the anti-Hermitian part. The elements in ε^A are proportional to the distribution function of the particles and the gradient of said distribution in velocity space. Consequently, the presence of energetic, non-thermal particles will affect ε^A [63]. As was mentioned in Subsection 2.2.1, the strength of the absorption strongly depends on the presence of fast ions. Furthermore, it depends on both the parallel and perpendicular components of the particle velocity distribution.

The parallel component of the velocity distribution determines the Doppler effect given in the resonance condition in Subsection 1.8.2, even if it does not have a direct effect on the absorption and propagation of the wave. The broadening of the power deposition profile is therefore governed by the parallel velocity distribution function. The perpendicular component of the velocity distribution determines the absorption strength. The narrowing of

the deposition profile is therefore given by the perpendicular velocity distribution function. Both components are also influential in the ICRF power partitioning between resonating species.

Let us now consider mode-converted waves. The calculation of the propagation and power deposition of these waves is remarkably challenging. In order to study mode-converted waves through a simple description of resonant absorption and tunnelling, the Budden model is used. The Budden model [63] describes the physics of a cutoff-resonance pair and provides an expression for the transmission coefficient T. The transmission coefficient is the fractional power transmitted across the wave resonance per unit of incident power and is given by $T = e^{-\pi k_0 x}$. Here, k_0 stands for the wave number far away from the cutoff region and x stands for the separation between the cutoff and the resonance. Whether the wave encounters the cutoff or the resonance first has no effect on the transmission coefficient, but it does have an effect on the reflection coefficient R. If the wave encounters the resonance before the cutoff, there is no reflection and the coefficient is given by $R = 0$. If the wave meets the cutoff first, the reflection coefficient is given by $R = (1-T)^2$.

2.4.2 Modelling of the Evolution of the Distribution Function

As indicated in Section 2.3, the evolution of the distribution function of the resonating particles is computed by the orbit-averaged Fokker-Planck equation [64]

$$\frac{\partial f}{\partial t} = \langle C(f) \rangle + \langle Q(f) \rangle \tag{2.27}$$

Here, $Q(f)$ stands for the quasi-linear operator that contains the contributions from wave-particle interactions, $C(f)$ stands for the collisional operator, and $\langle\rangle$ denotes the average of a quantity over a drift orbit. The explicit form of the collisional operator is given in [65] by

$$C(f) = \frac{1}{v^2}\frac{\partial}{\partial v}[-\alpha(v)v^2 f + \frac{1}{2}\frac{\partial}{\partial v}(\beta(v)v^2 f)] + \frac{\gamma(v)}{4v^2}\frac{\partial}{\partial \mu}(1-\mu^2)\frac{\partial f}{\partial \mu} \tag{2.28}$$

Here, $C(f)$ is given in terms of the variables (v, μ), where v is the particle velocity and $\mu = v_\perp / v$ is the cosine of the pitch angle of the particle relative to the magnetic field. The notation in equation 2.28 is given by the collision coefficients describing dynamical friction on the background species α, energy diffusion β and pitch angle scattering γ [65].

The distribution function present in the expression for the orbit-averaged Fokker-Planck equation is a function of the invariants describing single particle motion. Whether this equation is two or three dimensional depends on if the radial widths of the drift orbits are taken into account. At the small radial orbit width limit, the Fokker-Planck equation is two-dimensional in velocity space. In this case, the magnetic moment $\mu = mv_{\perp}^2/2B$ and the velocity are the invariants of motion. Stix was the first to use this two-dimensional version of the Fokker-Planck equation [54] to study the evolution of the velocity distribution function of the resonating ions in the presence of ICRF waves. When taking into account non-negligible radial orbit widths, the equation becomes three-dimensional and three invariants are needed. In this case, the invariants are (E, Λ, P_ϕ), where Λ stands for $\Lambda = \mu B_0/E$ and B_0 stands for the magnetic field at the axis. Using these invariants, the orbit-averaged quasi-linear operator becomes

$$\langle Q(f) \rangle = \sum_N L_N (D_{RF}^N L_N f) \tag{2.29}$$

where

$$L_N = \frac{\partial}{\partial E} + \frac{n\omega_{c0} - \Lambda\omega}{\omega E} \frac{\partial}{\partial \Lambda} + \frac{N}{\omega} \frac{\partial}{\partial P_\phi} \tag{2.30}$$

and the diffusion coefficient D_{RF}^N present in 2.28 is given by

$$D_{RF}^N = \frac{1}{4\omega^2} \sum_{\substack{resonance \\ points}} \frac{(Ze^2)}{|n\omega_{cR}|} v_{\perp R}^2 \left| E_+ J_{n-1}\left(\frac{k_\perp v_{\perp R}}{\omega_{cR}}\right) + E_- J_{n+1}\left(\frac{k_\perp v_{\perp R}}{\omega_{cR}}\right) \right|^2 \tag{2.31}$$

Here, the subscript R represents a magnitude evaluated at the resonance.

In this last section, the theoretical groundwork for the modelling of ICRF heating was laid out, discussing the basic aspects of power deposition and the evolution of the distribution function of resonating ions. The interdependence of these two components was emphasized, showcasing the necessity for a self-consistent solution. In the next chapter, the implementation of these theoretical concepts is studied through the PION code [1]. The PION codes serves as the interface between the formal mathematical definitions above and the computational simulations that are the basis of this thesis. By understanding the theory discussed in Subsection 2.4.2, we can now study how PION utilizes these principles to simulate and analyze the physics of ICRF heating in Chapter 3, providing valuable insights into the be-

havior of RF-heated plasmas. This transition from mathematical theory to computational application represents a crucial bridge in the holistic understanding of any physical process.

Chapter 3

Modelling of ICRF Heating with the PION Code

In this Chapter the steps to model ICRF with the PION code [1, 2] are discussed. Similarly to Subsection 2.4.2 above, the description is divided into several processes; the power deposition model, the evolution of the distribution function and computation of the Fokker-Planck equation and the coupling of both processes. An account of the structure of ETS is also given.

PION has been extensively validated against experimental data on JET [2, 66–74], AUG [75–80], DIII-D [81], and WEST (formerly Tore Supra) [82, 83] for many minority and majority heating schemes. At JET, it is part of the second data processing chain.

Recently, PION was integrated [5] into the EUROfusion Integrated Modelling & Analysis Suite (IMAS) [84]. IMAS is the computational platform that supports plasma operations and research activities at ITER. It uses a data model that can describe both experimental and simulated data with the same representation. The integration of PION into IMAS has allowed collective development of integrated modelling tools and workflows. In this work we use PION as integrated into the transport modelling workflow European Transport Solver (ETS) within IMAS. This integration is relevant because it provides the capabilities to simulate the evolution of a plasma discharge. Both interpretative and predictive simulations are possible. ETS has been validated against experimental data on JET [36, 85–88].

3.1 The PION Code

The modelling of ICRF involves calculating the power deposition and the evolution of the distribution function of the resonating ions in a self-consistent way. Theoretically, a full wave code that computed the power deposition could be coupled with a two-dimensional Fokker-Planck code that worked iteratively. This process would, however, be very expensive computationally and would result in long execution times. In order to analyse a large number of discharges in a quick manner, a simplified model is required. PION is an iterative, fast ICRF modelling code based on simplified models. It calculates the time evolution of the resonating ions distribution functions by solving a one-dimensional Fokker-Planck equation and computes the ICRF power absorption in a self-consistent way.

A typical PION simulation involves several time steps, as shown in Figure 3.1. In each time step, the background plasma parameters are read, and the absorbed power deposition is calculated. Then, the result of this calculation is used as the input of the one-dimensional Fokker-Planck solver, which outputs a distribution function. This distribution function is then used to calculate the absorbed power in the next time step.

The main features of PION are divided in two procedures described below, i.e. the power deposition model and the Fokker-Planck calculation.

3.1.1 The Power Deposition Model

The power deposition model in the PION code [90] originates from the model used in the full wave code LION [91], developed by Hellsten and Villard. This model is based on fundamental observations of the wave fields in a tokamak. Although certain parameter optimisation has taken place in PION as compared to LION, the power deposition profiles of both codes are in good agreement.

In order to calculate the power deposition, the launched wave is Fourier decomposed in the toroidal direction [90, 92]. The power deposition is then calculated for each toroidal mode number. This model describes the wave field as being the superposition of two elements; one in the limit of strong absorption and one in the limit of weak absorption [91]. Using this superposition we can compute the Poynting flux. The magnetic flux-surface-averaged Poynting flux for a given Fourier mode with toroidal mode number N is given by

$$P(s) = \alpha_s P_1(s) + (1 - \alpha_s) P_2(s) \tag{3.1}$$

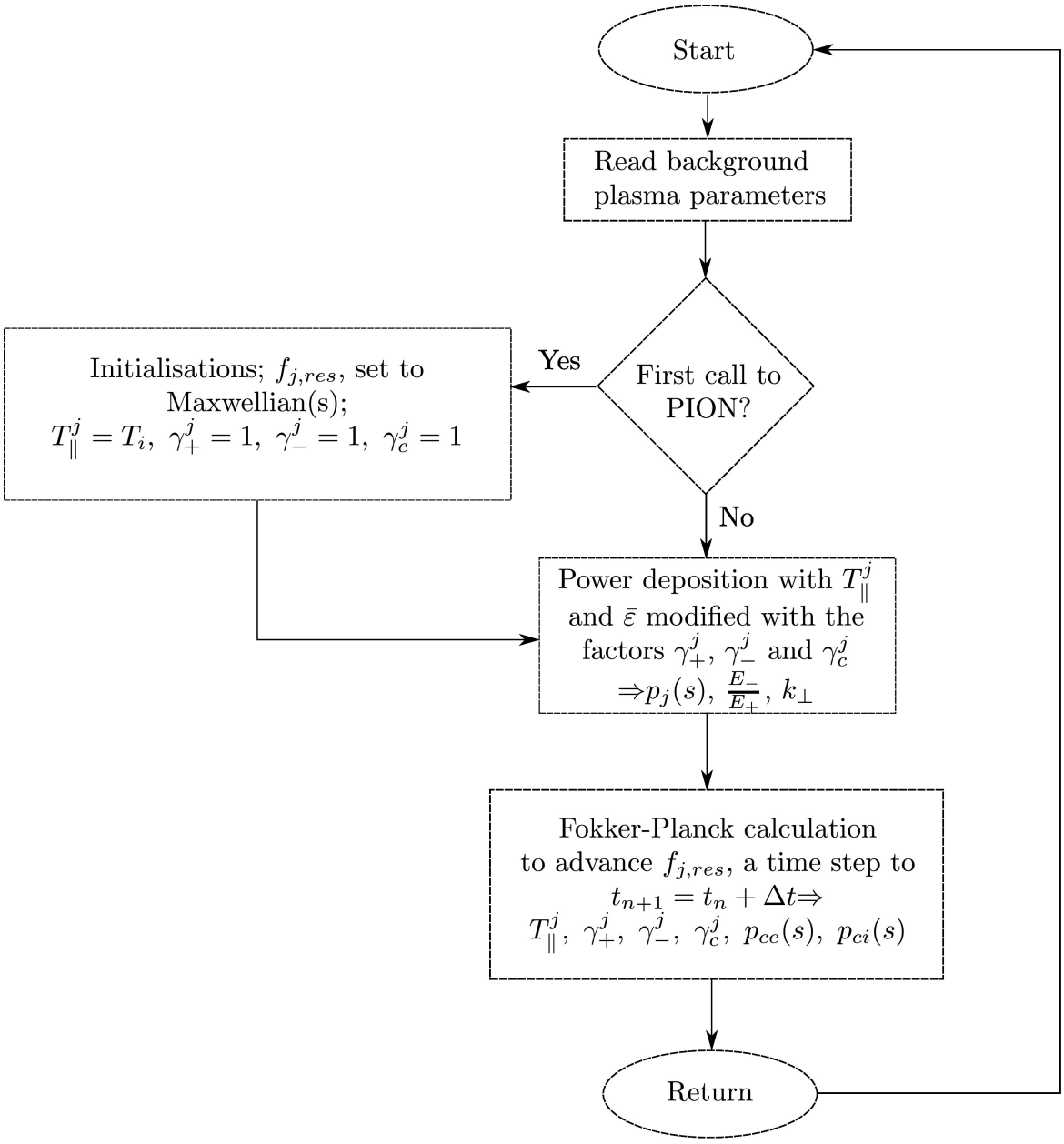

Fig. 3.1 *Flowchart of the PION code [89].*

Here, $P_1(s) = \sum_j P_{1j}(s)$ represents the strong absorption, $P_2(s) = \sum_j P_{2j}(s)$ the weak absorption and α_s is a constant. These functions are expressed in terms of s, which is a normalised flux surface given by $s = (\psi_p - \psi_{p0})/(\psi_{pa} - \psi_{p0})^{\frac{1}{2}}$. In this expression, ψ stands for the poloidal flux, and the subscripts 0 and a indicate the centre of the magnetic axis and the plasma boundary, respectively.

The assumptions and explicit derivations of both $P_1(s)$ and $P_2(s)$ are presented in [90]. $P_1(s)$ is described as the ansatz to the flux-surface-averaged Poynting flux for an antenna located in the LFS and for equilibria having a large aspect ratio and circular cross section, and it is given by

$$P_1(s) = P_1(1)\frac{1 - e^{[-(s/s_0)^2 ln2]}}{1 - e^{[-(1/s_0)^2 ln2]}} \tag{3.2}$$

where s_0 is the half width, which was calculated by the LION code. This ansatz is found to describe well the power deposition when the wave is focused on the magnetic axis and the minor radius is large compared to the wavelength.

Obtaining an ansatz for $P_2(s)$ is a little bit more complex. Assuming that for weak damping the structure of the wave field will not change much with the variation of the absorption strength and profile, the power deposition is divided by the single pass absorption coefficient $a_s(s)$ (which will be expanded upon below), separating the dependence of the field and geometry from the absorption and obtaining

$$f(s) = \frac{C_2}{P_2(1)a_s(s)}\frac{d\vec{P}_2}{ds} \tag{3.3}$$

where C_2 is a normalization factor given by $\int_0^1 a_s(s)f(s)ds = 1$. $f(s)$ is then computed from equation 3.3, where $d\vec{P}_2/ds$ is calculated by LION, for various density profiles and geometries, and verified to stay roughly constant. $a_s(s)$ is found to be proportional to the minority concentration when heating at the cyclotron resonance of a minority species with low concentration, and to $n_\alpha k_\perp^2 T_\alpha$ when heating at the second harmonic, where α denotes the resonant species, $k_\perp$ is the wavenumber perpendicular to the background magnetic field, n_α, T_α are the densities and temperature of the resonant species. When $f(s)$ and $a_s(s)$ are known, $\vec{P}_2$ can then be determined from equation 3.3.

The Poynting flux is used to obtain an expression for the locally averaged flux surface power density

$$p(s) = \frac{\frac{dP(s)}{ds}}{\frac{dV}{ds}} \tag{3.4}$$

where V denotes the volume enclosed by a flux surface. The constant α_s used in the Poynting flux equation 3.1 is given by $\alpha_s = a_s^2(2-a_s)$ [90]. The a_s in this expression stands for the single pass absorption coefficient across the horizontal plane through the magnetic axis. The single pass absorption (SPA) coefficient is given by

$$a_s = \frac{\omega}{2\pi P_x} \int Im(\vec{E}^* \cdot \overline{\varepsilon} \cdot \vec{E}) dx \tag{3.5}$$

Here, Px is the incoming Poynting flux, $*$ denotes a complex conjugated quantity, and the geometry is such that the x-axis goes across the resonance layer and the z-axis goes along the equilibrium magnetic field. The contributions to the SPA coefficient from different particle species are computed using the Wentzel-Kramers-Brillouin (WKB) approximation. In the absence of mode conversion, the WKB approximation is given by

$$a_s = \sum_j a_{sj} = \sum_j \int_{-\infty}^{\infty} \frac{k_0^2}{|k_\perp|} \left\{ Im(\varepsilon_{xx}^j) \left| \frac{\varepsilon_{xy}}{\varepsilon_{xx} - n_\parallel^2} \right|^2 + Im(\varepsilon_{yy}^j) + 2Re(\varepsilon_{xy}^j) Im\left[\frac{\varepsilon_{xy}}{\varepsilon_{xx} - n_\parallel^2} \right] \right\} \times e^{-\int_{-\infty}^{x} 2Im(k_\perp(x'))dx'} dx \tag{3.6}$$

where ε_j represents the contributions to the dielectric tensor from species j and $k_0 = \omega/c$.

The functions representing the strong and weak absorption contributions to the Poynting flux for a resonant ion species, $P_{1j}(s)$ and $P_{2j}(s)$, depend on the following quantities

$$P_{1j} = P_{1j}(s, N, < v_{\parallel j}^2 >), \quad P_{2j} = P_{2j}(s, a_j(s), F(s)) \tag{3.7}$$

Here, $< v_{\parallel j}^2 >$ represents the averaged squared parallel velocity of species j, $a_j(s)$ stands for the absorption strength of species j along the cyclotron resonance and the function $F(s)$ represents the averaged electric wave field strength along the cyclotron resonance in the limit of weak absorption. Therefore, using this expression we can deduce the dependencies of the components on the limit of strong and weak absorption. P_{1j} depends on $< v_{\parallel j}^2 >$, which, as explained in Subsection 2.4.1, determines the Doppler effect. The power deposition of

the strong absorption will therefore depend on the Doppler broadening of the cyclotron resonance and the damping will be focused on the first passage of the wave. P_{2j} depends on the function $F(s)$ representing the strength of the electric wave field. The weak absorption will hence be determined by the wave field distribution and the absorption strength along the cyclotron resonance. The expressions for both direct electron damping mechanisms, ELD and TTMP, are more complicated and can be found in [92].

The treatment of mode converted waves is again challenging. In order to compute the power going to mode conversion, the absorption layer is treated locally in planar geometry and the mode conversion is handled as a resonance absorption according to the Budden model [63]. The power going to mode conversion is then subtracted from the coupled power. Although this is an adequate way to compute mode conversion, it is not expected to be sufficient if there is significant mode conversion. However, improving this modelling has proven to be quite difficult.

3.1.2 The Fokker-Planck Calculation

Now that we have presented the power deposition model in PION, let us consider the next step in this procedure. As explained in Subsection 2.4.2, the evolution of the velocity distribution function is described by the Fokker-Planck equation. However, the full two-dimensional equation is not solved to reduce the computation time. The time-dependent, one-dimensional, pitch-angle-averaged Fokker-Planck equation is given by

$$\frac{\partial f}{\partial t} = \frac{1}{v^2}\frac{\partial}{\partial v}\left[-\alpha v^2 f + \frac{1}{2}\frac{\partial}{\partial v}(\beta v^2 f)\right] + \frac{1}{v^2}\frac{\partial}{\partial v}\left[v^2 D_{RF}\frac{\partial f}{\partial v}\right] + S \tag{3.8}$$

Here, the first term on the right-hand side of the equation is the collision operator describing the collisions with the background plasma, and the second term is the wave-particle operator describing the wave-particle interactions. The S term serves as a source term for the NBI, particularly significant in discharges where beams resonate with the ICRF wave. This term enables the consideration of the synergy between ICRF and NBI (ICRH+NBI synergy), which will be further explored in Chapter 4.

The diffusion coefficient D_{RF} in equation 3.6 is given by

$$D_{RF} = \sum_N K \left| J_{n-1}\left(\frac{k_\perp v_\perp}{\omega_{ci}}\right) + \frac{E_-}{E_+} J_{n+1}\left(\frac{k_\perp v_\perp}{\omega_{ci}}\right)\right|^2 \tag{3.9}$$

where K represents a constant proportional to E_+^2 and the collisional slowing down of the particles is assumed to be classical and is given by the coefficients α and β, found in [57].

From the expressions in equation 3.5 we know that we need to calculate the averaged squared parallel velocity in order to compute the power deposition. $< v_{\|j}^2 >$ is then obtained from an *ad hoc* formula [93]

$$< v_{\|j}^2 >= \frac{\int \mu_{eff}^2 v^2 f(v) dv}{\int f(v) dv} \tag{3.10}$$

where μ_{eff}^2 stands for the effective averaged pitch angle and is approximated as

$$\mu_{eff}^2 = \frac{1}{3} \frac{1 + (\frac{v}{v_*})^2}{1 + (\frac{v}{v_*})^2 + (\frac{v}{v_*})^4} \tag{3.11}$$

Here, $v_* = 0.5 v_\gamma$ where v_γ is a characteristic velocity above which the pitch angle scattering becomes weak. In order to obtain the ratio between v_* and v_γ, equation 3.9 has been fitted to calculations of the effective averaged pitch angle performed with the two-dimensional Fokker-Planck code BAFIC [94].

Special attention should be paid to the instances where the orbit widths are finite. Finite orbit widths (FOW) can have an important effect on ICRF accelerated fast ions. The energy density and the collisional power transfer to the background plasma are two of the quantities that, among others, are significantly affected by FOW. PION takes FOW effects into account by considering the fast ions that have been accelerated by ICRF wave to be trapped. As mentioned in Subsection 2.3.1, the turning points of the orbits of these trapped ions are close to the IC resonance. The fast trapped ions are hence identified with the magnetic flux surface where they have their turning points, located close to where the ion interacts resonantly with the wave field. The collision coefficients α and β needed to compute the one-dimensional Fokker-Planck equation are then averaged over the resulting orbits. The process through which PION deals with FOW is called orbit redistribution. It should be noted that this is an approximate model that may not be fully representing the physical reality when there are energetic passing particles in the fast ion population, such as in the case of a HFS resonance.

3.1.3 Coupling of Focker-Planck and Power Deposition Model

Let us now consider the last step in the modelling of ICRF with PION; the coupling of the two procedures described in this section.

Most of the quantities of interest can be calculated with the model for the distribution function presented above in Subsection 3.1.2. These include the collisional power transfer from the resonating species to the background electrons and the bulk ions, both the parallel and perpendicular energy density and the fusion reactivity. The dielectric tensor components ε_j used in equation 3.4 in the power deposition model are computed using the parameters obtained in the Fokker-Planck calculation. The absorption strength in the deposition model also depends on the distribution function, due to FLR effects. This absorption strength needs to be consistent with the Fokker-Planck calculation. In order to achieve this, the components in the dielectric tensor used in the power deposition are updated in each iteration using the results of the Fokker-Planck calculation, according to the procedure described in [1].

In addition to $< v_{\|j}^2 >$ described in equation 3.8, this model needs three additional parameters. In order to obtain these parameters, we first need to decompose the ICRF diffusion tensor D_{RF} in equation 3.7 into three components. These components are given below for each toroidal mode number N by

$$\begin{aligned} D_{RF,N}^{+} &= K_N \left| J_{n-1}\left(\frac{k_\perp v_\perp}{\omega_{ci}}\right)\right|^2 \\ D_{RF,N}^{-} &= K_N \left| \frac{E_-}{E_+} J_{n+1}\left(\frac{k_\perp v_\perp}{\omega_{ci}}\right)\right|^2 \\ D_{RF,N}^{c} &= 2K_N Re\left[\frac{E_-}{E_+} J_{n+1}\left(\frac{k_\perp v_\perp}{\omega_{ci}}\right) J_{n-1}\left(\frac{k_\perp v_\perp}{\omega_{ci}}\right)\right] \end{aligned} \tag{3.12}$$

Let us now use this decomposition to express the power density absorbed in terms of these components. The power density absorbed by a species j from the interaction with a wave that has a toroidal mode number N is therefore

$$p_{\sigma,N}^{j} = 2\pi m_j \int_0^\infty \frac{1}{v^2}\frac{\partial}{\partial v}(v^3 D_{RF,N}^{\sigma}) f_j v^2 dv, \quad \sigma = +,-,c \tag{3.13}$$

We can now use the expression for the power density absorbed to obtain the three parameters that the model for the power deposition calculation required

$$\gamma_{+,N}^{j} = \frac{p_{+,N}^{j}}{p_{+,N}^{jM}}, \quad \gamma_{-,N}^{j} = \frac{p_{-,N}^{j}}{p_{-,N}^{jM}}, \quad \gamma_{c,N}^{j} = \frac{p_{c,N}^{j}}{p_{c,N}^{jM}} \tag{3.14}$$

Here, the superscript M stands for Maxwellian. This superscript indicates a quantity calculated assuming a Maxwellian distribution function that has the same density as the actual distribution functions but a different temperature given by $kn_jT = \frac{1}{2}m < v_{\|j}^2 >$. Therefore, these three parameters, or γ factors, represent the ratios of the power densities absorbed by the actual distribution functions to the power densities that would have been absorbed by a Maxwellian distribution.

As was explained above, the γ factors obtained here are needed to compute the dielectric tensor in the power deposition model. When neglecting the parallel component of the wave electric field, the dielectric tensor $\overline{\varepsilon}$ can be used to calculate the power density absorbed locally, which is given by

$$\begin{aligned} p_{RF}^j = \frac{\omega}{2\pi} Im(\vec{E}^* \cdot \overline{\varepsilon} \cdot \vec{E}) = \frac{\omega}{2\pi} \{ |E_+|^2 \left[Im(\varepsilon_{xx}^j + \varepsilon_{yy}^j) - 2Re\varepsilon_{xy}^j \right] + \\ |E_-|^2 \left[Im(\varepsilon_{xx}^j + \varepsilon_{yy}^j) + 2Re(\varepsilon_{xy}^j) \right] + 2Re(E_+ E_-^*) Im(\varepsilon_{xx}^j - \varepsilon_{yy}^j) \} \end{aligned} \tag{3.15}$$

Using the γ factors and the expression in 3.13 we can arrive to the relations that need to hold for the absorption strength in the deposition model to be consistent with the Fokker-Planck calculation

$$\begin{aligned} Im(\varepsilon_{xx}^j + \varepsilon_{yy}^j) - 2Re(\varepsilon_{xy}^j) &= \gamma_{+,N}^j [Im(\varepsilon_{xx}^{j,M} + \varepsilon_{yy}^{j,M}) - 2Re(\varepsilon_{xy}^j)] \\ Im(\varepsilon_{xx}^j + \varepsilon_{yy}^j) + 2Re(\varepsilon_{xy}^j) &= \gamma_{-,N}^j [Im(\varepsilon_{xx}^{j,M} + \varepsilon_{yy}^{j,M}) + 2Re(\varepsilon_{xy}^j)] \\ Im(\varepsilon_{xx}^j - \varepsilon_{yy}^j) &= \gamma_{c,N}^j [Im(\varepsilon_{xx}^{j,M} - \varepsilon_{yy}^{j,M})] \end{aligned} \tag{3.16}$$

Finally, the equations above can now be employed to calculate the anti-Hermitian components of the dielectric tensor ε^A and express them in terms of the γ factors and the Maxwellian contributions, which can be found in [63], for example; $Im(\varepsilon_{xx})$, $Im(\varepsilon_{yy})$ and $Re(\varepsilon_{xy})$. PION uses a simplified approximation to calculate the corrections in the Hermitian parts ε^H due to the difficulty of the task [1].

3.2 The European Transport Solver

Now that we understand how ICRF heating can be modelled with the PION code, let us present a brief description of ETS, how it fits in the IMAS framework, how it treats data and why is relevant for PION to be integrated into its workflow.

Including all the complexities of fusion physics into one *master equation* is impossible. However, interconnecting the description of diverse subaspects through a *backbone* is feasible. Numerical codes utilize this *backbone* or framework by accessing a shared and standardized database during computations, and they feed back the output into it. The EUROfusion Integrated Modelling and Analysis Suite (IMAS) [84] provides this framework.. This aforementioned database, akin to experimental data, comprises *shots* where users can load parameters into their specific codes at designated times [36]. These codes, compiled as *actors*, exhibit flexibility through a *Kepler* [95] graphical user interface. The common input and output structure allows the interchange of codes investigating specific physics aspects, a feature crucial for cross-checking codes grounded in the same physics. Moreover, it enables the use of specific codes for scenarios necessitating special attention, fostering adaptable testing and modeling. Notably, the ETS [3, 4] holds a pivotal role in this framework.

The ETS encompasses equilibrium solvers, auxiliary heating modules, magnetohydrodynamics (MHD) simulators, and transport equation solvers. Particle and energy source inputs are essential for these transport solvers. A range of available H&CD codes includes those for ECRH, ICRH and NBI solvers. It interfaces with data banks of nuclear cross-sections to precisely estimate neutron production in D–T plasmas. The RF heating tools in the ETS are specifically designed for scenarios involving the simultaneous heating of various species, accounting for the interplay of minority and majority non-Maxwellian populations when computing power source terms for the transport equation [36].

The ETS is a modular package of physics modules combined into a workflow, where PION has been included as one of the H&CD actors. Other heating codes have been integrated into the ETS as H&CD actors, including CYRANO [96] or StixRedist [97]. The ETS has been developed with the objective of building the capabilities to compute the full discharge evolution of a power plant scale tokamak. To meet this objective, the ETS counts with a high degree of modularity, a separation of physics and numeric parts, a flexible workflow, and the ability to both treat several ion components (including impurities) and use stiff transport models [3].

The ETS is formed out of coupled codes where the information exchange takes place through well-defined generalized Identical Data Structures (IDSs) acting as standardized

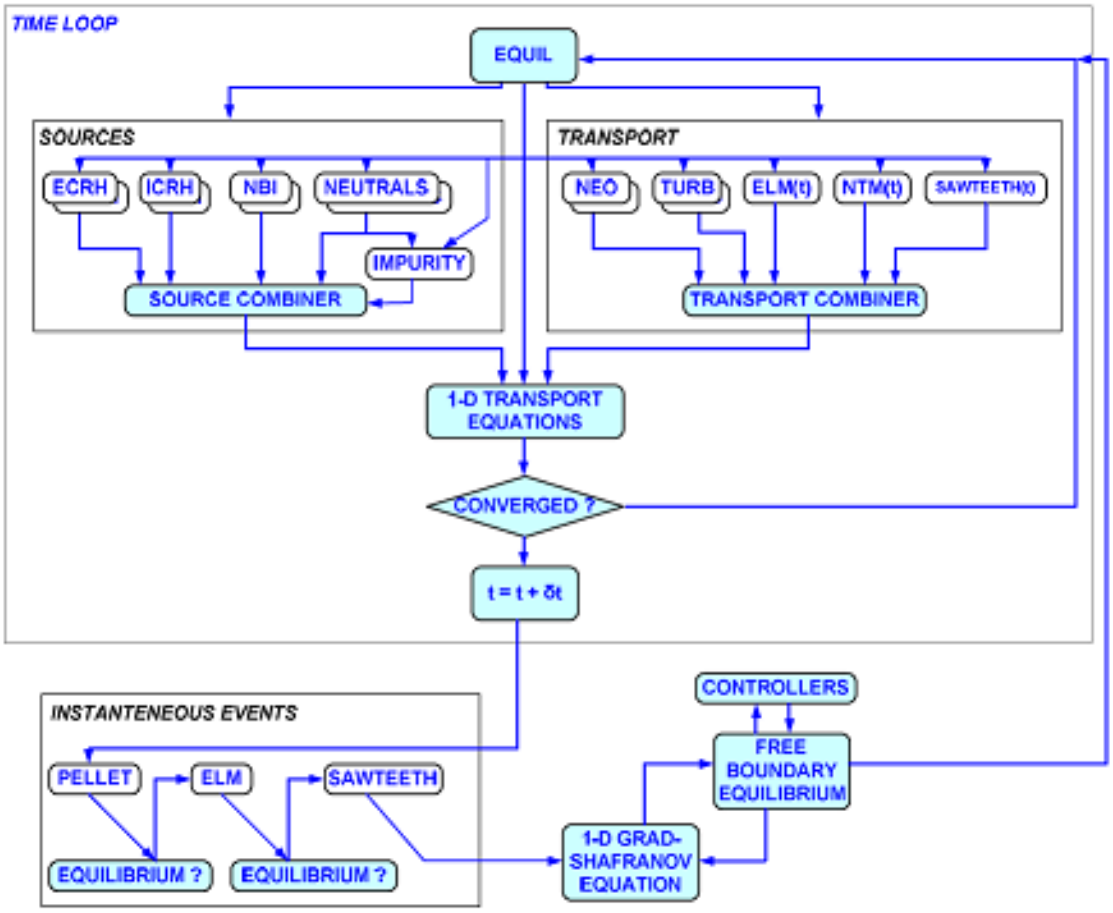

Fig. 3.2 *Flowchart of the ETS workflow [85].*

interfaces [4]. This is the standard layered structure used in IMAS, where the reactor data model is mapped to the solver data model through the IDSs. The IDSs contain physics definitions of the equilibrium, neoclassical transport and core sources, transport, impurities, and profile. The IDS equilibrium represents the equilibrium at the previous time step, the IDS core source represents the sources of current, electron and ion energy, momentum, and particles, whereas the IDS core transport represents the transport coefficients of these quantities.

In each iteration, the ETS core code reads the input from the equilibrium, core source and transport IDSs, as well as the core profile representation of the plasma state at the previous time step. The ETS then passes the input to the physics modules, which solve the transport equations for the density of current, the ion and electron density, the ion and electron temperature and the toroidal velocity. The core code will then output a core profile containing a new plasma state. The flowchart of the ETS workflow is shown in Figure 3.2.

The ETS functions as a suite of validated codes containing several transport actors integrated into its workflow which use different models, such as neoclassical and gyrokinetic transport models. The older actors use a neoclassical transport model, which uses the kinetic equation for the mean particle distribution function to describe the plasma and computes a closed set of fluid equations that describe the time evolution of the moments of particle density, flux, stress and pressure tensor and energy and heat flux [98]. This model takes into account geometrical effects such as drifts and banana orbits, but ignores micro-instabilities driven turbulence transport.

The newer actors use a gyrokinetic transport model, which again uses the evolution of the distribution function based on the Vlasov equation, but introduces a simplification; instead of accounting for the full orbit of the particle, it decomposes it into a rapid gyration about the magnetic field lines and a slow drift of the gyro centre [99]. The averaging over the angle of gyration allows the gyrokinetic equation to have one less dimension than the Vlasov equation and to account for the effects of turbulence.

The physics model of the ETS is based on the model in ASTRA [100], a standard, one-dimensional transport model. The ETS solves transport equations for the poloidal flux, the temperature and density of the ion species, the electron temperature and the toroidal rotation. The physics and numeric solvers of ETS are decoupled to allow same physics to be described by different numerical solutions

Chapter 4

Modelling of ICRH with PION+ETS

4.1 Introduction

The objective of this Chapter is to use the modelling tools presented in Chapter 3 to obtain predictions about the performance of the ICRF heating schemes that will be used to reach fusion-relevant temperatures in a number of ITER plasmas pertinent to the PFPO phase. These heating schemes have been analysed in [5–8] with different modelling tools, but the results presented here are the first ever results of the PION+ETS integration. These findings add depth to the existing knowledge obtained from previous simulations conducted with different ICRH modelling tools. By employing a novel approach, there is potential to uncover previously unnoticed nuances of these scenarios. This not only enriches our understanding but also validates and supplements findings from other modeling tools. Furthermore, the introduction of the PION+ETS integration allowed for the exploration of self-consistent simulations, as opposed to the fixed plasma parameters employed in the existing literature, leading to a more comprehensive assessment of the plasma behaviour in these scenarios. Overall, the results presented here demonstrate the value of using the PION+ETS integration to study these ITER scenarios, offering fresh insights into ICRF heating ITER scenarios that complement existing knowledge.

In this Chapter, the results of the modelling performed with the PION+ETS integration are presented. All the simulations performed are self-consistent, predictive and time-dependent. The Chapter is divided into three sections corresponding to the three tokamaks studied; ITER, JET and AUG. In Section 4.2, the results of simulations with ITER synthetic *shots* are presented. Three scenarios with different ICRF heating schemes are analysed. In Section 4.3, results for a JET baseline discharge are shown. The effects of ICRF heating, NBI heating and

the ICRF+NBI synergy mentioned in Subsection 3.1.2 are investigated. In the last section, the results of an AUG scenario are presented.

The focus of these simulations is on bulk ion heating. As it was explained in Subsection 2.3.1, bulk ion heating enhances fusion reactivity, so achieving good bulk ion heating is relevant for any fusion experiment. Special attention is also given to the gas mixture sensitivity. Density scans of the minority concentrations are performed for every scenario.

The reporting on the scenarios is structured as follows: first, an overview of the discharge used for the simulation is given. The basic plasma parameters and *shot* information are provided. Then, the power density absorption profile is presented. The power density absorbed by each resonant ion species ($P_{abs,i}$) and by the electrons ($P_{abs,e}$) as a function of the normalized flux surface as calculated by PION is studied, and the SPA coefficients, which measure how much of the ICRF wave is absorbed the first time it travels through the plasma, are given. After this, the collisional power transfer profiles given by PION are presented and analysed. The power equipartition between bulk ion heating (P_{ci}/P_c) and electron heating (P_{ce}/P_c) is discussed, as well as the critical energy (E_{crit}) and the average energy of the fast resonant ions ($\langle E_{fast,i} \rangle$). Finally, the evolution of the thermal ions temperature as calculated by PION+ETS is displayed.

Additional analysis includes a discussion of the energy distribution functions of the resonating ions at the normalized flux surface of the ICRF resonance and at the adjacent flux surfaces. The electron temperature evolution is evaluated. The density of the D neutrals from the NBI beams (n_D) as a function of the normalized flux surface, as well as the time evolution of the H&CD sources, is also given.

It should be noted that when speaking about *shots* or *discharges* in the following sections, it refers to the information and parameters present in the IDS (as explained in Section 3.2) of a specific tokamak plasma discharge. When speaking about *ramp-up* and *flat-top*, it denotes the phases of a plasma discharge; the ramp-up phase involves gradually increasing plasma current, temperature, and density, while the subsequent flat-top phase maintains stable levels of these parameters to sustain fusion reactions [101]. *On-axis* refers to a location along the central axis of the toroidal region, whereas *off-axis* refers to a position away from this central axis.

4.2 Minority Scenarios at ITER

4.2.1 Overview

In this section, three ITER ICRF minority scenarios are investigated and the results are presented. These scenarios were chosen based on the ITER Research Plan [5–8] and in the available discharges in the ITER database.

According to the ITER Research Plan, before reaching operations at full field (5.3 T), plasma scenarios at half field (2.65 T) and third field (1.8 T), as well as progressive steps (3.3 T) towards full field, will be investigated in the PFPO phase [29]. In this thesis, as mentioned in Section 1.2, the focus is on the ICRF scenarios with H and He plasmas investigated before reaching full field operation with D and T plasmas.

Let us now consider the possible ICRF heating schemes for H and He plasmas at 2.65 T, 3.3 T and 1.8 T. For a magnetic field of 2.65 T, taking into account that the accessible range of ICRF wave frequencies at ITER is 40-55 MHz, there is no efficient ICRF scheme for H plasmas [7]. The best candidate for He plasmas is fundamental minority H heating. To address the absence of an effective ICRF heating scheme in H plasmas at 2.65 T, a potential solution is to use the three-ion scheme, heating a small concentration of ^{3}He (<1%) in a H:^{4}He mixture, at its fundamental resonance of 40 MHz, at 3.3 T [59]. For a magnetic field of 1.8 T, the most efficient ICRF scheme for H plasmas is 2$^{\text{nd}}$ H harmonic majority heating, whilst for He plasmas it is 2$^{\text{nd}}$ H harmonic minority heating. However, PION has not been extensively tried on inverted minority scenarios, so the H plasma majority scheme was dismissed.

The chosen ICRF scenarios are summarised in Table 4.1; fundamental H ($\omega = \omega_H$) minority heating in ^{4}He plasma at 2.65 T is referred to as Scenario 1, 2$^{\text{nd}}$ H harmonic ($\omega = 2\omega_H$) minority heating in ^{4}He plasma at 1.8 T is referred to as Scenario 2 and fundamental ^{3}He heating ($\omega = \omega_{^3He}$) in a three-ion-scheme in H plasma at 3.3 T is referred to as Scenario 3.

Table 4.1 *Overview of the ICRF schemes studied in this section, including Scenario, magnetic field (B_0), main plasma ion, heating scheme and ICRF wave frequency (f)*

Scenario	B_0 (T)	Main Ion	Heating Scheme	f (MHz)
1	2.65	^{4}He	$\omega = \omega_H$	40
2	1.8	^{4}He	$\omega = 2\omega_H$	53
3	3.3	H	$\omega = \omega_{^3He}$	40

4.2.2 Scenario 1: Fundamental H Minority Heating in ^{4}He Plasma at 2.65 T

For the study of fundamental H ($\omega = \omega_H$) minority heating in ITER ^{4}He plasma, synthetic ITER *shot* 110005 with a pulse duration of 647 s was used. The plasma was heated using 20 MW of ICRF, 24 MW of NBI and 20 MW of ECRH. The PION+ETS simulation was started during the flat-top phase, at $t_i = 300$ s, with the plasma and ICRF parameters as shown in Table 4.2. An ICRF frequency of 40 MHz was chosen to place the fundamental H resonance in the plasma center. The ICRF power of 20 MW was chosen based on the ITER Research Plan. In the simulation set-up, the temperature evolution of the ions and electrons was set to be predictive, whilst the density evolution was set to be interpretative. The chosen transport model uses a combination of a neoclassical model and a multi-ion model. The H concentrations have been elected in order to replicate the results obtained by [5]. All results hereafter are shown in terms of these minority concentrations of 1.0, 2.5, 5.0 and 10%. These percentages are calculated in terms of the electron density shown in Table 4.2. The simulation was performed with a full antenna spectrum of 100 toroidal mode numbers N, out of which the toroidal mode number N = 54 is considered when giving the SPA coefficients. Finally, the duration of the simulation was chosen to be 8 s to allow ample time for the evolution of the plasma towards a new steady state.

Table 4.2 *Plasma composition (with the minority ion species in brackets), heating scheme, magnetic field (B_0), ICRF frequency (f), ICRF power (P_{ICRF}) and central electron and ion temperatures and densities, where n_i refers to the majority ion density at a H concentration of 1.0%.*

Plasma	Heating Scheme	B_0 (T)	f (MHz)	P_{ICRF} (MW)	$n_e^0 x10^{19}$ (m^{-3})	$n_i^0 x10^{19}$ (m^{-3})	T_e^0	T_i^0
^{4}He-(H)	$\omega = \omega_H$	2.65	40	20	3.3	1.6	10	11

Figure 4.1 shows the temperature and density profiles for both electrons and ions. The temperature for every profile decreases gradually as it approaches the edge of the plasma at $s = 1.0$. The small discontinuity seen close to $s = 0.9$ is a consequence of the transport model used, which considers the transport equations from $s = 0$ to $s = 0.9$. The initial ion temperature is slightly higher than the initial electron temperature (T_i^0 = 12 keV as compared to $T_e^0 = 10$ keV). The temperatures at the end of the simulation are very similar to each other, due to the thermalisation of the plasma. It should be noted that T_e increases by a higher percentage (60%) than T_i (40%) after plasma relaxation. We can see that there is no difference in the temperature profiles for the H concentrations considered, apart from

a slight initial change in the T_e profile and a larger difference in the T_i profile close to the ICRF resonance. The density profiles are only shown at the beginning of the simulation because their evolution was set to be interpretative and there is no relevant change after thermalisation.

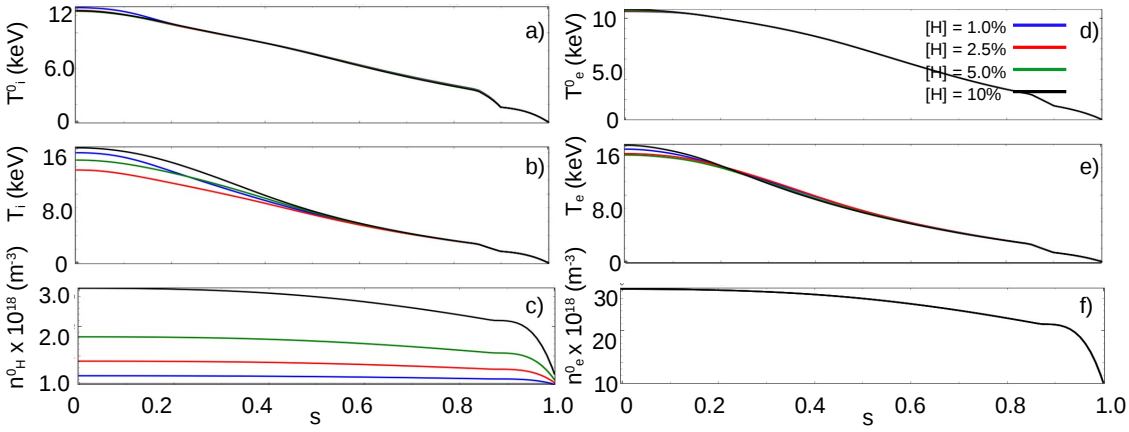

Fig. 4.1 *Overview of ITER discharge 110005 for H concentrations of [H]= 1.0, 2.5, 5.0 and 10%. a) Temperature of the ions at the start of the simulation (T_i^0), b) temperature of the ions at the end of the simulation (T_i), c) density of the H ions at the start of the simulation (n_H^0), d) temperature of the electrons at the start of the simulation (T_e^0), e) temperature of the electrons at the end of the simulation (T_e) density of the electrons at the start of the simulation n_e^0.*

Figure 4.2 shows the power density absorption profile as given by PION+ETS at $t_f = 308$ s. There are three competing absorption mechanisms, i.e., fundamental H damping, 2nd ^{4}He harmonic damping and direct electron damping. Among them, the fundamental H absorption is the dominant mechanism, with a resonance located at the normalized flux surface $s = 0.03$. As shown by Figure 4.2, most of the ICRF power is absorbed by resonating H ions independently of the H concentration. The fundamental H absorption takes place in the LFS of the plasma, with a second peak slightly shifted to the right, closer to $s = 0.20$. Figure 4.2 also shows the SPA coefficients for H absorption at the resonance with respect to the dominant toroidal mode number $N = 54$. As we can see from Figure 4.2, the SPA on H increases with the H concentration in the range of concentrations considered (1.0 - 10%). For the lowest H concentration of 1.0%, the SPA on H is low enough (85%) for significant ^{4}He absorption (19% of the ICRF power c.f. Table 4.3), to take place. The ^{4}He absorption arises because the chosen ICRF frequency also coincides with the 2nd ^{4}He harmonic resonance ($\omega = 2\omega_{^4He}$). Consequently, when H damping decreases as the H concentration is decreased, absorption by majority ^{4}He ions starts to compete with the dominant H damping. As

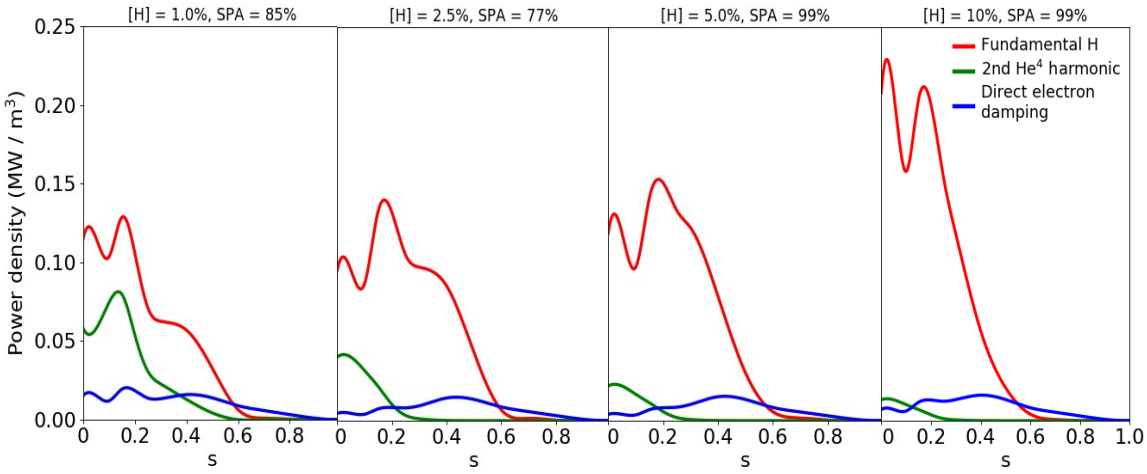

Fig. 4.2 *ICRF power density absorbed by fundamental H (red), 2nd ^{4}He harmonic (green), and direct electron damping (blue) as a function of the normalized flux surface, s, at $t_f = 308$ s for H concentrations of 1.0, 2.5, 5.0 and 10%. SPA coefficients on H at the resonance and toroidal mode number N=54 are given in the legends.*

shown by Figure 4.2, direct electron damping absorbs around 20% of the ICRF wave power independently of the H concentration, and takes place mainly off-axis.

Table 4.3 *H concentrations, power absorbed by resonant H and ^{4}He ions and electrons ($P_{abs,H}$, $P_{abs,e}$, $P_{abs,^4He}$), fractions of collisional power transferred from resonant ions to bulk ions (P_{ci}/P_c) and background electrons (P_{ce}/P_c), critical energy (E_{crit}) and average energy of the fast H ions ($\langle E_{fast,H} \rangle$) as given by PION+ETS for Scenario 1 with different H concentrations.*

H (%)	$P_{abs,H}$ (MW)	$P_{abs,e}$ (MW)	$P_{abs,^4He}$ (MW)	P_{ci}/P (%)	P_{ce}/P (%)	E_{crit} (keV)	$\langle E_{fast,H} \rangle$ (keV)
1.0	11.5	4.52	3.92	34.2	65.8	158	1719
2.5	15.2	3.90	0.73	26.8	73.2	153	568
5.0	15.6	3.90	0.40	39.9	60.1	154	366
10	15.7	4.16	0.25	48.8	52.2	173	459

In terms of the collisional power transfer shown in Figure 4.3, collisional transfer to electrons dominates over bulk ion heating in all cases. The average energy of the H ions in the tail of the fast ion distribution function is higher (in the range of 459 - 1719 keV c.f. Table 4.3) than their critical energy (158 - 173 keV) for all H concentrations considered. Therefore, and as explained in Subsection 2.3.1, the H ions will collide mainly with the electron population and transfer their energy to them. As the H concentration is increased to 10%, the average energy of the fast H decreases until $\langle E_{fast,H} \rangle \sim 2.5 E_{crit}$, resulting in a balanced power equipartition and $P_{ci}/P_c \sim 0.5$, which agrees with the equation for total

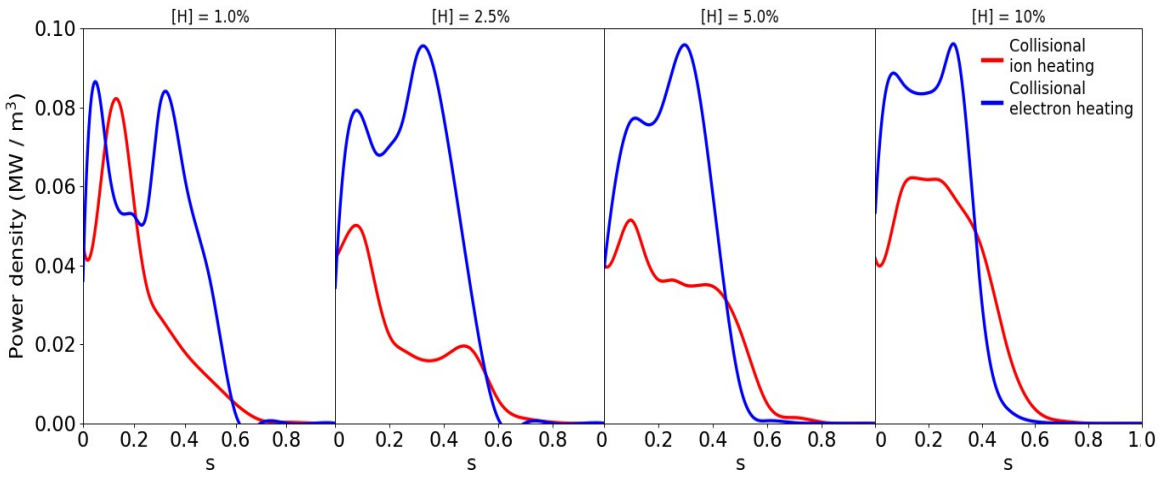

Fig. 4.3 *Orbit redistributed collisional power transferred by the resonant ion species to bulk ions (red) and electrons (blue) at* $t_f = 308$ *s.*

energy given up by the resonant particles transferred into the thermal ions of the plasma in [102]. It can be noted that the double peaks present in the fundamental H damping profiles in Figure 4.2 are also visible in the collisional power to electron profile (P_{ce}). This similitude takes place because the fast ions transfer most of their power to the background electrons, and therefore both profiles follow a similar pattern with respect to the normalized flux surface.

Figure 4.4 shows the time evolution of the thermal ion temperature at the location of the ICRF resonance at the normalized flux surface $s = 0.03$. Thermal ions here refers to the temperature of the bulk ions in the plasma after colisional relaxation, as opposed to the temperature of the fast, ICRF accelerated ions. The results suggest that at lower H concentrations the time evolution of the plasma is more non-linear due to the evolution of the ICRF power deposition in time when the fast resonant ion populations build up. We note, however, the transient evolution in the first seconds of the simulations shown in Figure 4.4 depends on the parameters used in the transport model and may not be observed experimentally.

Moreover, it takes a surprisingly long time for the plasma to reach a new steady state. Although it depends on the H concentration, Figure 4.4 shows that the plasma needs about 6 s to reach the new steady state. This time scale is roughly 3 times the ion-electron slow-down time (mentioned in Subsection 2.3.2) of the resonant particles, τ_{se} = 2.25 s at the resonance $s = 0.03$. The ion-ion slowing down time for this plasma is τ_{si} = 0.01 s, and the energy confinement time is $p\tau_E = 0.68$ s, given here at the resonance. The temperatures at the end of the simulation at $t_f = 308$ s are in the range of 11.9 - 15.0 keV, with the lowest T_i = 11.9 keV at a H concentration of 2.5% and the highest T_i = 15.0 keV at a H concentration of 10%.

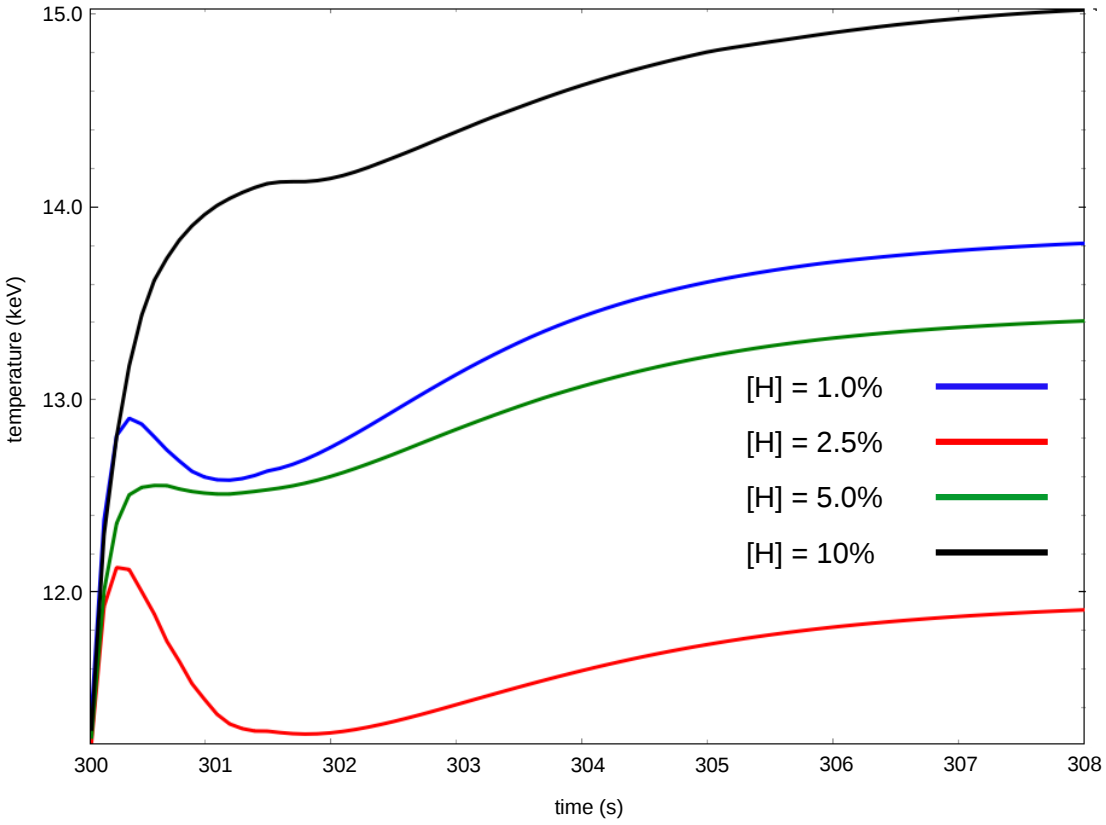

Fig. 4.4 *Time evolution of the thermal ions temperature at the normalized flux surface* $s = 0.03$ *where the ICRF resonance is located, from* $t_i = 300$ *s to* $t_f = 308$ *s, for H concentrations of 1.0, 2.5, 5.0 and 10%.*

As shown in Figure 4.4, the ion temperature increases as the H concentration increases in the range 2.5 to 10 %. The exception to this trend is the case with a H concentration of 1.0% for which the ion temperature is higher than that for a H concentration of 5.0% and higher than for a H concentration of 2.5%. At the low H concentration of 1.0%, 2^{nd} ^{4}He harmonic damping is significant as discussed above and contributes mainly to collisional bulk ion heating. Moreover, it has a more peaked absorption profile around the resonance located at $s = 0.03$. This explains its relatively good performance in terms of bulk ion heating and thermal ion temperature.

4.2.3 Scenario 2: 2nd H Harmonic Minority Heating in ^{4}He Plasma at 1.8 T

For the study of 2nd H harmonic ($\omega = 2\omega_H$) minority heating in ITER ^{4}He plasma, synthetic ITER *shot* 114102 was used. The plasma was heated using 30 MW of ECRH. This *shot* has one time slice, so the PION+ ETS simulation was started there during the flat-top phase, at $t_i = 255$ s, with the plasma and ICRF parameters as shown in Table 4.4. An ICRF power of 20 MW and a frequency of 53 MHz were chosen to place the 2nd H harmonic resonance in the plasma center. In the simulation set-up, the temperature evolution of the ions and electrons was set to be predictive, whilst the density evolution was set to be interpretative. The transport model and the antenna spectrum configuration are the same as in Scenario 1. Minority concentrations from 1.0% and up to 20% are considered in this case to investigate better absorption at higher concentrations. Finally, the duration of the simulation was chosen to be 7 s to allow ample time for the evolution of the plasma towards a new steady state.

Table 4.4 *Plasma composition (with minority species in brackets), heating scheme, magnetic field (B_0), ICRF frequency (f), ICRF power (P_{ICRF}) and central electron and ion temperatures and densities, where n_i refers to the majority ion density at a H concentration of 1.0%.*

Plasma	Heating Scheme	B_0 (T)	f (MHz)	P_{ICRF} (MW)	$n_e^0 x10^{19}$ (m^{-3})	$n_i^0 x10^{19}$ (m^{-3})	T_e^0	T_i^0
^{4}He-(H)	$\omega = 2\omega_H$	1.8	53	20	3.1	1.5	10	5.4

Figure 4.5 shows the temperature and density profiles for electrons and ions. The initial electron temperature is significantly higher than the initial ion temperature (T_e^0 = 10 keV as compared to T_i^0 = 5.4 keV). The ion temperatures at the end of the simulation are closer to the electron temperatures, but the thermalisation of the plasma is not enough to bring them to the same value. However, T_i increases by a higher percentage (140%) than T_e (60%) after plasma relaxation. The larger differences in temperature due to the H concentration are seen here in the T_e profile, not in T_i as was the case in Scenario 1.

Figure 4.6 shows the power density absorption profile as given by PION+ETS at $t_f = 262$ s. The competing absorption mechanisms in this scenario are 2nd H harmonic damping and direct electron damping. The 2nd H harmonic resonance is the dominant mechanism of ICRF wave absorption for all concentrations above 1.0%, with a resonance at $s = 0.24$. The 2nd H harmonic absorption takes place in the LFS of the plasma and off-axis for the H concentrations above 1.0%. As we can see from Figure 4.6, the SPA is lower for the H concentration of 1.0% (77%) than for every H concentration above (99%). The fact that the SPA is lower is the reason for the significant electron damping (72% c.f. Table 4.5) that

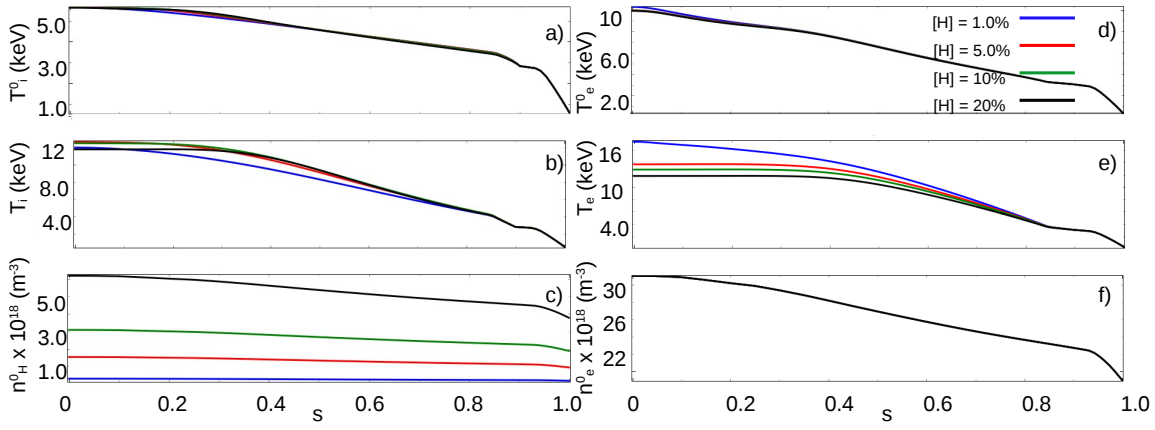

Fig. 4.5 *Overview of ITER discharge 114102 for H concentrations of [H]= 1.0, 5.0. 10 and 20%. a) Temperature of the ions at the start of the simulation (T_i^0), b) temperature of the ions at the end of the simulation (T_i), c) density of the H ions at the start of the simulation (n_H^0), d) temperature of the electrons at the start of the simulation (T_e^0), e) temperature of the electrons at the end of the simulation (T_e) density of the electrons at the start of the simulation n_e^0.*

takes place at this lowest concentration. It should be noted that the SPA given here is not the total SPA, but the SPA with respect to the dominant toroidal mode number. Here, the electron damping takes place over the whole radial profile, but it is most intense on-axis for a H concentration of 1.0%, where the electron temperature and density are highest [103]. For the higher concentrations, both absorptions take place off-axis, closer to $s = 0.5$. From the results in Table 4.5 we can see the trend of increasing power absorbed by the 2$^{\text{nd}}$ H harmonic resonance with increasing H concentration, with a maximum of 63% at a H concentration of 20%. It is worth noting that for these concentrations the absorption profiles are quite broad as compared to the profiles at a H concentration of 1.0%. This might be explained in terms of higher-order FLR effects.

It was mentioned in Subsection 2.2.1 that FLR effects are relevant for damping at both the fundamental and the harmonic ion cyclotron resonance, although these effects are more important in the case of harmonic heating, since the absorption mechanism depends on them to the lowest order. Higher-order FLR effects can cause the diffusion coefficient (equation 3.7) to become small, and the wave particle interaction to become weak at certain energies, preventing the resonating ions from reaching higher energies [69]. Since the power density absorbed (equation 3.11) depends on the components of the diffusion tensor, if FLR effects have an effect on the velocity distribution function of the resonating ions, they can also play a role in the absorption strength. Figure 4.7 shows the velocity distribution functions of the H resonating ions, at three magnetic flux surfaces (the ICRF resonance and the two adjacent

surfaces) for the H concentrations considered. For the H concentrations above 1.0%, the distribution function decreases sharply before 2.0 MeV. Figure 4.7 shows that, due to FLR effects, the tail of the fast ions has a *barrier* in the energy which prevents the resonating ions from reaching a higher energy. This can determine the power deposition width.

Table 4.5 *H concentrations, power absorbed by resonant H ions and electrons ($P_{abs,H}$, $P_{abs,e}$), fractions of collisional power transferred from resonant ions to bulk ions (P_{ci}/P_c) and background electrons (P_{ce}/P_c), critical energy (E_{crit}) and average energy of the fast H ions ($\langle E_{fast,H} \rangle$) as given by PION+ETS for Scenario 2 with different H concentrations.*

H (%)	$P_{abs,H}$ (MW)	$P_{abs,e}$ (MW)	P_{ci}/P_c (%)	P_{ce}/P_c (%)	E_{crit} (keV)	$\langle E_{fast,H} \rangle$ (keV)
1.0	5.56	14.2	21.3	78.7	164	639
5.0	10.5	9.50	39.1	60.9	132	168
10	11.5	8.44	49.3	50.7	128	85.1
20	12.5	7.30	57.5	42.5	64.7	61.0

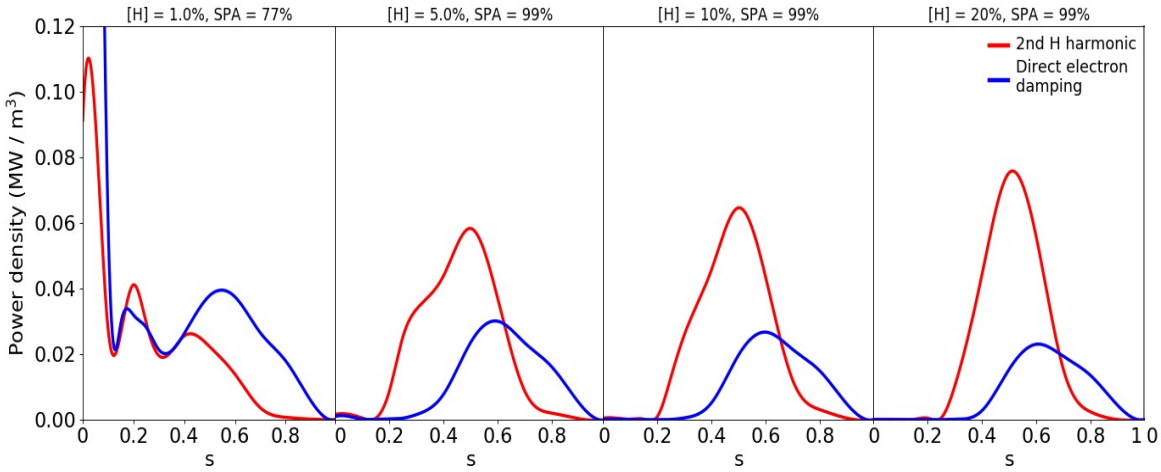

Fig. 4.6 *ICRF power density absorbed by fundamental H (red) and direct electron damping (blue) as a function of the normalized flux surface, s, at $t_f = 262$ s for H concentrations of 1.0, 5.0, 10 and 20%. SPA coefficients on H at the resonance and toroidal mode number N=54 are given in the legends. Direct electron damping has been purposely cut off in the [H] = 1.0% case to allow closer examination of the ionic power deposition profile.*

In terms of the collisional power transfer shown in Figure 4.8, there is dominant electron heating for all H concentrations considered apart from the highest H concentration at 20%. The average energy of H ions in the tail of the fast ion distribution function surpasses their critical energy (64.7 - 164 keV) for lower H concentrations of 1.0 - 5.0%, falling within the range of 61.0 - 639 keV (see Table 4.5). Therefore, the H ions will collide mainly with the electron population and transfer their energy to them. As the H concentration is increased

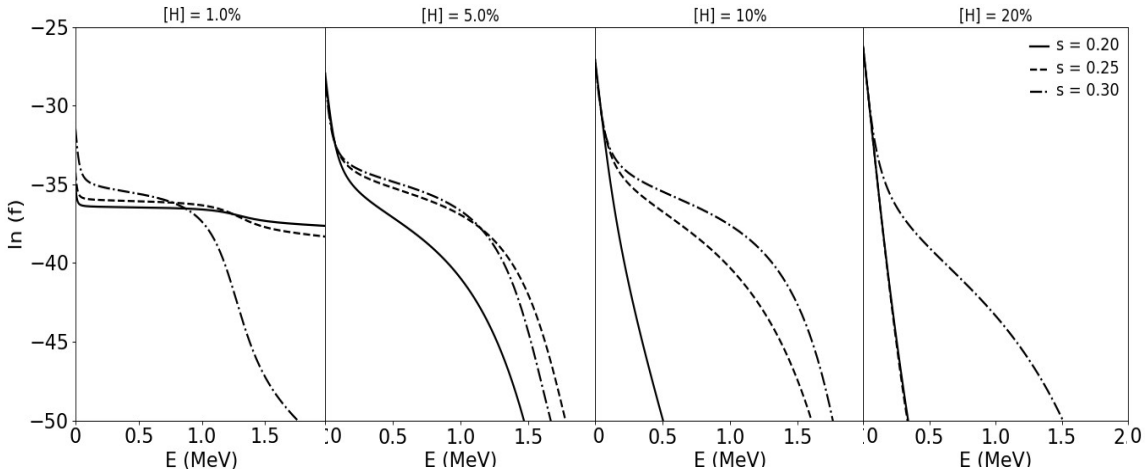

Fig. 4.7 *Velocity distribution functions of the resonating H ions at the normalized flux surface, s, of the ICRF resonance and the two closest flux surfaces, at $t_f = 262$ s for H concentrations of 1.0, 5.0, 10 and 20%.*

to 10%, the average energy of the fast H decreases until $\langle E_{fast,H} \rangle \sim 1.5 E_{crit}$, resulting in an equivalent ICRF power equipartition and $P_{ci}/P_c \sim 0.5$. For the highest H concentration of 20%, $\langle E_{fast,H} \rangle \sim E_{crit}$, therefore there is dominant bulk ion heating. It is worth noting, similarly to Scenario 1, how closely the P_{ce} profiles follow the profiles of the H power deposition, except for the profiles at a H concentration of 1.0%, even though the P_{ce} profiles are subjected to FOW effects.

The P_{ce} profile at a H concentration of 1.0% in Figure 4.7 shows some visible undulations, most notably from s = 0.1 to s = 0.6, absent in the P_{ce} profiles for the rest of minority concentrations. These distinct peaks might again be due to a simplified model to take into account FOW effects of the resonating particles. As it was explained in Subsection 3.1.2, when PION encounters FOW, it performs an orbit redistribution. Through this process, when the width of the particle orbit is finite and crosses different flux surfaces, the power is redistributed between these flux surfaces. Therefore, the FOW effects that can be seen in Figure 4.7 are probably a consequence of the approximate orbit redistribution model that PION uses to compute FOW.

Figure 4.9 shows the time evolution of the thermal ion temperature at the location of the ICRF resonance at the normalized flux surface $s = 0.24$. The results suggest that the time evolution of the plasma is quite linear for all H concentrations considered, as compared to Scenario 1 studied above. The temperatures at the end of the simulation at $t_f = 262$ s are in the range of 11.0 - 12.3 keV, with the lowest T_i = 11.0 keV at a H concentration of 1.0% and the highest T_i = 12.3 keV at a H concentration of 10%. As shown in Figure 4.8,

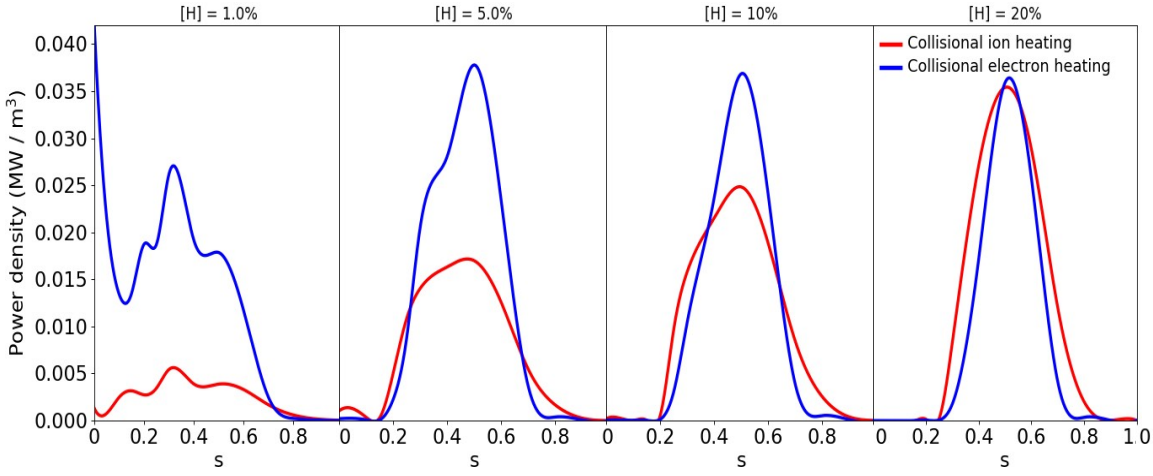

Fig. 4.8 *Orbit redistributed collisional power transferred by the resonant ion species to bulk ions (red) and electrons (blue) at* $t_f = 308$ *s.*

the ion temperature increases as the H concentration increases in the range 1.0 to 10 %. The exception to this trend is the case with a H concentration of 20%, for which the ion temperature is close to that of a H concentration of 5.0%. This is an interesting difference with Scenario 1, where the minority concentration with the largest absorption efficiency yielded the highest thermal temperature. In this scenario, however, the highest temperature is not obtained with the most efficient concentration in terms of absorption. This could be explained in terms of the absorption and collisional profiles at the resonance $s = 0.24$. At this location, there is more ICRF power absorbed by the ions at a H concentrations of 5.0 and 10%. This is the case with the collisional profiles as well, where there is more power going to the ion channel for the H concentrations of 5.0 and 10% than for 20% at the resonance. Hence at the specific s location where the thermal temperature is shown, both of these concentrations yield a higher temperature than the highest minority concentration.

Figure 4.10 shows the time evolution of the electron temperature at the location of the ICRF resonance at the normalized flux surface $s = 0.24$. The temperatures at the end of the simulation at $t_f = 262$ s are in the range of 12.0 - 16.0 keV, with the lowest T_e = 12.0 keV at a H concentration of 20% and the highest T_e = 16.0 keV at a H concentration of 1.0%. As shown in Figure 4.10, the electron temperature increases as the H concentration decreases. The case with a H concentration of 1.0% has the largest electron damping, as well as largest difference between critical energy and average energy of the fast H ions ($\langle E_{fast,H} \rangle \sim 4E_{crit}$), resulting in the highest electron temperature. It should be noted that every profile decreases in temperature before starting to increase after 0.5 s, except from the case with a H concentration of 1.0%. This might be the case because the T_e evolution in

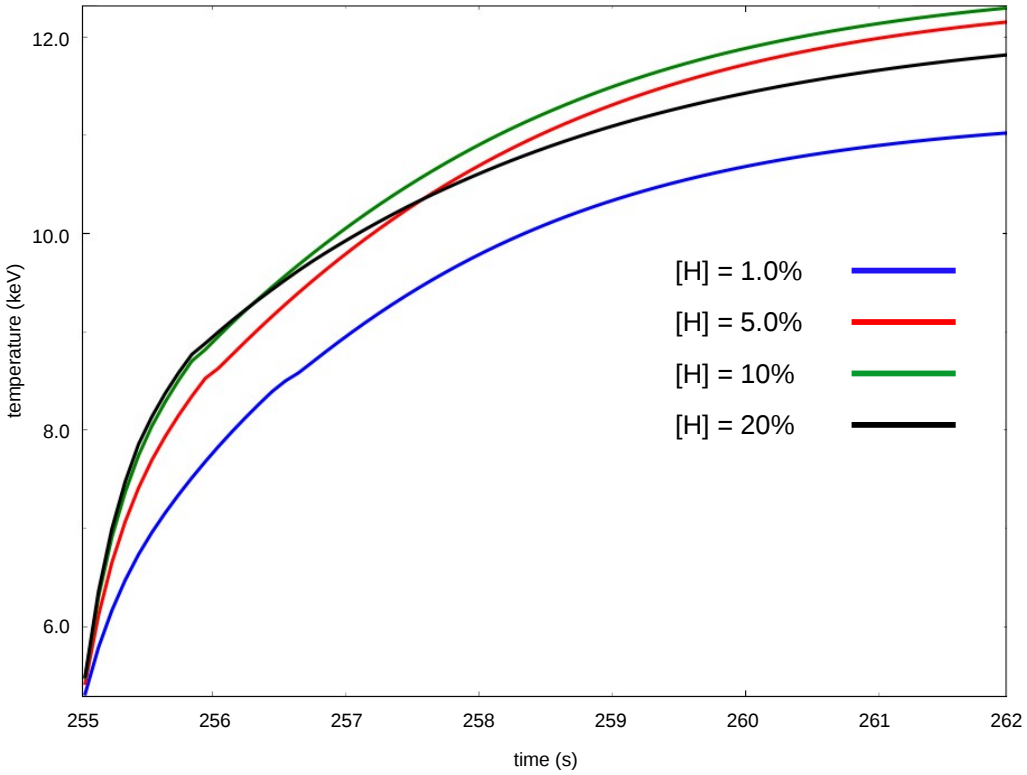

Fig. 4.9 *Time evolution of the thermal ion temperature at the normalized flux surface* $s = 0.24$ *where the ICRF resonance is located, from* $t_i = 255$ *s to* $t_f = 262$ *s, for H concentrations of 1.0, 5.0, 10 and 20%.*

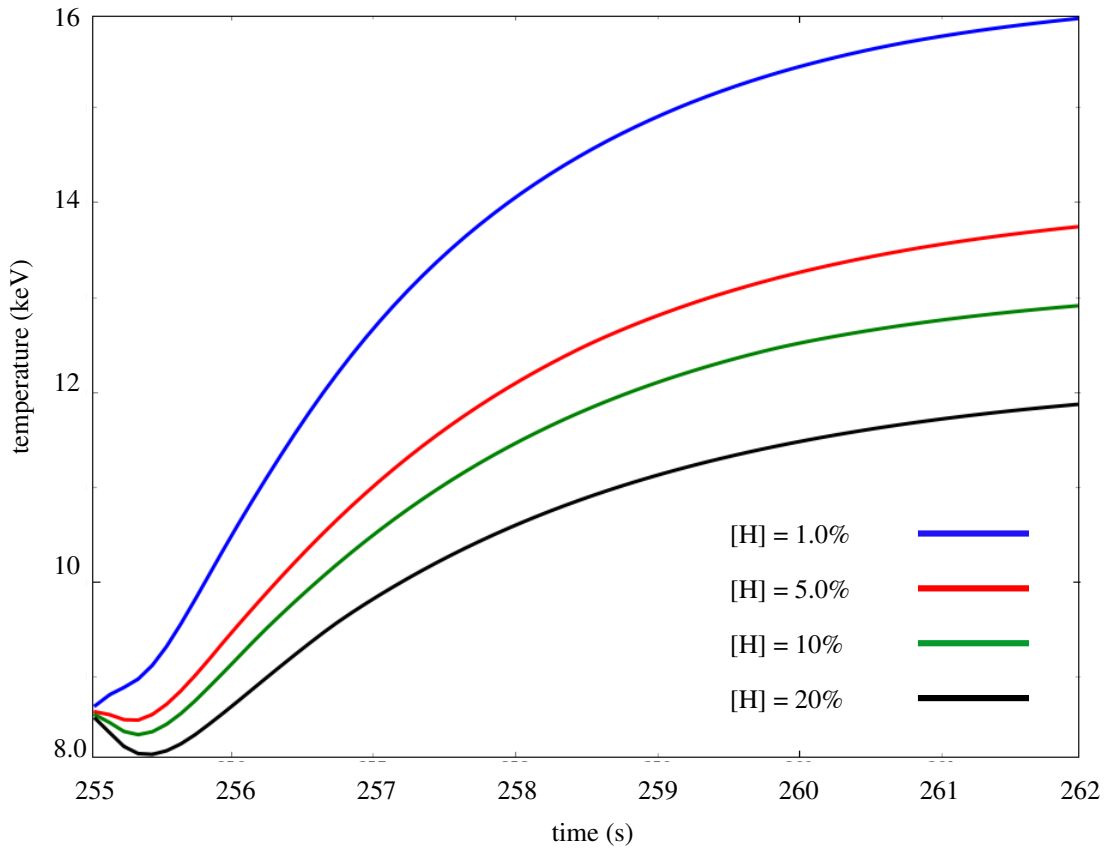

Fig. 4.10 *Time evolution of the electron temperature at the normalized flux surface* $s = 0.24$ *where the ICRF resonance is located, from* $t_i = 255$ *s to* $t_f = 262$ *s, for H concentrations of 1.0, 5.0, 10 and 20%.*

Figure 4.10 is shown at the IC resonance, where the main absorption mechanism is 2^{nd} H harmonic damping, whereas electron damping peaks off-axis. As the plasma starts to heat, direct electron damping increases and so do the electronic temperatures. This is not the case when the H concentration is at 1.0% because electron damping is very large and takes place on-axis.

4.2.4 Scenario 3: Fundamental ^{3}He Heating in a Three-Ion-Scheme in H Plasma at 3.3 T

For the study of fundamental ^{3}He ($\omega = \omega_{^3He}$) heating in a three-ion-scheme in ITER H plasma at 3.3T , synthetic *discharge* 104010 was used. The main ion composition in the

plasma was H:^{4}He with 85%:15% and a small ^{3}He concentration in the range of 0.01%-0.20%. In terms of H&CD, the plasma was heated using 30 MW of ECRH. This shot has one time slice, so the PION+ ETS simulation was started there during the flat-top phase, at t_i = 500 s, with the plasma and ICRF parameters as shown in Table 4.6. An ICRF frequency of 40 MHz was chosen to target the fundamental minority ^{3}He resonance, located off-axis at a normalized flux surface of $s = 0.62$. The ICRF power of 20 MW was chosen based on the ITER Research Plan. The settings for the evolution of the temperature and the density, as well as the transport model and the antenna spectrum, are as those used in Scenarios 1 and 2 studied above. The concentrations were chosen to allow comparison with the results in [7]. Finally, the duration of the simulation was chosen to be 5 s to provide sufficient time for the plasma to evolve towards a new steady state.

Table 4.6 *Plasma composition (with minority concentration in brackets), heating scheme, magnetic field (B_0), ICRF frequency (f), ICRF power (P_{ICRF}) and central electron and ion temperatures and densities, where n_i refers to the majority ion density at a ^{3}He concentration of 0.01%.*

Plasma	Heating Scheme	B_0 (T)	f (MHz)	P_{ICRF} (MW)	$n_e^0 x10^{19}$ (m^{-3})	$n_i^0 x10^{19}$ (m^{-3})	T_e^0	T_i^0
H-^{4}He-(^{3}He)	$\omega = \omega_{^3He}$	3.3	40	20	4.9	0.3	12	9.5

Figure 4.11 shows the temperature and density profiles for electrons and ions. The initial electron temperature is higher than the ion temperature at the beginning of the simulation (T_i^0 = 9.5 keV as compared to T_e^0 = 11.8 keV). The electron temperature profile evolves and there is a 40% increase in temperature after thermalization. The ion temperatures, however, show almost no change after plasma relaxation, no perceptible change in central temperature, although some difference between concentrations can be seen. Similarly to Scenario 2 studied above, the central temperature of the case with the smallest minority concentration is the highest. The larger differences in temperature due to the ^{3}He concentration are also seen here in the T_e profile, rather than in the T_i profile.

The competing absorption mechanisms as given by PION+ETS are fundamental ^{3}He damping and direct electron damping. Figure 4.12 shows that the fundamental ^{3}He absorption takes place much more off-axis than the power deposition in Scenario 1. The fundamental ^{3}He resonance is located in the HFS of the plasma. The electron damping takes place over the whole radia profile, but it is most intense on-axis, where the electron temperature and density are highest. In Table 4.7 it can be seen that most of the power is absorbed by the ^{3}He resonance for the ^{3}He concentrations above 0.05%, whereas below this concentration the dominating mechanism is direct electron damping. This can also be understood in terms of

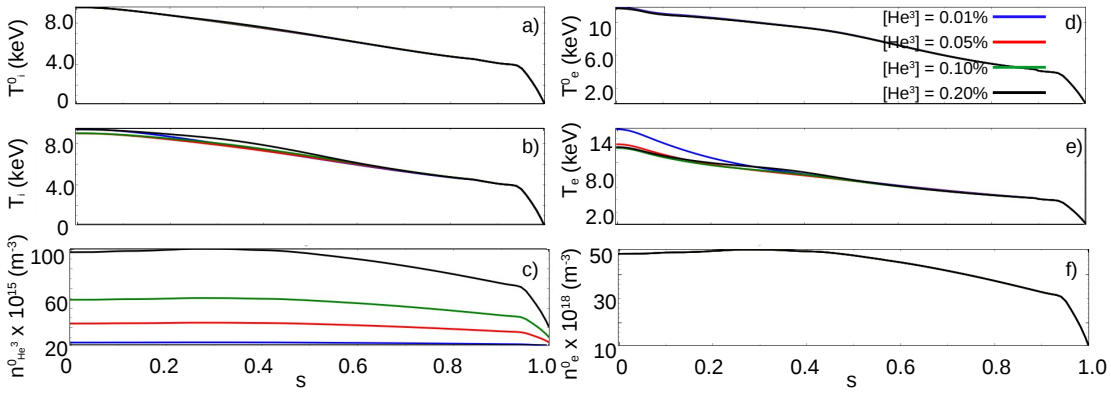

Fig. 4.11 *Overview of ITER discharge 104010 for* ^{3}*He concentrations of [*^{3}*He]= 0.01, 0.05, 0.10 and 0.20%. a) Temperature of the ions at the start of the simulation* (T_i^0)*, b) temperature of the ions at the end of the simulation* (T_i)*, c) density of the* ^{3}*He ions at the start of the simulation* ($n^0_{^3He}$)*, d) temperature of the electrons at the start of the simulation* (T_e^0)*, e) temperature of the electrons at the end of the simulation* (T_e) *density of the electrons at the start of the simulation* n_e^0.

the SPA, which is very low (7%) for the ^{3}He concentration of 0.01%, resulting in most of the power in the ICRF wave not being absorbed at the resonance and arriving at the centre of the plasma, where it is absorbed by the electrons. Based on the values in Table 4.7, it is evident that there is a trend of higher power absorption by the fundamental ^{3}He damping as the ^{3}He concentration increases, peaking at 65% when the minority concentration reaches 0.20%. The SPA is also highest (89%) at this concentration. It is worth noting that, as the concentration increases, the peak in the absorption profile becomes narrower and moves closer to the centre of the plasma and away from the resonance. This could be explained in terms of the energy density. As the ^{3}He concentration is increased, the power per particle and hence the energy of the fast ions increases. Therefore, the orbits of the fast ions and the location of the wave-particle interaction change with the ^{3}He concentration via Doppler broadening of the resonance. This could also be related to the fact that, when the ^{3}He density is modified, the density of ^{4}He also varies in order to maintain quasineutrality. As it was explained in Subsection 2.1.7, the location of the *L*-cutoff depends on the density ratio between the main two ion species in the plasma. This change in the density ratio between species can change the location of ω_{cutoff} in equation 2.18 and therefore modify the location of the absorption.

In terms of the collisional power transfer shown in Figure 4.13, there is dominant electron heating for the lowest and highest ^{3}He concentrations of 0.01% and 0.20%, and dominant bulk ion heating for 0.05% and 0.10%. The average energy of the fast ^{3}He ions in the tail of

Table 4.7 *^{3}He concentrations, power absorbed by resonant ^{3}He ions and electrons ($P_{abs,^3He}$, $P_{abs,e}$), fractions of collisional power transferred from resonant ions to bulk ions (P_{ci}/P_c) and background electrons (P_{ce}/P_c), critical energy (E_{crit}) and average energy of the fast ^{3}He ions ($\langle E_{fast,H}\rangle$) as given by PION+ETS for Scenario 3 with different ^{3}He concentrations.*

^{3}He (%)	$P_{abs,^3He}$ (MW)	$P_{abs,e}$ (MW)	P_{ci}/P_c (%)	P_{ce}/P_c (%)	E_{crit} (keV)	$\langle E_{fast,H}\rangle$ (keV)
0.01	4.26	14.0	17.1	82.9	601	775
0.05	8.56	9.39	51.9	48.1	510	169
0.10	10.5	7.18	55.7	44.3	486	71.9
0.20	11.3	6.08	43.8	56.2	496	102

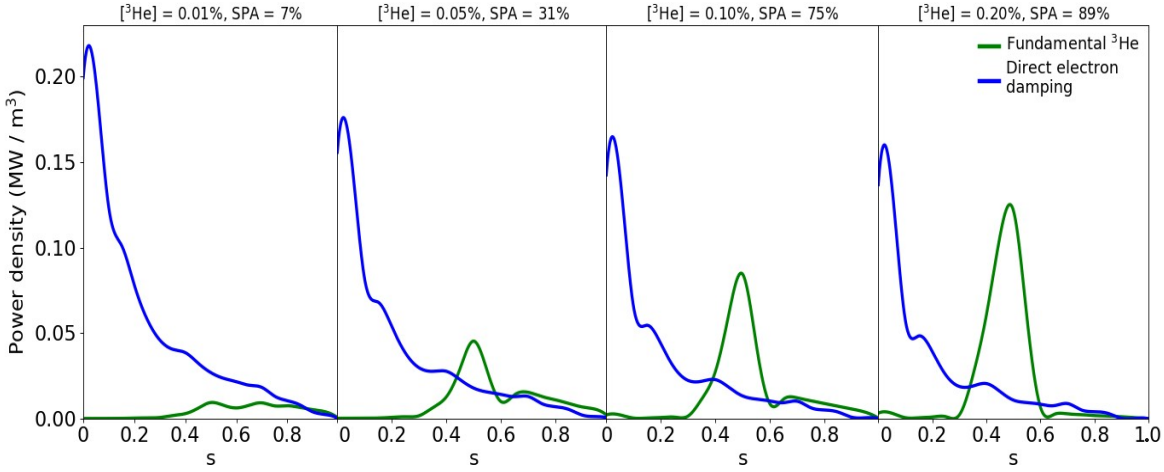

Fig. 4.12 *RF-power density absorbed by the fundamental ^{3}He (green) and direct electron damping (blue) as a function of the normalized flux surface, s, at the end of the simulation at $t_f = 505$ s, for [^{3}He]=0.01, 0.05, 0.10 and 0.20%. SPA coefficients on ^{3}He at the resonance and toroidal mode number N=54 are given in the legends.*

the fast ion distribution function is higher in the case of the lowest concentration, but lower in every other case (in the range of 775 - 71.9 keV c.f. Table 4.7) than their critical energy (601 - 486 keV). Therefore, the ^{3}He ions will collide mainly with the bulk ions and transfer their energy to them. The case with the highest concentration does not seem to follow the trend seen in Scenarios 1 and 2, where $\langle E_{fast}\rangle$ decreases with the increasing concentration. The reason for this might be that the $\langle E_{fast,^3He}\rangle$ values shown in Table 4.7 are given at the ICRF resonance, whereas the collisional power transfer is an integrated value over all flux surfaces. If we consider the values of P_{ci} and P_{ce} at the resonance $s = 0.62$ in Figure 4.13, it can be seen that, apart from the lowest minority concentration case, the P_{ce} and P_{ci} profiles seem to meet close to the resonance, resulting in a relatively equivalent power equipartition.

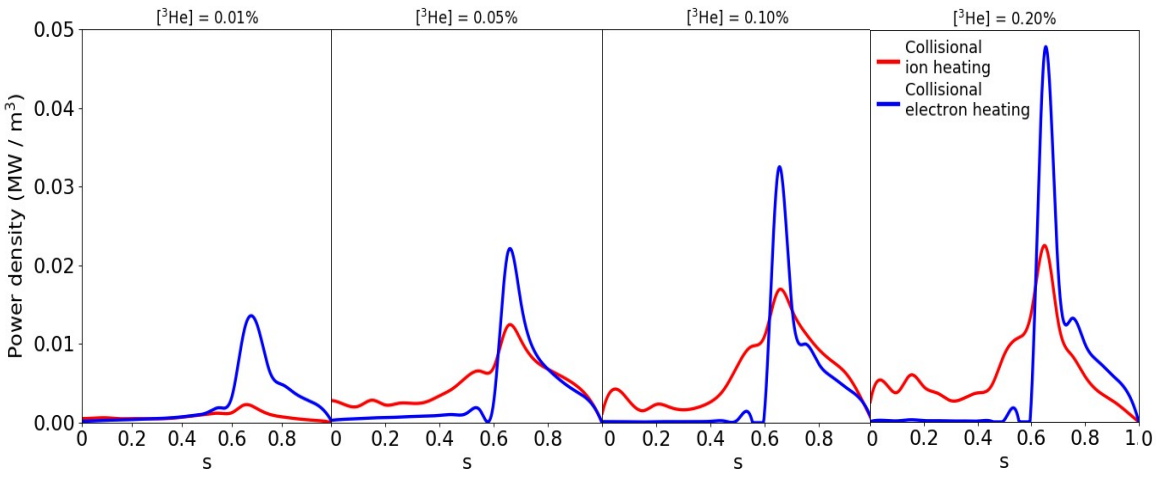

Fig. 4.13 *Orbit redistributed collisional power transfer from the resonant ion species to bulk ions (red) and electrons (blue) at* $t_f = 505$ *s, for [*^{3}*He]=0.01, 0.05, 0.10 and 0.20%.*

The distinct peaks in the profile of the orbit redistributed collisional power transfer to ions and electrons might be due to FOW effects.

In order to confirm that these peaks were indeed the result of FOW effects, a test was performed. FOW effects are larger when the resonant energy particle energy is large. Reducing the energy per particle can help to alleviate these effects. In order to understand the effect of this energy reduction on the peaks present in Figure 4.13, a set of simulations was conducted. In these simulations, the minority concentrations were kept constant at a ^{3}He concentration of 0.05%, whilst the input ICRF power was modified to P_{ICRF} = 20, 10, 5.0 and 1.0 MW. By reducing the input power whilst keeping a constant concentration, the power per particle is effectively reduced. The results are shown in Figure 4.14, where the contribution from the collisional power transfer to electrons and electron damping have been added, and all values are scaled per MW of input power. The peaks in Figure 4.13 are no longer seen, although some undulations in the P_{ci} profile are still visible at around $s = 0.3$ for an input ICRF power of 1.0 MW. Otherwise, the $P_{ce} + P_{abs,e}$ profile is relatively smooth and follows closely the shape of the power density absorbed by electrons profile. The shape of the P_{ci} profile does not change in any relevant way, apart from increasing in size, which is expected when modifying the input power for a fixed minority concentration and scaling per input MW. Another expected effect is the increase in the power equipartition going to bulk ion heating as the input ICRF power is lowered. As the power is decreased, the energy of the fast ions in the tail of the energy distribution function decreases as well, leading to majority collisions with the bulk ions rather than the background electrons.

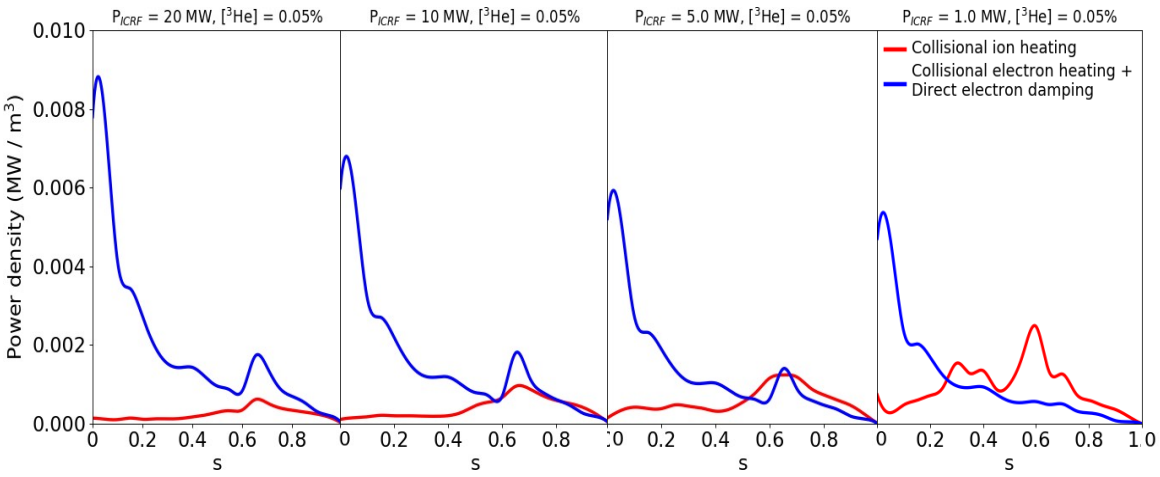

Fig. 4.14 *Orbit redistributed collisional power transfer from the resonant ion species to bulk ions (red) and background electrons (blue) at $t_f = 505$ s, at [^{3}He]=0.05 and for P_{ICRF} = 20, 10, 5.0 and 1.0 MW. The contributions from P_{ce} and $P_{abs,e}$ have been added, and all contributions are scaled by MW of input power.*

Absorption at the H and ^{4}He ion cyclotron resonance layers

PION is built for modelling the distribution function of one or two fast ion species, although it can only simulate species with the same resonance position. If there is more than one resonance, PION considers the resonances and models the one closest to the plasma centre, which in this case is the fundamental ^{3}He resonance. The resonance can however be forced. The chosen ICRF frequency coincides with the fundamental H resonance and the 2nd ^{4}He harmonic resonance. By forcing the fundamental H resonance and renormalizing the absorptions we obtain Figure 4.15. Direct electron damping has been left out purposely to allow closer consideration of the power absorption equipartition between the competing mechanisms, i.e, fundamental H damping, 2nd ^{4}He harmonic damping and fundamental ^{3}He damping.

Figure 4.15 shows off-axis absorptions for all competing mechanisms. There are parasitic, LFS, off-axis absorptions by the fundamental H damping and 2nd ^{4}He harmonic dampings, located at $s = 0.81$. It should be noted that the ^{4}He profile is very narrow as compared to the other two. The H damping profile, on the other hand, is quite broad. As it was explained in Subsection 2.2.1, the broadening of the power deposition profile is governed by the parallel velocity distribution function. PION computes the parallel velocity $v_{||}$ through the fast ion distribution function and the effective pitch angle. The Doppler broadening increases with the increasing $v_{||}$. The $v_{||}$ of the ^{4}He ions in the fast ion distribution function is therefore quite low compared to that of the H ions. 2nd ^{4}He harmonic and fundamental ^{3}He damping increase

with the increasing ^{3}He concentration, whereas fundamental H damping decreases and becomes competitive with the fundamental ^{3}He absorption at a ^{3}He concentration of 0.01% (c.f. Table 4.8). Direct electron damping is the dominant mechanism of absorption for all ^{3}He concentrations considered, followed by fundamental ^{3}He damping for the concentrations below 0.10%, and by 2nd ^{4}He harmonic damping for the concentrations above.

Table 4.8 *^{3}He concentrations, power absorbed by resonant ^{3}He, ^{4}He and H ions, and electrons ($P_{abs,^3He}$, $P_{abs,^4He}$, $P_{abs,H}$, $P_{abs,e}$), fractions of power transferred from resonant ions to bulk ions (P_{ci}/P_c) and background electrons (P_{ce}/P_c) as given by PION+ETS for Scenario 3 with different ^{3}He concentrations. All values are given after renormalization.*

^{3}He (%)	$P_{abs,^3He}$ (MW)	$P_{abs,^4He}$ (MW)	$P_{abs,H}$ (MW)	$P_{abs,e}$ (MW)	P_{ci}/P_c (%)	P_{ce}/P_c (%)
0.01	2.22	0.66	2.05	15.1	80.8	19.2
0.05	4.50	3.22	1.75	10.5	77.9	22.1
0.10	5.52	5.60	1.41	7.47	74.3	25.7
0.20	5.99	6.10	1.36	6.55	73.0	27.0

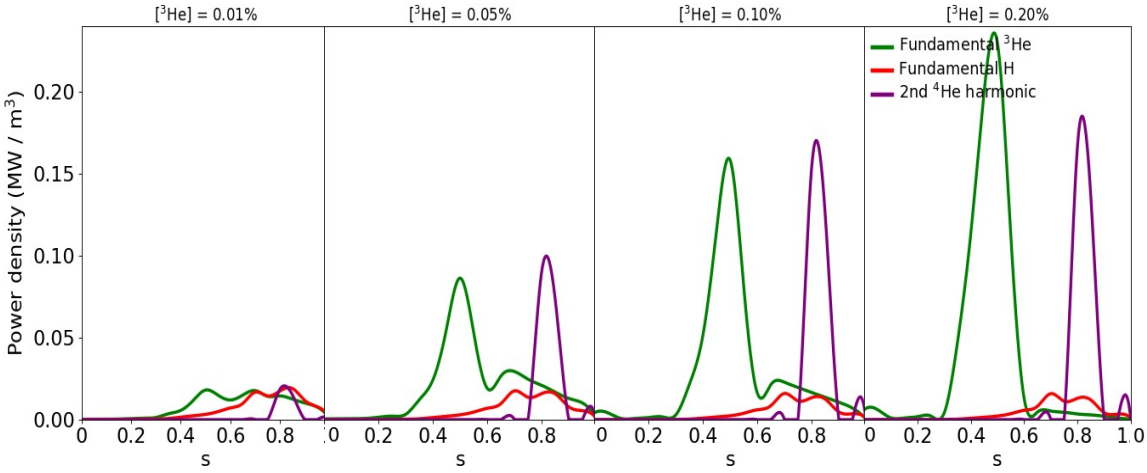

Fig. 4.15 *RF-power density absorbed by fundamental ^{3}He ions (green), 2nd ^{4}He harmonic (purple) and fundamental H (red), as a function of the normalized flux surface, s, at the end of the simulation at $t_f = 505$ s, for [^{3}He]=0.01, 0.05, 0.10 and 0.20%.*

Figure 4.16 shows the collisional power transfer after including the H and ^{4}He resonances. It can be seen that all profiles have changed considerably as compared to Figure 4.13. The P_{ce} profile is broader and flatter than in Figure 4.13, and the P_{ci} profile is narrower, centred between $s = 0.4$ and $s = 1.0$, with a peak divided in two, probably due to a combination of the influences of $P_{abs,^3He}$ and $P_{abs,^4He}$. From Table 4.8 we can see that there is dominant bulk ion heating for all concentrations considered, with a maximum at a ^{3}He concentration of 0.01%.

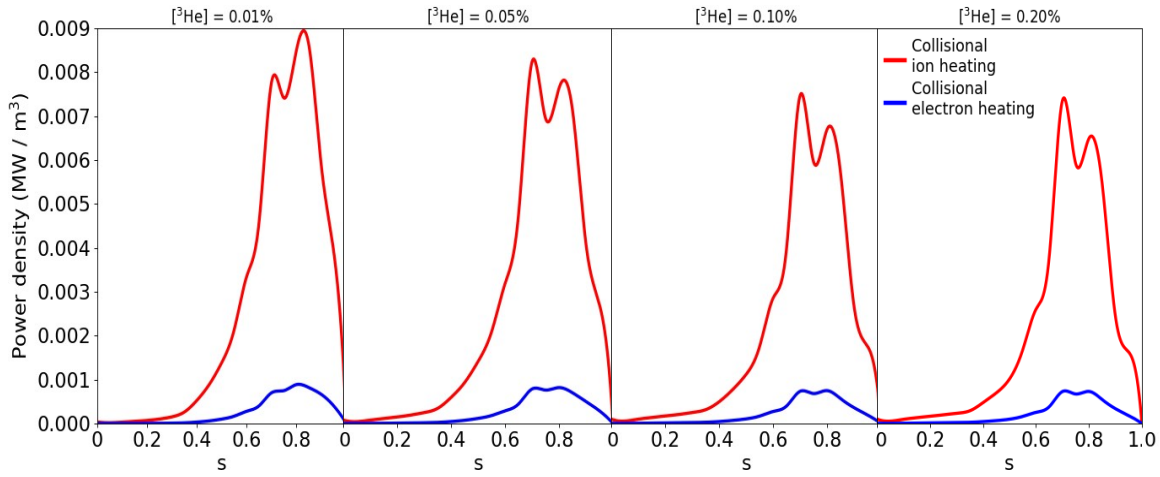

Fig. 4.16 *Orbit redistributed collisional power transfer from the resonant ion species to bulk ions (red) and electrons (blue), taking into account absorption at the H and ^{4}He resonance layers and renormalization, at $t_f = 505$ s, for [^{3}He]=0.01, 0.05, 0.10 and 0.20%.*

It should be noted that P_{ci}/P_c decreases with the increasing minority concentration. This might be due to the fact that the fundamental H and ^{3}He damping at the lower concentrations are larger than the 2nd ^{4}He harmonic damping. As these absorptions take place at the fundamental resonance, the tail in the velocity distribution function is not as high-energy, the resonant ions have a lower energy density and will therefore collide mainly with the bulk ions. As the concentration increases, 2nd ^{4}He harmonic damping becomes more dominant as compared to fundamental H damping. As the 2nd ^{4}He harmonic damping takes place at the harmonics, a high-energy tail containing trapped ions with very high perpendicular velocities will be formed. These fast ions will hence collide mainly with the background electrons, causing the electron heating to increase.

Figure 4.17 shows the time evolution of the thermal ion temperature at different ^{3}He concentrations. In this scenario, the temperatures range from 5.78 keV to 5.92 keV at $t_f = 505$ s, with the lowest T_i = 5.78 keV at a ^{3}He concentration of 0.01% and the highest T_i = 5.92 keV at a ^{3}He concentration of 0.20%. As shown in Figure 4.15, the ion temperature increases as the ^{3}He concentration increases in the range 0.01 to 0.20%. It should be noted that the transient evolution in the first seconds of the simulation is quite similar to the evolution in Scenario 1, and also depends on the parameters used in the transport model. The highest ^{3}He concentration yields the largest ICRF absorption, SPA and, consequently, highest final ion temperature. It is also worth noting that the profiles for all concentrations have a lower temperature at the end of the simulation than at the beginning. This can be expected since the plasma was initially heated by a higher ECRH power than the ICRF power that was then

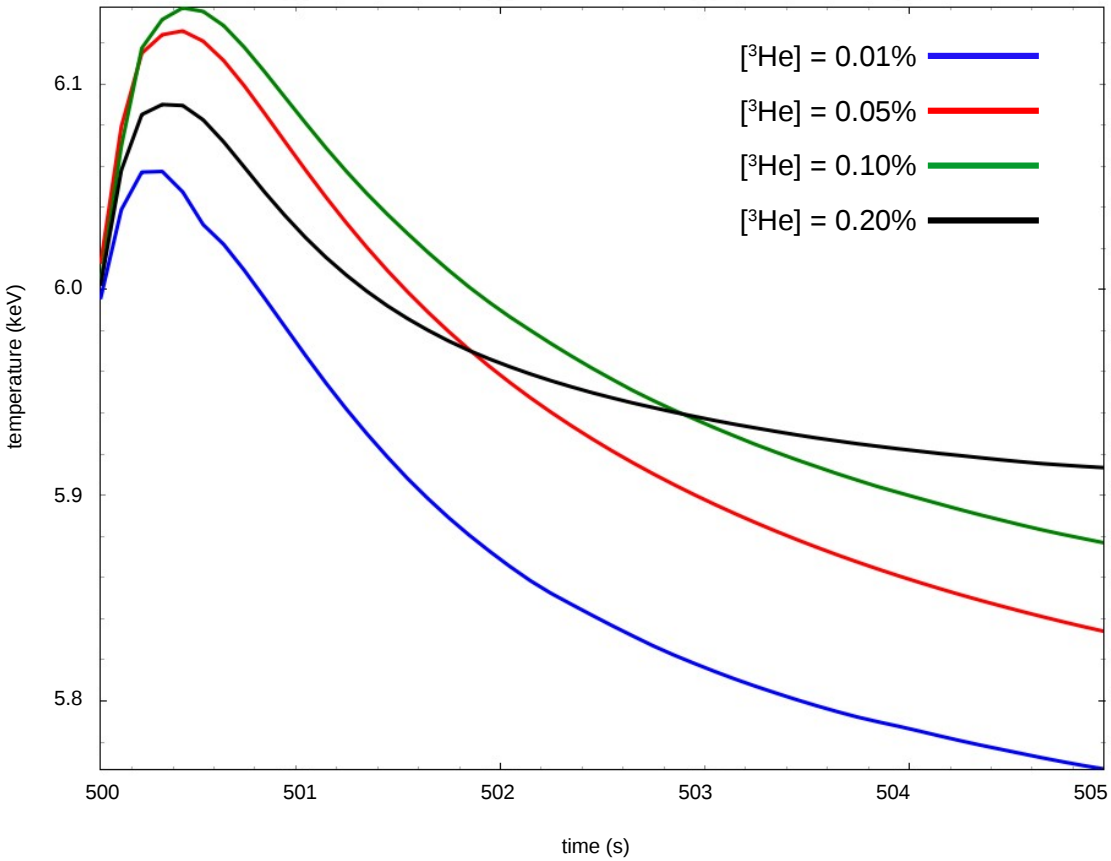

Fig. 4.17 *Time evolution of the thermal ion temperature at the location of the* ^{3}*He resonance at* $s = 0.62$ *from* $t_i = 500$ *s to* $t_f = 505$ *s for [*^{3}*He]=0.01, 0.05, 0.10 and 0.20%.*

applied during the simulation. As seen previously in the temperature profiles in Figure 4.11, even though a percentage of the ICRF power has been absorbed by the resonant ions, it has not been enough to increase the ionic temperature after relaxation. The ICRF power has, however, increased the electronic temperature, as shown in Figure 4.18.

Figure 4.18 shows the time evolution of the electron temperature at the location of the peak in electron damping at $s = 0.0$. The temperatures at the end of the simulation at $t_f = 262$ s are in the range of 12.4 - 15.4 keV, with the lowest T_e = 12.4 keV at a ^{3}He concentration of 0.20% and the highest T_e = 15.4 keV at a ^{3}He concentration of 0.01%. The case with a ^{3}He concentration of 0.01% has the largest electron damping, as well as the most dominant background electron heating, with 86% of the collisional power being transferred to electrons, resulting in the highest electron temperature. As shown in Figure 4.18, the electron temperature increases as the ^{3}He concentration decreases, apart from the case with the highest ^{3}He concentration. Even though electron damping is larger in the case with a ^{3}He

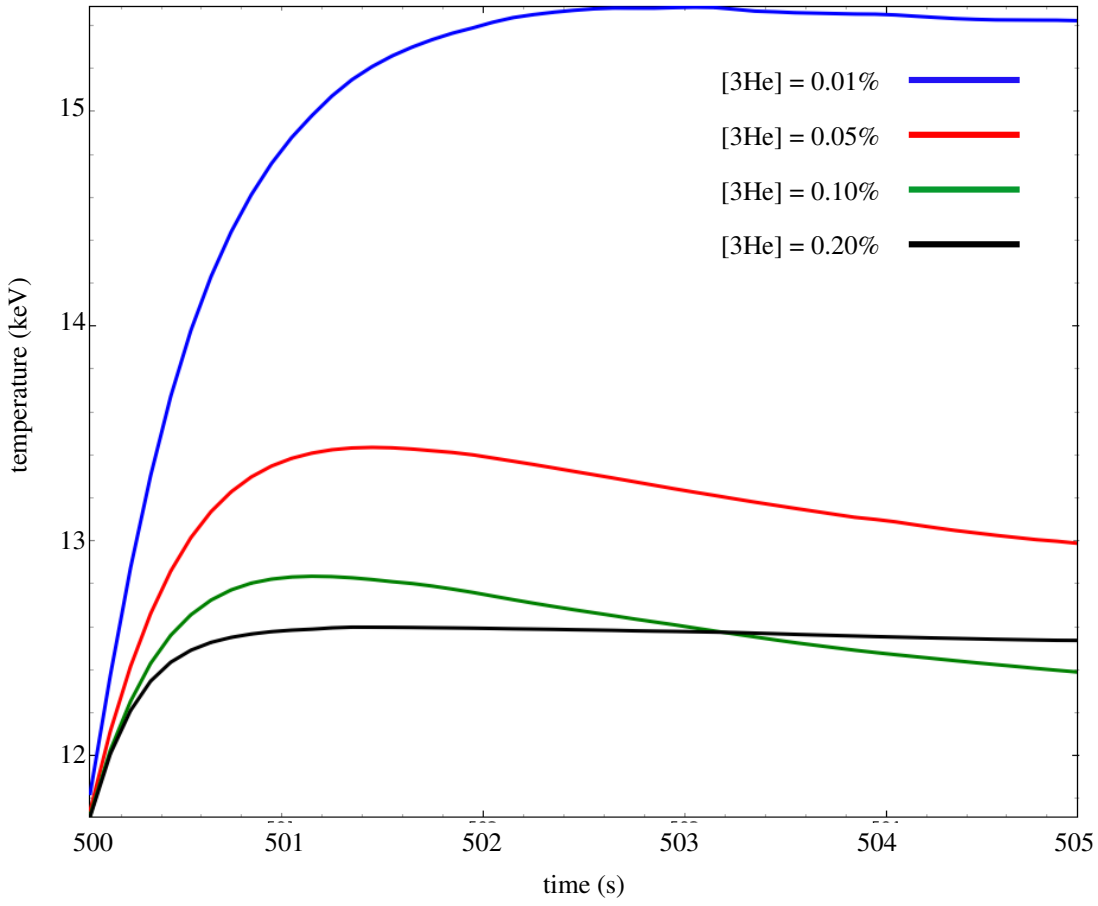

Fig. 4.18 *Time evolution of the electron temperature at the centre of the plasma at* $s = 0.0$ *from* $t_i = 500$ *s to* $t_f = 505$ *s for [*^{3}*He]=0.01, 0.05, 0.10 and 0.20%.*

concentration of 0.10%, the electron temperature at the end of the simulation is higher for the case with a ^{3}He concentration of 0.20%. This might be explained in terms of the collisional power. The collisional power transfer to electrons is larger for the highest ^{3}He concentration, resulting in a slightly higher temperature.

4.3 ICRH+NBI Synergy at JET

In this section, one ICRF minority heating scenario is investigated in a JET plasma and the results are presented; fundamental H ($\omega = \omega_H$) minority heating in a synthetic D baseline [104] plasma at 2.8 T. The work is divided into three cases: in Case 1 ICRF is used as the only

source, in Case 2 NBI is used as an only source, and in Case 3 the effects of the ICRH+NBI synergy are studied.

In Subsection 3.1.2 it was mentioned that when ICRF heating is used in combination with NBI, certain synergistic effects can take place. This synergy arises when the particles in the NBI beam resonate with the ICRF wave. This resonance enables the ICRF wave to effectively interact with both the plasma population that it is targeting and with the beam population, leading to a possible enhancement in ICRF performance and plasma heating. In this section we use three H&CD codes integrated into the ETS workflow: the ICRF code PION, the NBI heating code BBNBI [105] and the Fokker-Planck solver NBISIM2 (an implementation of the formulas found in [26]), to study and predict how the ICRH+NBI synergy will affect the plasma performance.

The main plasma parameters, the absorption and collisional transfer profiles and the evolution of the thermal ionic temperature are analysed for each case. The source evolution and the penetration of the NBI beams are also studied.

4.3.1 Fundamental H Minority Heating in D Plasma at 2.8 T

For the study of fundamental H ($\omega = \omega_H$) minority heating in JET D plasma, synthetic plasma based on JET *discharge* 92436 was used. The synthetic plasma was heated using 23.6 MW of NBI, 2 MW of ECRH and 5 MW of ICRF whereas the experimental *discharge* 92436 had only NBI and ICRF heating. In IMAS this shot has one time slice available during the flat-top phase at t_i = 9 s, with the plasma ICRF and NBI parameters as shown in Table 4.9. An ICRF frequency of 48 MHz was chosen, placing the fundamental H resonance close to the plasma centre. The ICRF power of 5 MW and the NBI power of 23.6 MW were chosen based on the H&CD capabilities available at JET for this particular discharge. In the simulation set-up, the temperature evolution of the ions was set to be predictive, whilst the density evolution and the temperature evolution of the electrons was set to be interpretative for simplicity, given the focus of the present study on bulk ion heating. The transport model and antenna spectrum are as used in the ITER scenarios, although the toroidal mode number considered when giving the SPA coefficients in this case is $N = 26$. Finally, the duration of the simulation was chosen to be 5 s to allow time for the plasma to evolve towards a new steady state.

Figure 4.19 shows the temperature and density profiles for electrons and ions for Case 1 as an example (refer to figure 4.30 regarding the differences in ion temperatures between different cases). The differences with the profiles from Cases 2 and 3 are negligible, so these

Table 4.9 *Plasma composition (with the minority species in brackets), heating scheme, magnetic field (B_0), ICRF frequency (f), ICRF power (P_{ICRF}), NBI power (P_{NBI}) and central electron and ion temperatures and densities, where n_i refers to the majority ion density at a H concentration of 1.0%.*

Plasma	Heating Scheme	B_0 (T)	f (MHz)	P_{ICRF} (MW)	P_{NBI} (MW)	$n_e^0 x10^{19}$ (m^{-3})	$n_i^0 x10^{19}$ (m^{-3})	T_e^0	T_i^0
D-(H)	$\omega = \omega_H$	2.8	48	5.0	23.6	7.8	7.8	6.8	6.0

profiles can be used as an overview for all three sets of simulations. The electron temperature profiles show a discontinuity at $s = 0.9$ caused by the transport model. In this case there is no difference between the electron temperature profiles at the start and end of the simulation because the temperature evolution of the electrons was set to be interpretative, as opposed to predictive. The initial electron and H temperatures are almost identical, apart from a small divergence of the smaller minority concentrations. This divergence grows by the end of the simulation, when the difference between the largest minority concentration and the rest is of the order of $\sim$ 2 keV. This results in a decrease in temperature of $\sim$ 15% for the H concentrations between 1.0 - 5.0%. There is no perceptible change in temperature for the case with a H concentration of 10% at the centre of the plasma, although slight variations are visible with increasing s.

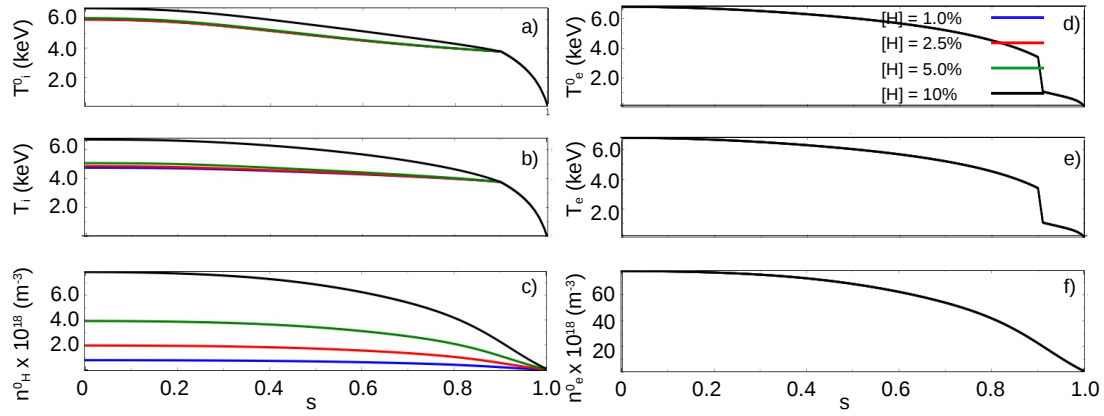

Fig. 4.19 *Overview of JET discharge 92436 for H concentrations of [H]= 1.0, 2.5, 5.0 and 10%. a) Temperature of the ions at the start of the simulation (T_i^0), b) temperature of the ions at the end of the simulation (T_i), c) density of the H ions at the start of the simulation (n_H^0), d) temperature of the electrons at the start of the simulation (T_e^0), e) temperature of the electrons at the end of the simulation (T_e) density of the electrons at the start of the simulation n_e^0.*

Case 1: ICRF as the Only Source

Figure 4.20 shows the power density absorption profile as given by PION+ETS at $t_f = 14$ s. There are three competing absorption mechanisms, i.e., fundamental H damping, 2nd D harmonic damping and direct electron damping. Fundamental H resonance is the dominating mechanism of wave absorption for all concentrations considered. The fundamental H absorption takes place in the HFS of the plasma, the highest peak in the profile on-axis for the H concentrations below 5.0%, and off-axis for the concentrations above. The resonance located at $s = 0.36$. As we can see from Figure 4.20, the SPA on H, which is taken at the resonance and toroidal mode number N=26, increases with the H concentration reaching a maximum of 83% at a H concentration of 5.0%. The SPA at the minimum H concentration of 1.0% is sufficiently low (40%) to facilitate significant D damping (12% of the ICRF power, see Table 4.10). D absorption primarily occurs off-axis due to the selected ICRF frequency aligning with the 2nd D harmonic resonance. Consequently, as fundamental H minority damping decreases with decreasing H concentration, 2nd D harmonic majority damping begins to rival dominant H damping. Here, the electron damping takes place on-axis, where the electron temperature and density are highest. Although fundamental H damping is the principal absorption mechanism, direct electron damping absorbs more than 40% of the ICRF power independently of the H concentration, reaching its maximum absorption of 47% at a H concentration of 10%. Fundamental H damping absorbs more than half of the ICRF power for all concentrations above 1.0%, and reaches a maximum at a H concentration of 2.5%. The SPA, however, is highest (83%) for the larger concentration of 5.0%. Thus, in this case the highest SPA does not correspond to the most efficient concentration in terms of absorption. This might be caused by the fact that collisional ion heating is much higher for the case with 5.0% as compared to the case with 2.5%, resulting in a higher final thermal ion temperature. A higher ionic temperature can allow a higher SPA.

Table 4.10 *H concentrations, power absorbed by resonant H and D ions and electrons ($P_{abs,H}$, $P_{abs,e}$, $P_{abs,D}$), fractions of collisional power transferred from resonant ions to bulk ions (P_{ci}/P_c) and background electrons (P_{ce}/P_c), critical energy (E_{crit}) and average energy of the fast H ions ($\langle E_{fast,H} \rangle$) for Case 1 as given by PION+ETS for H minority heating in D plasma with different H concentrations.*

H (%)	$P_{abs,H}$ (MW)	$P_{abs,e}$ (MW)	$P_{abs,D}$ (MW)	P_{ci}/P_c (%)	P_{ce}/P_c (%)	E_{crit} (keV)	$\langle E_{fast,H} \rangle$ (keV)
1.0	2.36	2.15	0.60	41.9	52.1	63.8	228
2.5	2.85	2.05	0.20	49.7	50.3	64.5	163
5.0	2.76	2.13	0.19	78.0	22.0	65.5	54.5
10	2.57	2.35	0.10	91.3	8.70	67.6	23.1

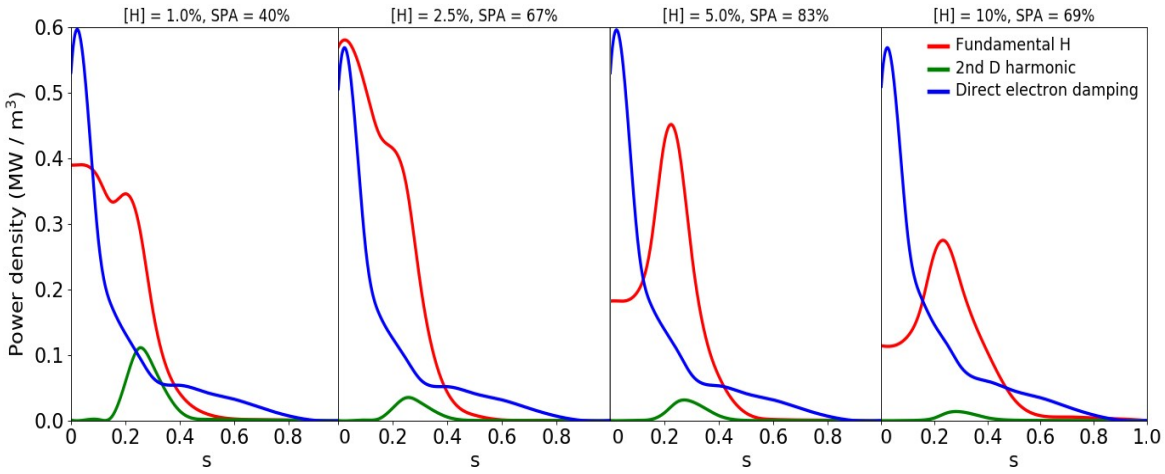

Fig. 4.20 *RF-power density absorbed by the fundamental H (red), 2nd D harmonic (green) and direct electron damping (blue) as a function of the normalized flux surface, s, at the end of the simulation at $t_f = 14$ s, for [H]= 1.0, 2.5, 5.0 and 10%. SPA coefficients on H at the resonance and toroidal mode number N=26 are given in the legends for Case 1.*

In terms of the collisional power transfer shown in Figure 4.21, there is dominant electron heating for the H concentrations below 5.0% and dominant bulk ion heating for the higher concentrations. The average energy of H ions in the tail of the fast ion distribution function falls below (ranging from 23.1 - 228 keV, see Table 4.10) their critical energy (63.8 - 67.6 keV) for lower H concentrations, leading to predominant bulk ion heating. For a H concentration of 2.5%, $\langle E_{fast,H} \rangle \sim 2E_{crit}$, resulting in an almost equivalent equipartition of collisional power $P_{ci}/P_c \sim 0.5$. As the H concentration is increased, the average energy of the fast H decreases, whilst the critical energy remains relatively constant, arriving at $\langle E_{fast,H} \rangle \sim 1/3E_{crit}$ at a H concentration of 10%, resulting in a high collisional bulk ion heating fraction of $P_{ci}/P_c \sim 0.9$. It is worth noting that the collisional power transfer profiles seem to be slightly shifted to the right and peak closer to the resonance than the absorbed power profiles for the lower concentrations. This type of shift might be caused by FOW effects, which tend to move the profiles to the right due to orbit redistribution, especially P_{ce}, since the most energetic ions mainly transfer their power to electrons.

Figure 4.22 shows the time evolution of the thermal ion temperature at the location of the ICRF resonance at the normalized flux surface $s = 0.36$. The temperatures at the end of the simulation at $t_f = 14$ s are in the range of 4.6 - 4.8 keV, with the lowest T_i = 4.6 keV at a H concentration of 1.0% and the highest T_i = 4.8 keV at a H concentration of 10%. The final temperature of all concentrations is lower than their initial temperature. This can be expected since the plasma was initially heated by a higher combined ICRF, ECRH and NBI

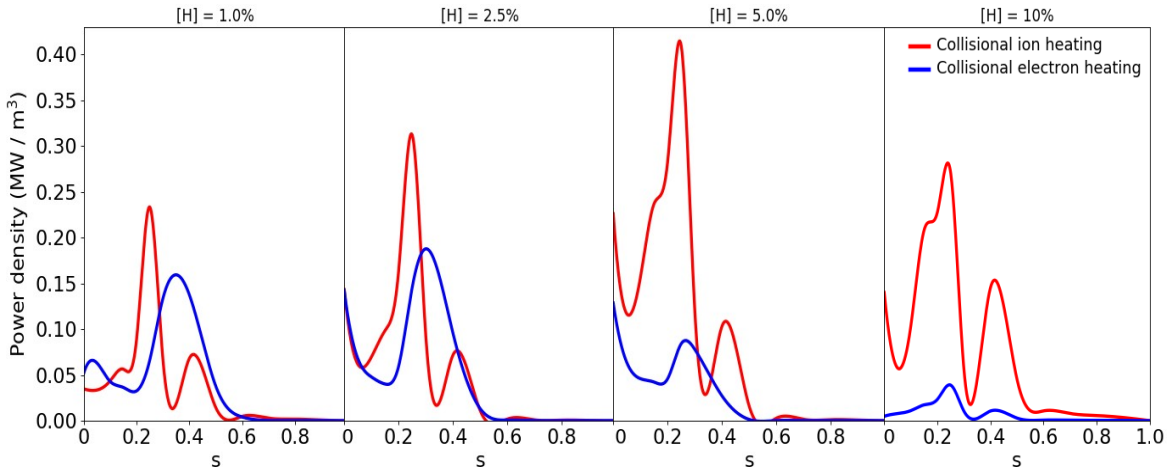

Fig. 4.21 *Orbit redistributed collisional power transfer from the resonant ion species to bulk ions (red) and electrons (blue) at* $t_f = 14$ *s, for [H]=1.0, 2.5, 5.0 and 10% for Case 1.*

heating power. This decrease is of the order of $\sim$ 15% for the lowest minority concentration and $\sim$ 10% for the highest. As shown in Figure 4.21, the ion temperature increases as the H concentration increases in the range 1.0% to 10 %. It is worth noting that even though the most efficient concentration in terms of power absorption is a H concentration of 2.5% (56%) and the best performance in terms of SPA is a H concentration of 5% (83%), these concentrations do not result in the highest temperature when the plasma reaches the steady state. This might be explained in terms of the collisional power transfer. The most dominant bulk ion heating takes place at a H concentration of 10%, with more than 90% of the absorbed power going to the thermal ion population, and resulting in the highest thermal ion temperature at the end of the simulation.

Case 2: NBI as the Only Source

In this set of simulations, NBI is used as the only source. The NBI heating code chosen as the ETS actor was BBNBI [105], whilst NBISIM2 (an implementation of the formulas found in [26]) was used as the Fokker-Planck solver. The plasma was heated with 23.6 MW of NBI power using D beams. There is no ICRF heating in this case and hence no ICRF power absorbed. Therefore, only the collisional power transfer relevant values are shown in Table 4.11. NBI heating should not depend on the H concentration, the values are included in Table 4.11 to show that this is indeed the case.

The primary goal of NBI is to introduce high-energy neutral particles into the plasma to transfer energy and momentum and increase the plasma temperature. When the NBI beams

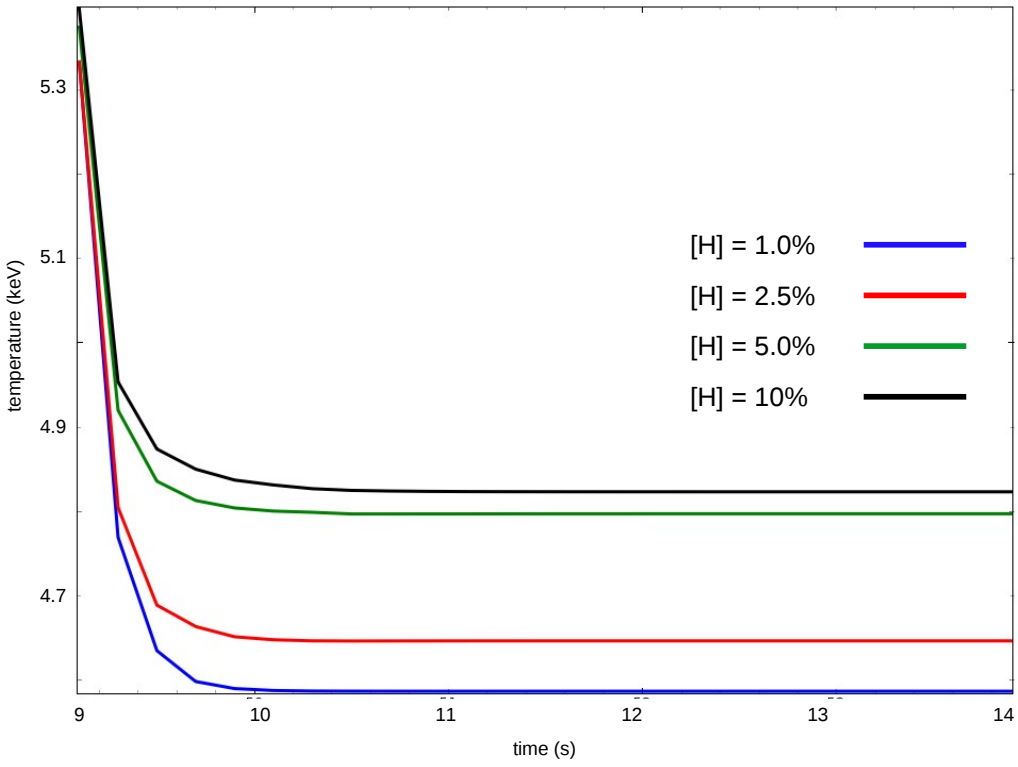

Fig. 4.22 *Time evolution of the thermal ion temperature at the location of the H resonance at* $s = 0.36$ *from* $t_i = 9$ *s to* $t_f = 14$ *s for [H]=1.0, 2.5, 5.0 and 10% for Case 1.*

Table 4.11 *H concentrations, total collisional power transferred from resonant ions to bulk ions (P_{ci}) and background electrons (P_{ce}), and fractions of said power (P_{ci}/P_c, P_{ce}/P_c) for Case 2 as given by PION+ETS for H minority heating in D plasma with different H concentrations.*

H (%)	P_{ci} (MW)	P_{ce} (MW)	P_{ci}/P_c (%)	P_{ce}/P_c (%)
1.0	19.9	3.99	83.3	16.7
2.5	20.1	3.94	83.6	16.4
5.0	20.0	3.95	83.5	16.5
10	19.9	3.83	83.9	16.1

are injected into the plasma, the particles can penetrate deeper than charged particles towards the centre of the tokamak without significant deflection by the magnetic fields, becoming ionized and colliding with the bulk ions and background electrons, transferring their energy and becoming part of the plasma [26]. Figure 4.23 shows the NBI penetration, given as the density of the D neutrals from the NBI beams as a function of the normalized flux surface. The molecules in the beam can have either one (D), two (D2) or three (D3) D nuclei. The D molecules each carry all of the NBI energy, whereas the D nuclei in the D2 molecule each carry a half of the energy, and the nuclei in the D3 molecule each carry a third of the energy. The solid line in the plot represents the total sum of these contributions. NBI is said to have *good* penetration when a majority of the D neutrals reach the centre of the tokamak. In this case, the penetration is not good, as the beam deposition is very broad and the maximum deposition seems to be around mid radius ($s = 0.5$).

The collisional power transfer is shown in Figure 4.24. The P_{ci} and P_{ce} profiles in this case depend on the plasma density and on the penetration of the NBI beams. Hence, the profiles are broader than in Case 1. There is dominant bulk ion heating for all concentrations considered, both the total NBI power going to the bulk ions and the power equipartition between bulk ions and background electrons are extremely similar for every H concentration, which is expected because, as mentioned above, NBI heating does not depend significantly on the minority concentration. The two main peaks in the P_{ci} profile are at similar locations to the peaks in the Case 1 P_{ci} profile in 4.21, at around $s = 0.2$ and $s = 0.4$, although this second, off-axis peak is more prominent in Case 2. Another main difference is that, in Case 1, P_{ci} approaches 0 between $s = 0.5$ and $s = 1.0$, whereas in Case 2 bulk ion heating remains prominent through the whole plasma and does not approach 0 until it reaches the edge of the plasma, following the NBI penetration profile in Figure 4.23. In this case, the ions in the D beams will collide with the bulk ion population over a larger volume of the plasma than in Case 1. This serves to explain the broad P_{ce} profile as well. The fast ions that collide with

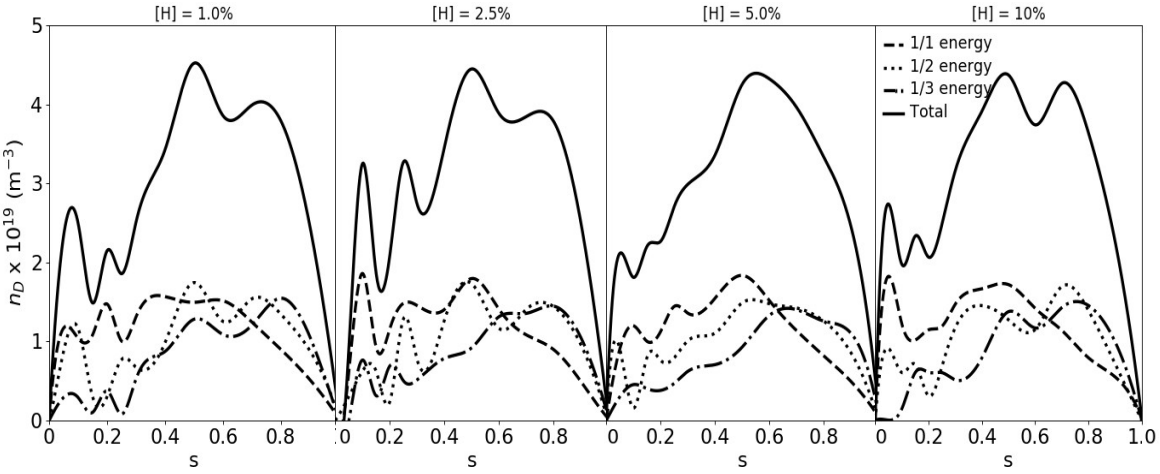

Fig. 4.23 *NBI penetration; the density of NBI D beam particles ($n_D x 10^{19} m^{-3}$) with respect to s is shown. The dashed, dotted and dash-dotted lines represent the fraction of particles with 1/1, 1/2 and a 1/3 of the energy (D, D2 and D3) respectively. The solid line represents the total sum. The profiles are shown at $t_f = 14$ s, for [H]=1.0, 2.5, 5.0 and 10% for Case 2.*

the background electrons are relatively evenly distributed through the plasma, so instead of following the direct electron damping as in Figure 4.20, the P_{ce} profile is also distributed between magnetic flux surfaces.

The presence of a peak in the P_{ci} profile at the location of the ICRF resonance in Figure 4.24 above is curious. Without any ICRF power present in these simulations, the collisional power transfer to ions should not depend on the location of the ICRF resonance. In order to assess whether this event was a reflection of some unknown physics or a numerical misbehaviour of the PION code, a comparison of the collisional power transfer to ions as calculated by the PION code and by the NBISIM2 Fokker-Planck solver was performed. This comparison is shown in Figure 4.25. It can be seen that the P_{ci} profiles given by NBISIM2 do not share the peaks at the ICRF resonance. They seem to follow quite closely the shape of the NBI penetration profiles, which is expected for a plasma where NBI is the only source. The collisional power transfer to ions as calculated by the PION code is thus affected by the presence of an ICRF resonance, even when the ICRF power is 0 MW. This is likely due to the simple orbit redistribution model used in PION which assumes that the fast ions are mainly trapped and have their turning points along the ICRF resonance layer. As we can see from Figure 4.25, this is not a good approximation for NBI heating only.

Figure 4.26 shows the time evolution of the thermal H temperature with NBI as the only source at the ICRF resonance $s = 0.36$. The temperatures at the end of the simulation at $t_f = 14$ s are in the range of 6.28 - 6.36 keV, with the lowest T_i = 6.28 keV at a H

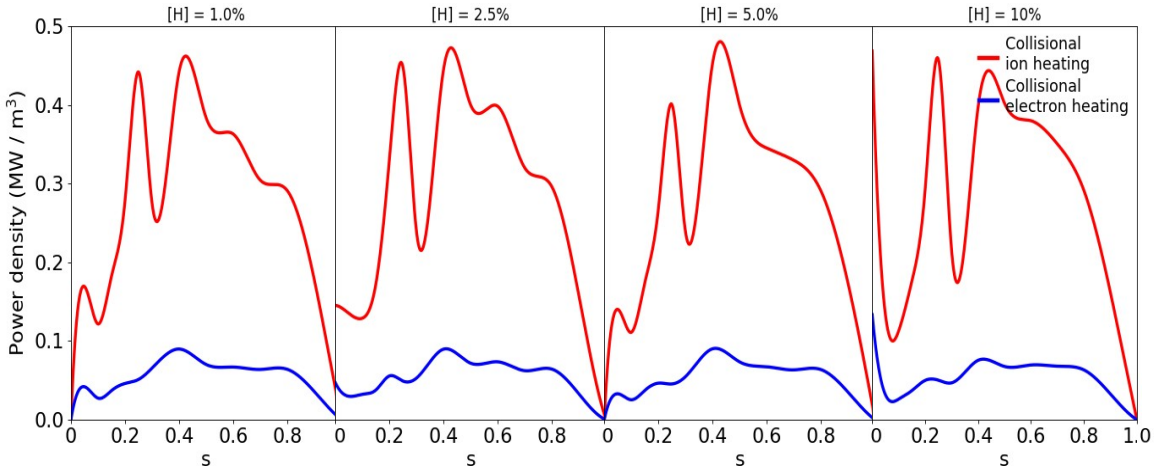

Fig. 4.24 *Orbit redistributed collisional power transfer from the NBI D beams to bulk ions (red) and electrons (blue) at* $t_f = 14$ *s, for [H]=1.0, 2.5, 5.0 and 10% for Case 2.*

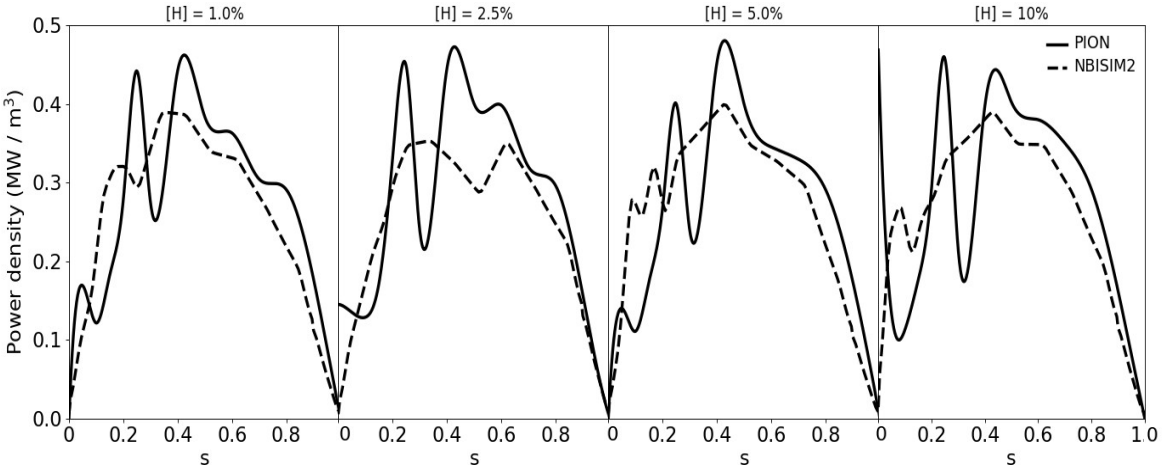

Fig. 4.25 *Comparison of the orbit redistributed collisional power transfer from the NBI D beams to bulk ions between the PION code (solid) and the NBISIM2 Fokker-Planck solver (dashed), at* $t_f = 14$ *s, for [H]=1.0, 2.5, 5.0 and 10% for Case 2.*

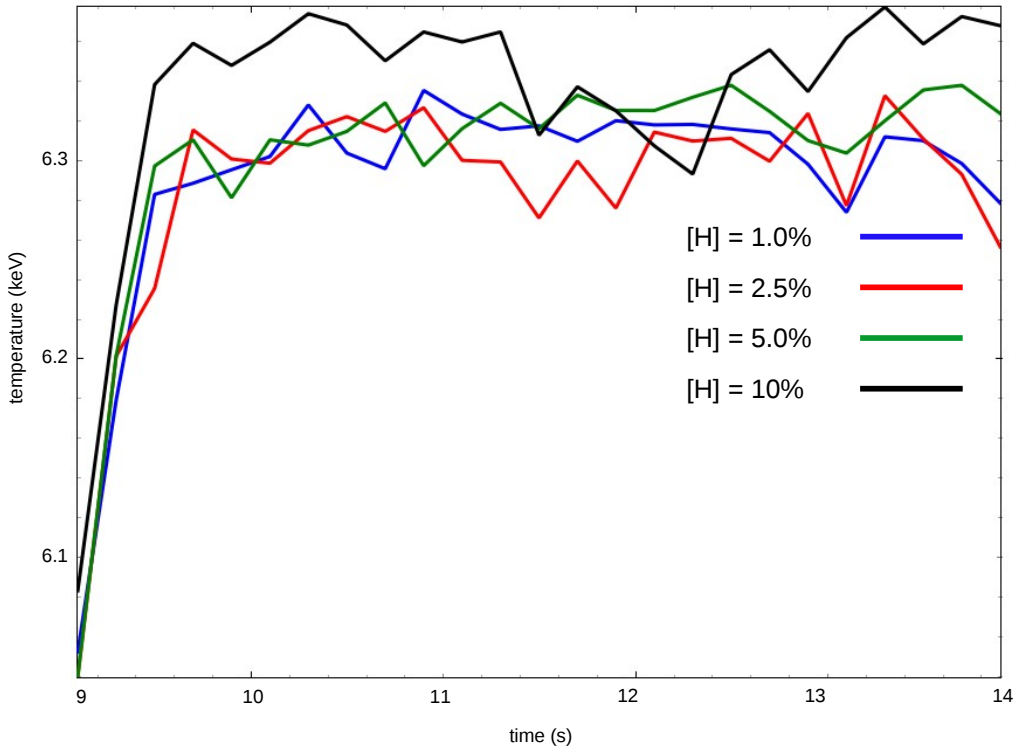

Fig. 4.26 *Time evolution of the thermal ion temperature at the location of the H resonance at* $s = 0.36$ *from* $t_i = 9$ *s to* $t_f = 14$ *s for [H]=1.0, 2.5, 5.0 and 10% for Case 2.*

concentration of 2.5% and the highest T_i = 6.36 keV at a H concentration of 10%. All final ionic temperatures are higher than the initial temperatures for all concentrations considered, with an increase of $\sim 4\%$ for a H concentration of 2.5% and an an increase of $\sim 5\%$ for a H concentration of 10%.

It is worth noting that the temperature evolution of this scenario seems to be less linear than the evolution of Case 1 in Figure 4.22. This might be explained in terms of the evolution in time of the power emitted by each source shown in Figure 4.27. In Case 1, the ICRF source emits power at a constant value from $t_i = 9$ s to $t_f = 14$ s. In Case 2, there are larger fluctuations in the power evolution, with gradients as large as 0.5 MW per time step, which could serve to explain the fluctuations observed in the thermal H temperature evolution for Case 2.

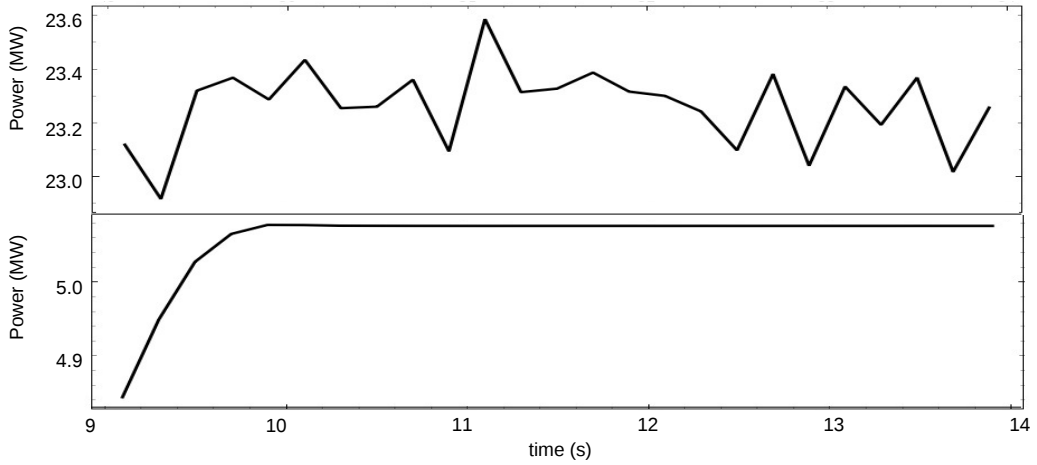

Fig. 4.27 *Time evolution of the power emitted by NBI (top) and ICRF (bottom), from* $t_i = 9$ *s to* $t_f = 14$ *s.*

Case 3: ICRH+NBI Synergy

In this subsection we used NBI combined with ICRF heating to study the effect of the synergy on the evolution of the plasma parameters. The ICRF power and frequency are as those used in Case 1, targeting the fundamental H resonance, which coincides with the 2nd harmonic resonance of the D ions in the plasma and the beam population. The NBI power and beams are as used in Case 2. The settings for the evolution of the temperature and the density, as well as the transport model, are also as those used in Cases 1 and 2.

Table 4.12 *H concentrations, power absorbed by resonant H and D ions and electrons (*$P_{abs,H}$*,* $P_{abs,e}$*,* $P_{abs,D}$*), total collisional power transferred from resonant ions to bulk ions (*P_{ci}*) and background electrons (*P_{ce}*), and fractions of said power (*P_{ci}/P_c*,* P_{ce}/P_c*) for Case 3 as given by PION+ETS for H minority heating in D plasma with different H concentrations.*

H (%)	$P_{abs,H}$ (MW)	$P_{abs,e}$ (MW)	$P_{abs,D}$ (MW)	P_{ci} (MW)	P_{ce} (MW)	P_{ci}/P_c (%)	P_{ce}/P_c (%)
1.0	2.23	1.98	0.85	21.4	5.74	78.8	21.2
2.5	2.75	1.91	0.36	21.3	5.52	79.4	20.6
5.0	2.69	2.01	0.38	22.0	4.75	82.3	17.7
10	2.70	2.13	0.21	22.5	4.24	84.1	15.9

Figure 4.28 shows the power density absorption profile of Case 3 (dashed lines) as given by PION+ETS at $t_f = 14$ s, compared to the Case 1 power absorption profiles from Figure 4.20 (solid lines). Case 2 is not displayed because there was no ICRF power absorption. Since the power absorption related values in Table 4.12 and Figure 4.28 depend on the ICRF wave absorption, no significant difference should be seen as compared to Case 1. Fundamental

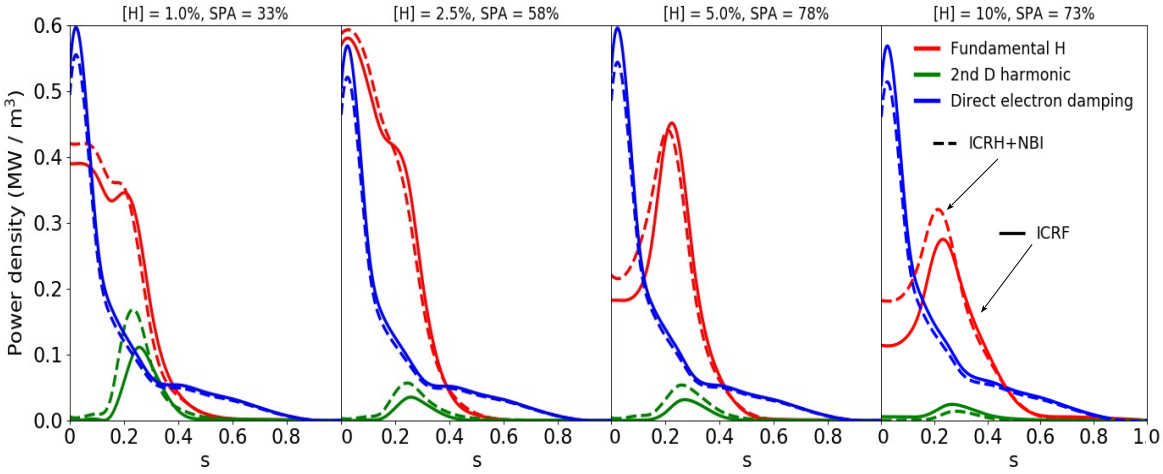

Fig. 4.28 *RF-power density absorbed by fundamental H (red), 2nd D harmonic (green) and direct electron damping (blue) as a function of the normalized flux surface, s, at the end of the simulation at $t_f = 14$ s, for [H]= 1.0, 2.5, 5.0 and 10%. The solid lines stand for ICRF only heating in Case 1, the dashed lines for ICRH+NBI heating in Case 3. SPA coefficients on H at the resonance and toroidal mode number N=26 are given in the legends for Case 3.*

H resonance is still the dominating mechanism of wave absorption for all concentrations considered. The main differences with the power density absorption profiles in Case 1 considered above are in the 2nd D harmonic damping and the SPA. The 2nd D harmonic damping has doubled for all concentrations considered with respect to Figure 4.20, reaching a maximum absorption at a H concentration of 1.0% (16%). This is due to the dependence of the ICRF power partitioning between H and D on the energy density of D [106]. By adding the NBI D beams, the energy density of D increases and thus the D damping. The SPA has decreased for all concentrations considered, with a minimum of 33% compared to the previous minimum of 40%, and a maximum of 78% compared to 83%.

The collisional power transfer in Figure 4.29 shows more relevant differences with Cases 1 and 2 considered above than the RF power density absorbed in Figure 4.28. The ions absorb the ICRF power through a particle-wave resonance and the NBI power through particle collisions. Later, the power absorbed from both sources is transferred to the thermal populations in the plasma through thermal relaxation. Figure 4.29 and the collisional transfer related values in Table 4.12 show the effect of the ICRH+NBI synergy on the plasma heating. The solid lines stand for ICRF only heating in Case 1, the dotted lines for NBI only heating in Case 2 and the dashed lines for the ICRH+NBI synergy in Case 3. There is dominant bulk ion heating for all H concentrations considered. The large majority of the NBI power has been collisionally transferred to the bulk ions (c.f. Table 4.12). The power transferred to the ions increases with the increasing H concentration, reaching a maximum of 22.5 MW at a

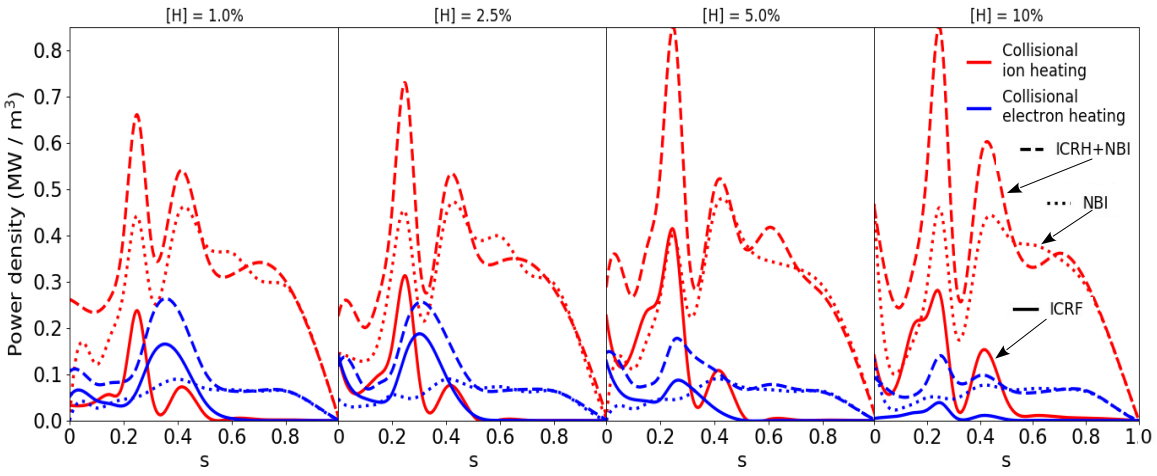

Fig. 4.29 *Orbit redistributed collisional power transfer from the resonant ion species to bulk ions (red) and electrons (blue) at $t_f = 14$ s, for [H]=1.0, 2.5, 5.0 and 10% for Case 3. The solid lines stand for ICRF only heating, the dotted lines for NBI only heating and the dashed lines for ICRH+NBI heating*

H concentration of 10%. The Case 3 profiles shown in Figure 4.29 follow a combination of the profiles seen in Figures 4.20 and 4.22 from Cases 1 and 2 for both the collisional power transferred to ions and electrons. In the P_{ci} profile from Case 3 there is a first peak corresponding to the ICRF resonance, more prominent in the Case 1 P_{ci} profile. The second peak is more off-axis, at around $s = 0.4$. This second peak and the broad slope between $s = 0.5$ and $s = 1.0$ follow very closely the collisional profile from Case 2. The difference between Cases 1 and 3 is larger in the case of the ions, where the ICRH+NBI Case 3 peak in the profile lies at almost 0.5 MW/m^3 higher than Case 1. The difference is not so notable with respect to Case 2, as the large majority of the contributions to the bulk ion heating are a consequence of the NBI heating.

Figure 4.30 shows the time evolution of the thermal H ions temperature at the location of the ICRF resonance at the normalized flux surface $s = 0.36$. Again, solid lines represent ICRF, dotted lines NBI and dashed lines ICRH+NBI as sources in Cases 1, 2 and 3, respectively. The Case 3 final temperatures are higher than in the other two cases, as was expected, for all concentrations considered. The temperatures at the end of the Case 3 simulation at $t_f = 14$ s are in the range of 6.5 - 6.8 keV, with the lowest T_i = 6.5 keV with a H concentration of 1.0% and the highest T_i = 6.8 keV with a H concentration of 10%. All final temperatures are higher than the initial temperatures for all concentrations considered, with an increase of $\sim$ 13% for a H concentration of 1.0% and an an increase of $\sim$ 8% for a H concentration of 10%. This represents a difference of $\sim$ 2 keV with Case 1 for the highest and lowest T_i, and of $\sim$

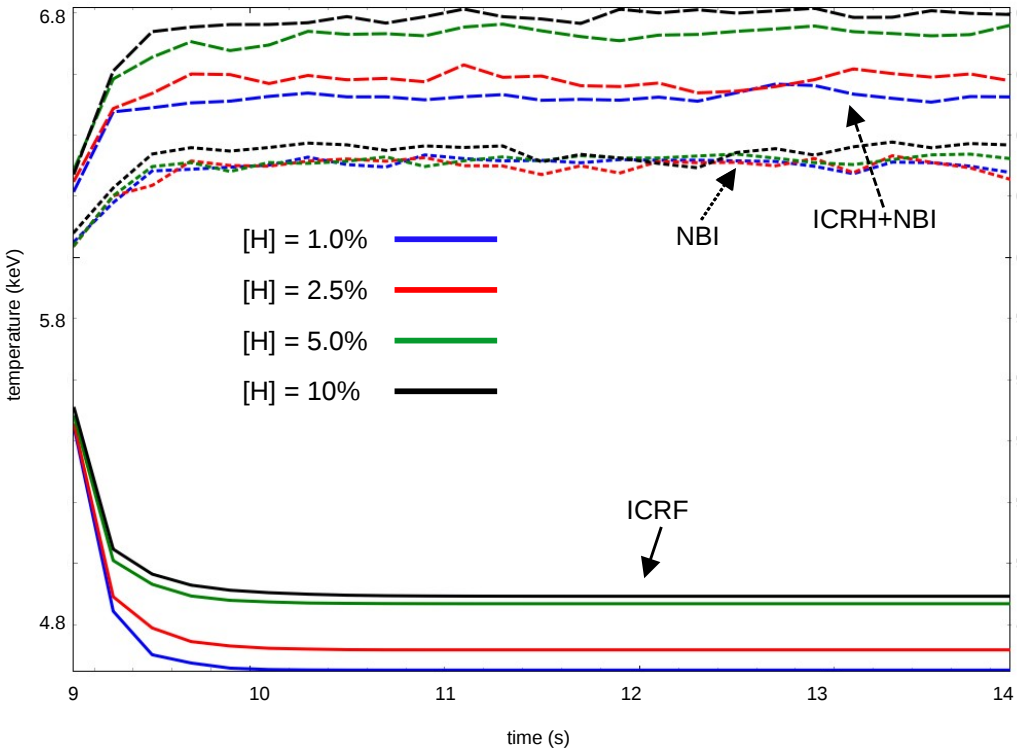

Fig. 4.30 *Time evolution of the thermal H ions temperature at the location of the ICRF resonance at* $s = 0.36$ *from* $t_i = 9$ *s to* $t_f = 14$ *s for [H]=1.0, 2.5, 5.0 and 10%. Solid lines for ICRF, dotted lines for NBI and dashed lines for ICRH+NBI.*

0.3 keV with Case 2. The Case 3 temperature profiles are smoother than the Case 2 profiles, but less linear than for Case 1. It is also worth noting that the ICRH+NBI in Case 3 shows the largest difference between the highest and lowest T_i, of the order of ~ 0.3 keV.

4.4 Minority Heating at AUG

In this section, fundamental H ($\omega = \omega_H$) minority heating in a D plasma at 2.5 T in AUG is investigated and the results are presented. This discharge was chosen because it was the only AUG shot available in IMAS. PION results for the power density absorbed and the collisional power transfer, as well as PION+ETS results for the evolution of the thermal ion temperature and the temperature and density profiles for the AUG *discharge* are displayed below.

4.4.1 Fundamental H Minority Heating in D Plasma at 2.5 T

For the study of fundamental H ($\omega = \omega_H$) minority heating in AUG D plasma, synthetic AUG *discharge* 30503 was used. The plasma was heated using 14.3 MW of NBI, 0.7 MW of Ohmic heating and 3 MW of ICRF. This shot has 6 time slices, so the PION+ ETS simulation was started at the last time slice, during the flat-top phase, at t_i = 2.58 s, with the plasma ICRF parameters as shown in Table 4.13. An ICRF frequency of 36.5 MHz was chosen to place the fundamental H resonance in the plasma centre. The ICRF power of 3.2 MW was chosen based on the H&CD capabilities available at AUG. In the simulation configuration, the temperature evolution of ions and electrons was designed to be predictive, while the density evolution of ions and electrons was set to be interpretive, for simplicity. This decision aligns with the emphasis of the present study on bulk ion heating. The transport model and antenna spectrum is as used in the ITER scenarios, although the toroidal number considered when giving the SPA coefficients is N = 12. Finally, the duration of the simulation was chosen to be 0.2 s, which, due to the smaller size of the AUG reactor, is enough time for the plasma to evolve towards a new steady state.

Table 4.13 *Plasma composition (with the minority species in brackets), heating scheme, magnetic field (B_0), ICRF frequency (f), ICRF power (P_{ICRF}) and central electron and ion temperatures and densities, where n_i refers to the majority ion density at a H concentration of 1.0%.*

Plasma	Heating Scheme	B_0 (T)	f (MHz)	P_{ICRF} (MW)	$n_e^0 x10^{19}$ (m^{-3})	$n_i^0 x10^{19}$ (m^{-3})	T_e^0	T_i^0
D-(H)	$\omega = \omega_H$	2.5	36.5	3.2	11	11	4.1	2.9

Figure 4.31 shows the temperature and density profiles for electrons and ions. The temperature profiles decrease with a steeper slope than the rest of the scenarios studied above. The initial electron temperature is slightly higher than the ion temperature at the beginning of the simulation (T_i^0 = 2.9 keV as compared to T_e^0 = 4.1 keV). There is no difference between H concentrations in the initial H temperature profile, whereas a small difference can be seen in the electron temperature profile at the centre of the reactor. The differences between concentrations are larger in the final temperature profiles, more so in the T_e^0 profile from $s = 0.0$ to $s = 0.2$. The central temperature of the case with 5.0% minority concentration is the highest in the T_i profile, whereas the largest minority concentration (10%) shows the highest final temperature in the case of the electrons. The electron temperature profile evolves and there is a $\sim 25\%$ increase in temperature after thermalization in the case with a H concentration of 10%. However, for a H concentration of 1.0%, there is an equal, but

opposite change, with a $\sim 25\%$ decrease. The final ion temperatures are lower than the initial temperatures independently of the concentration, with an average of a $\sim 60\%$ decrease.

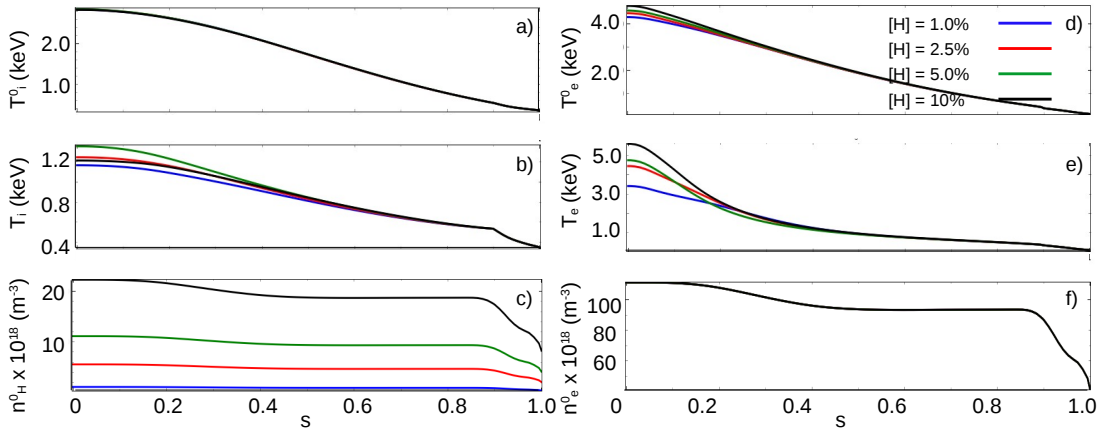

Fig. 4.31 *Overview of AUG discharge 30503 for H concentrations of [H]= 1.0, 2.5, 5.0 and 10%. a) Temperature of the ions at the start of the simulation (T_i^0), b) temperature of the ions at the end of the simulation (T_i), c) density of the H ions at the start of the simulation (n_H^0), d) temperature of the electrons at the start of the simulation (T_e^0), e) temperature of the electrons at the end of the simulation (T_e) density of the electrons at the start of the simulation n_e^0.*

Figure 4.32 shows the power density absorption profile as given by PION+ETS at $t_f = 2.78$ s. The three competing absorption mechanisms in this scenario are fundamental H damping, 2$^{\text{nd}}$ D harmonic damping and direct electron damping. Fundamental H resonance is the dominating mechanism of wave absorption for all concentrations considered. The fundamental H absorption takes place in the LFS of the plasma, the highest peak in the profile on-axis, very close to the centre of the plasma, with the resonance located at $s = 0.01$. There is a second, lower peak, more prominent for the H concentrations below 5.0%, off-axis and closer to $s = 0.3$. As we can see from Figure 4.32, the SPA increases with the H concentration reaching a maximum of 95% at a H concentration of 10%. For the 1.0% lowest H concentration, there is notable damping of the 2$^{\text{nd}}$ D harmonic (25% of the ICRF power, as shown in Table 4.14) attributed to the low H SPA (68%). Off-axis D absorption occurs because the selected ICRF frequency coincides with the 2$^{\text{nd}}$ D harmonic resonance. Consequently, as the fundamental H damping diminishes with decreasing H concentration, absorption of the 2$^{\text{nd}}$ harmonic by majority D damping begins to rival the dominant fundamental H damping. Here, the direct electron damping is small for all concentrations considered and takes place on-axis. Fundamental H absorption also increases with the concentration, absorbing 70% of the ICRF power or above for all concentrations considered, and reaching a maximum of 88% at a H concentration of 10%.

Table 4.14 *H concentrations, power absorbed by resonant H and D ions and electrons ($P_{abs,H}$, $P_{abs,e}$, $P_{abs,D}$), fractions of collisional power transferred from resonant ions to bulk ions (P_{ci}/P_c) and background electrons (P_{ce}/P_c), critical energy (E_{crit}) and average energy of the fast H ions ($\langle E_{fast,^3He} \rangle$) as given by PION+ETS for H minority heating in D plasma with different H concentrations.*

H (%)	$P_{abs,H}$ (MW)	$P_{abs,e}$ (MW)	$P_{abs,D}$ (MW)	P_{ci}/P_c (%)	P_{ce}/P_c (%)	E_{crit} (keV)	$\langle E_{fast,^3He} \rangle$ (keV)
1.0	2.18	0.18	0.80	42.3	57.7	32	129
2.5	2.58	0.14	0.43	42.7	57.3	37	84
5.0	2.75	0.14	0.27	48.8	51.2	43	62
10	2.80	0.24	0.14	59.2	40.8	47	44

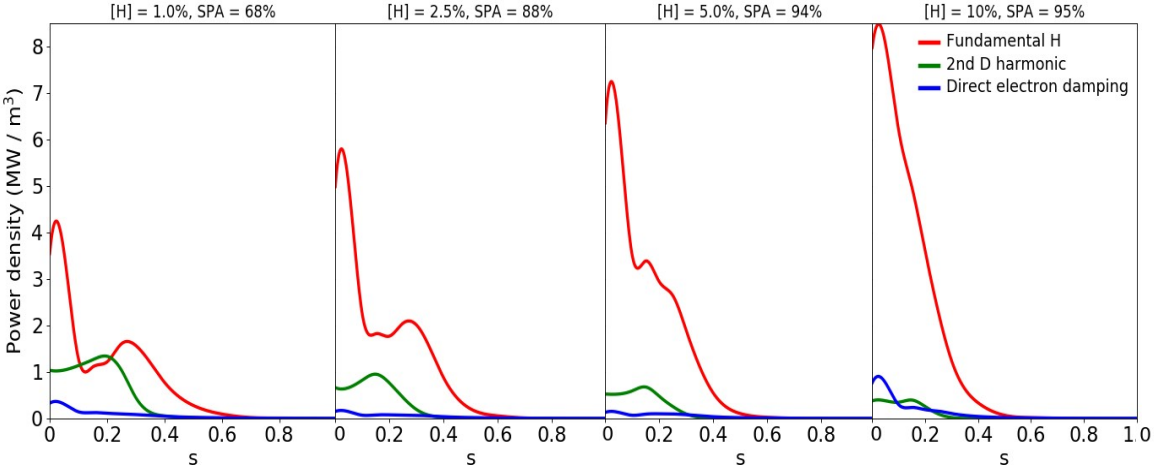

Fig. 4.32 *RF-power density absorbed by fundamental H (red), 2nd D harmonic and direct electron damping as a function of the normalized flux surface, s, at the end of the simulation at $t_f = 2.78$ s, for [H]=1.0, 2.5, 5.0 and 10%. SPA coefficients on H at the resonance and toroidal mode number N=12 are given in the legends.*

In terms of the collisional power transfer shown in Figure 4.33, there is dominant electron heating for all H concentrations considered apart from the H concentration at 10%. The average energy of H ions in the tail of the fast ion distribution function exceeds their critical energy (32 - 47 keV) for H concentrations below 10%, ranging from 44 - 129 keV (refer to Table 4.14). Consequently, these H ions primarily collide with the electron population, transferring their energy to them. As the H concentration is increased, the average energy of the fast H ions decreases, whilst the critical energy increases slightly, resulting in almost identical values for the H concentrations of 10% and $\langle E_{fast,H} \rangle \sim E_{crit}$, resulting in dominant bulk ion heating and $P_{ci}/P_c \sim 0.5$.

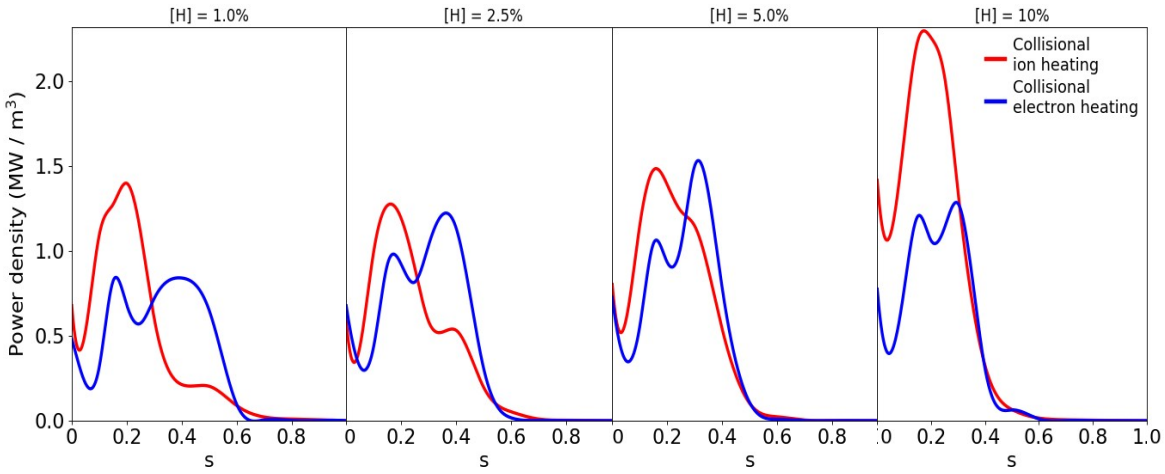

Fig. 4.33 *Orbit redistributed collisional power transfer from the resonant ion species to bulk ions (red) and electrons (blue) at t_f=2.78 s, for [H]=1.0, 2.5, 5.0 and 10%.*

Figure 4.34 shows the time evolution of the thermal ion temperature at the location of the ICRF resonance at the normalized flux surface $s = 0.01$. The temperatures at the end of the simulation at $t_f = 2.78$ s are in the range of 1.16 - 1.35 keV, with the lowest T_i = 1.16 keV with a H concentration of 1.0% and the highest T_i = 1.35 keV with a H concentration of 10%. As shown in Figure 4.34, the ion temperature increases as the H concentration increases in the range 1.0% to 10 %. There is a large difference between the final thermal ionic temperature corresponding to a H concentration of 10% and the rest of the concentrations considered. This happens because, apart from being the most efficient concentration in terms of power density absorbed and SPA, it is also the only concentration where bulk ion heating dominates over electron heating, resulting in a vast majority of the ICRF power going to the thermal ions.

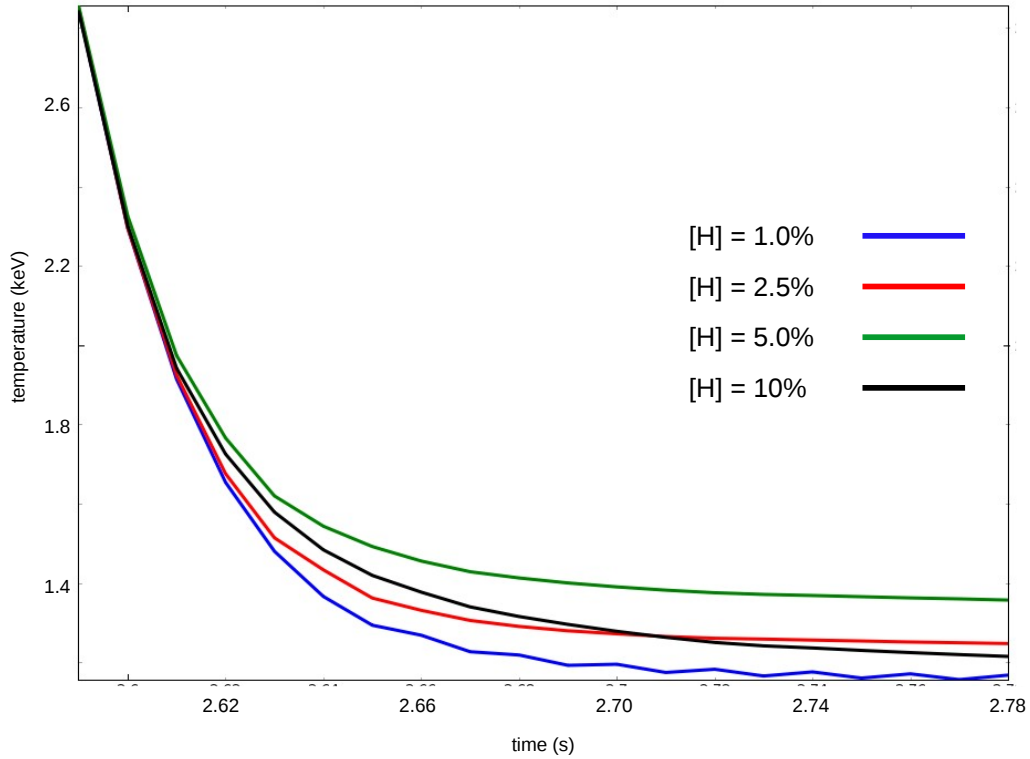

Fig. 4.34 *Time evolution of the thermal ion temperature at the location of the H resonance at* $s = 0.01$ *from* $t_i = 2.58$ *s to* $t_f = 2.78$ *s for [H]=1.0, 2.5, 5.0 and 10%.*

Chapter 5

Discussion, Conclusions and Future Steps

5.1 Discussion

5.1.1 Overview

In Chapter 4, three ITER scenarios of the non-active phase were investigated using time-dependent predictive PION+ETS simulations, taking self-consistently into account the power deposition, the modifications of the resonant ion distribution functions and resulting changes in the plasma parameters. Particular attention was given to the sensitivity of the ICRF power partition to minority concentration. The JET and AUG discharges will not be discussed further in the current chapter, as the focus of this thesis is on enhancing the performance of ICRF heating scenarios for the PFPO phase at ITER, and the modelling of these other tokamaks was carried out in order to prove the feasibility of using the PION+ETS integration on currently working reactors. The validation of this integration against experimental data from JET and AUG was, however, not in the scope of this thesis, and corresponds to the future steps. In this section, the power absorption, collisional power transfer and temperature enhancement in the ITER scenarios are reviewed and compared to the findings in [5–8] (referred to from here onwards as *previous works*). The ICRF heating code PION [1] integrated into the IMAS framework [84] (PION+IMAS), the 1D TOMCAT code [107], the TORIC 2D code [108] and the CYRANO/StixRedist 2D code [96, 97] have been used for the simulations in these previous works.

Unlike these previous works, which employed fixed plasma parameters in their simulations, the research in this thesis utilizes self-consistent simulations, where the temperature and density vary in response to the changes in the heating characteristics. For each scenario,

the central electron densities and the initial central temperatures of ions and electrons used in the simulations of these previous works are not exactly the same as the ones used in this thesis. These previous works also typically focus on a singular toroidal mode number. In contrast, the work in this thesis employs a more realistic, fuller antenna spectrum, represented by 100 toroidal mode numbers.

5.1.2 Scenario 1

Regarding power absorption, in Chapter 4, it was highlighted that fundamental H minority damping served as the primary absorption mechanism. A density scan indicated a rise in minority absorption from 1.0-5.0% of minority concentration, with no notable difference observed between 5.0% and 10%. Interestingly, the smallest H concentration facilitated central and competitive 2^{nd} ^{4}He harmonic absorption. However, as the minority concentration increased, this absorption decreased. The research in [5] with PION+IMAS revealed a similar trend. As the minority concentration increased, the power absorbed also escalated, peaking at 80% when the concentration was at 5%, very similar to the 78% calculated by PION+ETS. Furthermore, and again similarly to the results obtained with PION+ETS, FOW effects played a role in altering the radial profiles, resulting in widened and flattened distributions. The deposition profiles for fundamental H damping exhibited a distinct double peak at the center, whilst the direct electron damping was characterized by a broader and flatter profile. The simulations carried out by [6] using the 1D TOMCAT code provided power absorption percentages for fundamental H, 2^{nd} ^{4}He harmonic and direct electron damping at 72%, 6%, and 22%, respectively, for a H concentration of 5%. These were again very consistent with the results from PION+ETS, with percentages for fundamental H, 2^{nd} ^{4}He harmonic and direct electron damping at 78%, 2%, and 20%, respectively, although TOMCAT calculated a slightly higher absorption for 2^{nd} ^{4}He harmonic at the expense of fundamental H absorption. The ion absorption was notably central, whereas electron absorption tended to be flatter and more off-axis. In this aspect, PION+ETS, PION+IMAS, and TOMCAT coincided.

The SPA showed a similar pattern to the absorbed power in terms of its correlation with the minority concentration. In [7], they found a total SPA close to 100% for concentrations ranging from 2 - 8%. This suggested a significant absorption efficiency within this concentration range, although it should be noted that the SPA quoted there was the total SPA for ions and electrons combined, whereas the highest SPA found in this thesis, 99% for H concentrations of 5.0% and 10%, referred only to the power absorbed by H. In [6], for a H concentration of 5%, they found a SPA of 100%. An interesting finding in [6] was the decrease in H SPA and absorption with increasing minority concentration, decreasing from

$P_{abs,H}$ = 72% and a total SPA of 100% at an H concentration of 5% to $P_{abs,H}$ = 42% and a total SPA of 70% at an H concentration of 30%. This was attributed to the less favorable RF field polarization near the ion cyclotron resonance layer when the ^{4}He plasma was diluted, i.e., the screening effect. Conversely, there was an observed increase in electron absorption under similar conditions. A direct comparison with the results in this thesis could not be made because the largest minority concentration used was 10%, three times lower than the concentration used in [6].

Regarding collisional power transfer, PION+ETS calculated higher average fast energies for the resonant H ions than their critical energies, for all concentrations below 10%. This resulted in the majority of the ICRF power ending up in the electron channel and dominant electron heating. Notably, at an H concentration of 10%, there was a balanced power equipartition, resulting in 49% of the ICRF power being collisionally transferred to the bulk ions, and the rest being transferred to the electrons. In [5], they also found that the energy of the fast ions exceeded the critical energy threshold for all concentrations. This established a prevalent electron heating regime. As minority concentrations increased, there was a transition towards higher bulk ion heating. At a maximum minority concentration of 9% studied in [5], up to 38% of the collisional power went to bulk ion heating. PION+IMAS in [5] predicted a very similar P_{ci} profile to PION+ETS for a minority concentration of 5%, with a plateau around $s < 0.4$, and a similar P_{ce} profile, which plateaued and decreased until it reached 0 at $s = 0.5$, although with a more central, sharper peak close to $s = 0.1$, compared to the broader, $s = 0.3$ peak calculated by PION+ETS. In this thesis, the case with the lowest minority concentration of 1.0% showed quite central bulk ion heating, with a peak close to $s = 0.1$, and a fraction of the total collisional power going to the ion channel closer to the value obtained with a concentration of 5.0% than with 2.5%. This seemed to indicate that 2$^{\text{nd}}$ ^{4}He harmonic absorption gave rise to bulk ion heating which was concentrated in the plasma center, while fundamental H absorption gave rise to a significantly broader bulk ion heating profile.

In terms of the temperature enhancement, the density scan analysis revealed that the highest minority concentration yielded the most substantial temperature augmentation, approximating a 40% increase. It should be noted that the smallest minority concentration resulted in a final temperature only 0.6 keV less than the largest concentration at the end of the simulation. This enhancement in temperature was attributed to competitive 2$^{\text{nd}}$ ^{4}He harmonic absorption, which significantly contributed to bulk ion heating, thereby influencing the final ion temperature. PION+IMAS simulations in [5] used fixed plasma parameters and therefore did not provide information on the plasma temperature response to the applied heating, so the temperature enhancement could not be calculated. The ion temperature was recorded at

10.9 keV, comparatively lower than the ion temperatures calculated by PION+ETS, which ranged between 12 - 15 keV. The electron temperature stood at 10.2 keV, whereas the final central electron temperatures found in this work lay at 16 keV, independently of the minority concentration.

In conclusion, there was no notable increase in power density absorbed by the resonant ions and SPA when the minority concentration was increased. A very similar $P_{abs,H}$ value was obtained for concentrations in the range of 2.5 - 10%, which agreed with [5] and [6]. However, bulk ion heating did increase with concentration, and a concentration of 10% resulted in much better power equipartition in terms of power going to the ion channel than in the case of 2.5%. This affected the temperature evolution and resulted in a final temperature more than ~ 3 keV higher for a concentration of 10% compared to 2.5%. Special attention had to be paid to the role of competitive 2^{nd} ^{4}He harmonic absorption in both the collisional equipartition and temperature enhancement. Even though a concentration of 10% resulted in the highest final thermal ion temperature, a concentration an order of magnitude lower yielded quite similar results. Maintaining temperature and density gradients without instabilities was crucial for efficient confinement of the plasma. Higher concentrations of minority species could lead to stronger gradients, which might trigger ion-temperature gradient instabilities [26]. Higher minority concentrations could also affect the pressure profile of the plasma, driving pressure-related instabilities such as ballooning modes or kink modes, and enhance anomalous transport processes. This could eventually lead to increased particle and energy losses, disruptions, and reduced plasma confinement times [26]. Therefore, using a H concentration of 1.0% for Scenario 1 as a feasible alternative to 10% should be taken into consideration.

5.1.3 Scenario 2

There was a notable disparity in absorption efficiency when comparing this scenario to Scenario 1. In Scenario 2, absorption was suboptimal for the majority of concentrations, with off-axis, 2^{nd} H harmonic minority absorption being predominant, except for the case with a H concentration of 1.0%. Interestingly, even with a very high SPA nearing 100%, the highest minority concentration of 20% managed to absorb only 63% of the ICRF wave. For the smallest concentration of 1.0%, PION+ETS found a large electron damping of 72%. For a 5.0% H concentration, [5] reported absorption at 48%, a slight reduction from the 53% noted in this work. The power deposition pattern of H was notably more central in [5], with a peak close to $s = 0.2$, contrasting with the $s = 0.5$ peak observed in this work. However, similarly to PION+ETS results, electron damping remained predominantly off-axis. In [5], they noted

how fast ions contributed to a broader and more even radial profile, whilst in Subsection 4.2.3 of this work, it was discussed that the extent of this broadening was constrained by FLR effects, which limited the range of energies available to resonating ions. In [7], they found that at a concentration of 5%, the SPA closely approached 100%. This observation suggested that under these conditions, effective minority heating could be achieved.

Regarding collisional heating, Subsection 4.2.3 highlighted that the decreased average energies of the fast resonating ions in Scenario 2 resulted in a more pronounced bulk ion heating than in Scenario 1. Notably, for the cases with higher minority concentrations, a significant proportion of the ICRF power was channeled towards ion heating, peaking at 58% for a H concentration of 20%. However, a persistent issue remained; the excessive energy of the fast ions impeded their effective contribution to dominant bulk ion heating across all concentrations. PION+IMAS calculations in [5] also revealed the emergence of a high-energy tail in the distribution of the resonating ions, which was a primary factor driving electron heating. The result quoted in [5] for collisional power transferred to background electrons was 87% of the ICRF power for a concentration of 5%, a marked increase from the 61% reported in this work. Additionally, the profile for electron absorption exhibited a notably central peak, contrasting with the $s = 0.5$ peak predicted in this work.

In terms of temperature enhancement, PION+ETS calculated an increase in temperature for all concentrations considered. All concentrations above 1.0% resulted in ion temperatures around $\sim$ 12 keV at the location of the ICRF resonance. The highest ion temperature of 12.3 keV was reached at a minority concentration of 10%. In [5], they reported an ion temperature of 8.2 keV for a minority concentration of 5.0%, compared to the 12.0 keV in this work. Regarding electron temperatures, a concentration of 1.0% registered a maximum electron temperature of 16 keV. In [5], they reported an electron temperature of 15.4 keV for an H concentration of 5%, which was higher than the one reported by PION+ETS at 13.8 keV.

In conclusion, despite a clear increase in both power density absorbed and bulk ion heating with increasing minority concentration, the difference in final ion thermal temperatures was quite small between concentrations, with just over 1 keV separating the lowest and highest temperatures. Regarding power density absorbed, SPA, and bulk ion heating, the largest minority concentration of 20% yielded the highest values. It should be noted that the power density absorbed here was quite low compared to the other two scenarios, although it aligned with the results in [5]. Nonetheless, the smallest concentration of 1.0% resulted in a final ion temperature only $\sim$ 1 keV lower than the 20% case, and in the largest final electron temperature by a margin of more than $\sim$ 4 keV over the 20% case. This again could point towards a feasible alternative in a H concentration of 1.0% for Scenario 2.

5.1.4 Scenario 3

The percentages of the ICRF wave absorbed by the main resonant ion in this scenario were similar to the percentages in Scenario 2, even though the concentrations were two orders of magnitude smaller. A maximum of 65% of the ICRF wave was absorbed by the resonant ^{3}He ions at a concentration of 0.20%, almost triple the power density absorbed at 0.01%, demonstrating that, by adding a few percent of ^{3}He, absorption at the fundamental ^{3}He resonance was greatly improved. When considering the power absorptions at the H and ^{4}He cyclotron resonance layers, the competition between absorption mechanisms resulted in a somewhat smaller percentage of the ICRF wave being absorbed by the resonant ions, with a maximum of 59% of the power being absorbed between the three competing mechanisms for the largest minority concentration. For this case, PION+ETS calculated power density absorption percentages for fundamental ^{3}He, 2nd ^{4}He harmonic, fundamental H and direct electron damping at 27%, 26%, 6%, and 41%, respectively. The presence of Doppler effects, particularly pronounced at lower concentrations, contributed to the broadening of absorption profiles. The research carried out by [7] suggested that ion losses might escalate due to the acceleration of off-axis fast trapped ions.

Comparatively, [8], for a ^{4}He concentration of 8% and 0.4% of ^{3}He, using TORIC, found power density absorption percentages for fundamental ^{3}He, fundamental H and direct electron damping at 69%, 3%, and 28%, respectively. It should be noted that these results were affected by the fact that no power absorption at the ^{4}He IC resonance layer was taken into account. CYRANO was then used by [8] to study this same scenario with the same concentrations as stated above. They calculated percentages for fundamental ^{3}He, 2nd ^{4}He harmonic, fundamental H and direct electron damping at 55%, 0.2%, 14%, and 30%, respectively. When using these same ^{4}He and H concentrations and ignoring the power absorptions at the H and ^{4}He cyclotron resonance layers, PION+ETS calculated almost 70% of the ICRF power being absorbed by the fundamental resonant ^{3}He ions, almost identical to the TORIC results in [8]. The power density absorbed by the ^{3}He ions as calculated by PION+ETS was hence comparable to the other two codes only when the power absorptions at the H and ^{4}He cyclotron resonance layers were not taken into account. When considering the combined power absorbed by all resonant ions, the results from TORIC, CYRANO, and PION+ETS were comparable because the last one predicted a higher 2nd ^{4}He harmonic absorption than the other two codes. The absorption profiles calculated by TORIC and CYRANO were slightly shifted towards the edge of the tokamak as compared to PION+ETS. This deviation could stem from either an altered positioning of the ion-ion hybrid layer or a shift in equilibrium.

It is worth noting that the SPA coefficients in this scenario were significantly lower than in the other two scenarios, with an exception for the largest minority concentration of 0.20%, which yielded the best absorption at 65% with a SPA of 88%. In [7], they reported SPA values ranging between 80% to 90%, combining electron heating and off-axis fundamental ^{3}He heating for a ^{3}He concentration of 0.05%, whilst [8] reported a SPA of 91% for the ^{3}He ions, demonstrating good agreement between PION+ETS, TORIC, and CYRANO.

In terms of collisional heating, for the higher minority concentrations, the average energy of the resonant ions was low enough for bulk ion heating to dominate, with a maximum of 58% of the ICRF power going to bulk ions at a concentration of 0.10%. When considering the absorptions at the H and ^{4}He cyclotron resonance layers, there was dominant bulk ion heating for all concentrations, with a maximum of 70% of the power going to the ion channel for the lowest minority concentration of 0.01%, due to fundamental H and ^{3}He absorption mechanisms dominating over the 2nd ^{4}He harmonic absorption. Therefore, the accelerated ^{3}He and H ions heated bulk ions efficiently because they had a high critical energy and a moderate high-energy tail.

In this scenario, there was no ion temperature enhancement; in fact, there was a decrease in temperature for all concentrations considered at the location of the ICRF resonance, except for the largest concentration of 0.20%. This was expected since the plasma was initially heated by higher ECRH power. In terms of electron temperature, there was an enhancement of the order of $\sim$ 1 keV for all concentrations above 0.01%. However, for this lowest minority concentration, there was an increase of almost $\sim$ 4 keV at the end of the simulation. Nevertheless, it should be noted that for these simulations, a synthetic plasma discharge simulated in ETS at a given time was taken, and further evolved in time using the ICRF heating as simulated by PION. Hence, these results (including the simulated temperature enhancements) were relative to the initial conditions.

To conclude, the largest minority concentration yielded the best results in terms of combined power density absorbed by all competing mechanisms, at around $\sim$ 60%, and in the final thermal ion temperature at 5.9 keV. Bulk ion heating was the lowest for this concentration, but the difference with the lower concentrations was small enough to be irrelevant, with only $\sim$ 5% separating the lowest bulk ion heating from the highest. Combined power densities absorbed by all competing mechanisms of the order of $\sim$ 70%, with a minority concentration twice as large as the one used in this work, was obtained by [8]. Therefore, results seem to agree in showing that a larger ^{3}He concentration yields better absorption and a higher final temperature. However, it should be noted that this temperature enhancement was very small compared to the increase in electron temperature for the lowest minority

concentration. This poses an interesting decision between a large minority concentration and a relatively poor thermal ion temperature enhancement or a very small minority concentration and a significant enhancement in the final electron temperature.

5.1.5 Scenario Comparison and Recommendations

The plasma parameters and ICRF heating schemes in these three scenarios were different, and therefore, a direct comparison was not advisable. However, some conclusions could be drawn from the predictions made by PION+ETS and their comparison to the findings in [5–8]. An overview of the comparison of the ITER scenarios studied in this chapter for the lowest minority concentration is shown in Table 5.1.

For the lowest minority concentration, Scenario 1 showed better combined power density absorbed by all competing mechanisms (77% compared to 28% and 37%) as compared to Scenarios 2 and 3, respectively. It also exhibited a better SPA (85% compared to 77% and 66%) and a higher final thermal ion temperature (13.8 keV compared to 11.0 keV and 5.78 keV) than Scenarios 2 and 3, respectively, and better bulk ion heating (34% compared to 21%) than Scenario 2. However, Scenario 2 showed a better temperature enhancement, both at the resonance (120% compared to 25% and 0%) and at the center of the plasma (140% compared to 35% and 0%) than Scenarios 1 and 3, respectively. In terms of electron temperature, Scenario 2 also exhibited the highest final electron temperature at the ICRF resonance and at the center of the plasma (16.0 keV compared to 12.8 keV and 15.4 keV) and electron temperature enhancement (90% compared to 30% and 30%). Scenario 3 showed the best bulk ion heating (79% compared to 34% and 21%) for a minority concentration below 0.2%.

Table 5.1 *Comparison of the ITER scenarios studied in this chapter for the lowest minority concentration, including Scenario, combined power density absorbed by all competing mechanisms ($P_{abs,ions}$), SPA, percentage of the total collisional power going to the bulk ions (P_{ci}/P_c), final thermal ion temperature ($T_{f,ion}$), ion temperature enhancement (ΔT_{ion}), final electron temperature ($T_{f,e}$) and electron temperature enhancement (ΔT_e)*

Scenario	$P_{abs,ions}$ (MW)	SPA (%)	P_{ci}/P_c (%)	$T_{f,ion}$ (keV)	ΔT_{ion} (%)	$T_{f,e}$ (keV)	ΔT_e (%)
1	77	85	34	13.8	25	12.8	30
2	28	77	21	11.0	120	16.0	90
3	37	66	70	5.78	0	15.4	30

In consideration of the ITER PFPO phase, among the explored ICRF scenarios, Scenario 1 was, in the opinion of the author, the most promising option. This conclusion stemmed from an analysis of the main factors considered in this thesis, i.e. the power absorption, collisional power transfer, and temperature enhancement, and from an examination of relevant plasma dynamics such as H-mode access, impurity control and fast-ion driven instabilities. However, it should be noted that the work presented here functions as a tool that facilitates advancing the research on plasma heating using RF waves. Further work is needed in order to have the capability to provide a deeper analysis of such plasma dynamics as H-mode access or fast ion driven instabilities. The following is an account of said dynamics and some recommendations on the scenario design based on the evidence found in this thesis.

PION+ETS simulations of Scenario 1 revealed a notable efficiency in power absorption, primarily attributed to fundamental H minority damping. This mechanism proved highly effective, showing a steady rise in minority absorption up to 5.0% concentration, with significant power absorption percentages observed. Moreover, competitive 2^{nd} ^{4}He harmonic absorption played a crucial role in enhancing bulk ion heating, further contributing to power absorption efficiency and temperature enhancement.

From the perspective of scenario design, Scenario 1 presented promising prospects for H-mode access. Access to the H-mode in fusion plasmas denotes the transition from a mode of operation with relatively low levels of energy confinement and turbulence known as L-mode, to a state of improved plasma and energy confinement [54]. Turbulence suppression at the plasma edge creates a steep pressure gradient, acting as a barrier against particle and heat escape from the plasma core, thereby enhancing plasma confinement. The efficient power absorption and temperature enhancement observed in Scenario 1 have the potential to lead to more peaked plasma temperature and density profiles, which are favorable conditions for accessing the H-mode regime. However, other factors such as energy confinement time and edge-localized mode (ELM) suppression also play a role in H-mode access and should be taken into account. Moreover, magnetic field configuration and the direction of the magnetic gradient drift of the ions affect the power threshold for triggering an L-H transition [109]. Additionally, earlier modelling done with PION in [110] for an ITER discharge predicts that good bulk ion heating results in enhanced alpha particle heating relative to a given H&CD power input, which can facilitate an easier access to the H-mode regime.

Avoiding the penetration of high-Z impurities into the plasma core, where densities and temperatures are typically higher, stands as a primary concern in ITER plasma discharges. This is due to the fact that radiation losses increase with density and exponentially with atomic number and temperature. Hence, maintaining a clean plasma core devoid of impurities

is imperative to prevent radiative collapse of the discharge [44]. Fast ions play a crucial role in impurity control, primarily through temperature screening. Temperature screening refers to the ability of ions and electrons to inhibit impurity accumulation by peaking their central temperature profile and forming steep temperature gradients, thereby promoting outward impurity flux [111, 112]. However, previous studies [113, 114], taking into account FOW effects, have shown that the most significant impact on temperature screening occurs through the peaking of electron temperature via ion-electron collisions and the flattening of plasma density. Effective impurity control in the plasma core through this peaking of electron temperature yields optimal results when the deposition is central, whereas off-axis deposition experiments exhibit poor impurity control, often dominated by MHD activity and substantial radiation losses, leading to disruption [44]. Therefore, the central deposition observed in Scenario 1, coupled with the dominance of ion-electron collisions over ion-ion collisions, could suggest a promising performance in terms of avoiding impurity accumulation. However, a more detailed examination of the electron temperature profile and of the degree to which the fast ion population contributes to the temperature screening, as compared to the background plasma, would be necessary for a more concrete prediction.

Regarding the fast ion population, the main fast ion quantity studied in this work is the average energy of the fast resonant ions $\langle E_{fast,i} \rangle$. As it can be seen in Table 4.3, the fast ion energies in Scenario 1 are in the range of 459 - 1719 keV, and a trend of increasing $\langle E_{fast,H} \rangle$ with decreasing minority concentration can be seen for the concentrations below 10%. Even though the radial distribution of the fast ion pressure or the energy content are not shown, it is true that those profiles generally follow the shape of the high energy particles contribution to the electron collisional profile P_{ce}, so certain conclusions could be drawn from Figure 4.3. In said figure, it can be seen that there are clear gradients located mid radius, with a sharp drop off at around $s = 0.5$. Gradients in the distribution of fast ions, either spatially or in velocity space, can lead to instabilities [115]. Fast ion-driven instabilities include Alfvén eigenmodes, energetic particle modes (EPMs), and neoclassical tearing modes (NTMs), which can impact plasma confinement, energy transport, and overall plasma stability [116]. It should be noted that, in the case with a minority concentration of 1.0%, the ICRF-accelerated fast H population is reduced due to the presence of competitive damping at the 2$^{\text{nd}}$ harmonic by the ^{4}He ions. This depletion in the fast ion population, combined with the small concentration of the minority species, results in the largest average fast ion energy $\langle E_{fast,H} \rangle$ for this scenario, which could indicate some risk of fast ion-driven instabilities. However, to be able to conclude anything concrete about fast-ion driven instabilities in Scenario 1, more information about the radial and pressure profiles of the fast ions would be needed, which is out of the scope of this thesis and could be developed in future work.

It should also be noted that, in a real experimental setting, achieving precise control over the minority concentration to within 1.0% could pose significant challenges. This limitation could have implications in either of the scenarios considered, as variations in the minority concentration might lead to unpredictable changes in power absorption patterns, could influence collisional power transfer dynamics, potentially altering the distribution of energy between different plasma species, and impact temperature enhancement processes, affecting the overall thermal properties of the plasma. However, the findings in this thesis indicated that even with variations in concentration, some degree of efficiency could still be attained. Notably, the difference in MW of power absorbed between minority concentrations is quite small (c.f. Table 4.3), and there is dominant electron heating independently of the concentration. It is also worth noting that in [117] they developed a real-time control (RTC) scheme to control the ^{3}He concentration, linking the measurement of the ^{3}He density to the opening of a gas injection valve, achieving good control up to a few percent of the ^{3}He concentration in several pulses with different target concentrations.

In summary, Scenario 1 presented an option with good potential for ICRF heating in the ITER PFPO phase, offering promising prospects for H-mode access and impurity transport management, although more research is required to enhance our ability to conduct a more comprehensive analysis of these plasma dynamics. While challenges in achieving precise control over minority concentration may exist, results suggested that viable performance outcomes are achievable, laying a solid foundation for further experimental validation.

5.2 Conclusion and Future Steps

This thesis presented the development and assessment of theoretical models for ICRF at JET, AUG, and ITER, with a special focus on the latter. ICRF heating has been a well-established technique for providing auxiliary heating in contemporary tokamak plasmas and is anticipated to be a primary method for heating in ITER and future reactor plasmas. In order to predict the effectiveness of ICRF heating in upcoming machines, it was crucial to perform self-consistent, time-dependent, predictive simulations that could provide a better understanding of the dynamics of the confined plasma when ICRF heating is applied. On this basis, this thesis offered valuable insights into optimizing plasma performance through various ICRF heating schemes. The results presented in this thesis can serve as a guide for maximizing absorption, bulk ion heating, and final temperature by appropriately configuring the ICRF heating scheme.

The heating code PION, integrated into the transport workflow ETS, was utilized to examine the power deposition, collisional equipartition, and the evolution of ion and electron temperatures when applying ICRF heating to ITER non-active plasmas. PION+ETS was also employed to analyze a JET baseline scenario and an AUG D plasma, demonstrating the feasibility of integrating PION+ETS into currently operational reactors. Special focus was given to bulk ion heating and temperature enhancement, along with comparing the results obtained in this thesis to those in [5–8]. The presence of ICRF physics phenomena such as Doppler effects, FOW effects, FLR effects and fast-ion tails were examined, and their effects were discussed.

In terms of power density absorbed, SPA, and final thermal ion temperature, Scenario 1 emerged as the most favorable option compared to the other two ITER scenarios, yielding satisfactory outcomes even with the smallest minority concentration of 1.0%. Scenario 2 showcased the highest electron temperature and the most significant thermal ion temperature enhancement, presenting an intriguing possibility of utilizing only a minority concentration of 1.0% as well. Lastly, the three-ion-scheme in Scenario 3 demonstrated the best bulk ion heating for a minority concentration below 0.2%. FOW and FLR effects manifested in all simulations, notably impacting Scenario 2, where FLR effects weakened the wave-particle interaction at certain energies, thereby limiting the range of energies that the resonating ions could attain. This limitation arose because the primary absorption mechanism in Scenario 2 was 2^{nd} H harmonic damping, underscoring the importance of FLR effects.

Overall, fundamental minority H heating in ^{4}He plasma at 2.65 T emerged as a promising choice for ICRF heating during the ITER PFPO phase, with encouraging potential for H-mode access and impurity transport control, even though a deeper analysis of these dynamics is outside the scope of the research carried out in this thesis, as well as good performance in terms of power absorption, SPA and temperature enhancement.

Future steps would focus primarily on developing a better understanding of the available transport modelling tools in the IMAS framework, and on gaining the capabilities to substitute the simplified, first-principles transport model used in this work by a more consistent transport model, so that the effect of ICRF heating on the temperature and density transport can be studied. A thorough benchmarking could also be performed, comparing the results obtained here for the JET and AUG simulations to experimental results. Finally, PION+ETS could be applied to more ITER scenarios to forward the understanding of the effect of ICRF heating on the evolution of the plasma parameters, and extend the range of scenarios to the active, D-T phase.

References

[1] L. G. Eriksson *et al.* A model for calculating ICRH power deposition and velocity distribution. *Physica Scripta*, 52:70, 1995.

[2] L. G. Eriksson *et al.* Comparison of time dependent simulations with experiments in ion cyclotron heated plasmas. *Nuclear Fusion*, 33:1037, 1993.

[3] D. P. Coster *et al.* The European Transport Solver. *IEEE Transactions on Plasma Science*, 38:2085, 2010.

[4] D. Kalupin *et al.* Construction of the European Transport Solver under the European Integrated Tokamak Modelling Task Force. *35th EPS Conference on Plasma Physics*, 32:5027, 2008.

[5] I. L. Arbina *et al.* First applications of the ICRF modelling code PION in the ITER Integrated Modelling and Analysis Suite. *46th EPS Conference on Plasma Physics*, 59:1079, 2019.

[6] E. Lerche *et al.* ICRF scenarios for ITER's half-field phase. *AIP Conference Proceedings*, 1406:1, 2011.

[7] M. Schneider *et al.* ICRF heating schemes for the ITER non-active phase. *EPJ Web of Conferences*, 157:03046, 2017.

[8] M. Schneider. Private Communication. *ITER Organization*, 2023.

[9] J. Rockström *et al.* Planetary boundaries: Guiding human development on a changing planet. *Science*, 347(6223):1259855, 2015.

[10] L. Personn *et al.* Outside the safe operating space of the planetary boundary for novel entities. *Environmental Science Technologies*, 56(3):1510–1521, 2022.

[11] K. Richardson *et al.* Earth beyond six of nine planetary boundaries. *Science Advances*, 9(37):2458, 2023.

[12] D. A. McKay *et al.* Exceeding 1.5°C global warming could trigger multiple climate tipping points. *Science*, 377:7959, 2022.

[13] IPCC. Climate Change 2023: Synthesis Report. Contribution of Working Groups I, II and III to the Sixth Assessment Report of the Intergovernmental Panel on Climate Change. *Intergovernmental Panel on Climate Change*, 2023.

[14] International Energy Agency. CO2 Emissions in 2022. *International Energy Agency*, 2022.

[15] World Nuclear Association. Carbon Dioxide Emissions From Electricity. *World Nuclear Association*, 2022.

[16] G. D'Alisa *et al. Degrowth: A Vocabulary for a New Era*. Routledge, 2014.

[17] F. Demaria *et al.* What is Degrowth? From an activist slogan to a social movement. *Environ. Values*, 22(2):191–215, 2013.

[18] V. Fournier *et al.* Escaping from the economy: the politics of degrowth. *Int. J. Sociol. Soc. Policy*, 28(11/12):528–45, 2008.

[19] D. H. Meadows *et al.* WW III. 1974. The Limits to Growth: A Report for the Club of Rome's Project on the Predicament of Mankind. *New York: Universe Books*, 1974.

[20] G. Kallis *et al.* In defence of degrowth. *Ecol. Econ.*, 70(5):873–80, 2011.

[21] D. W. O'Neill *et al.* A good life for all within planetary boundaries. *Nat. Sustain.*, 1(2):88–95, 2018.

[22] G. Kallis *et al.* Research on degrowth. *Annual Review of Environment and Resources*, 43:291–316, 2018.

[23] J. P. Freidberg. *Theory of Fusion Plasmas*. Cambridge University Press, 2007.

[24] D. Bodansky. *Nuclear Energy: Principles, Practices, and Prospects*. Springer, 2005.

[25] D. Bodansky. *Nuclear energy*. Springer, 2004.

[26] J. Wesson *et al. Tokamaks*. Oxford University Press, 2018.

[27] C. Leadbeater-Hart. Introducing JET Decommissioning and Repurposing Project. *JET*, 2024.

[28] P. H. Rebut *et al.* The Joint European Torus: installation, first results and prospects. *Nuclear Fusion*, 25:9, 1985.

[29] ITER team. ITER research plan within the staged approach. *ITER*, 2018.

[30] M. Keilhacker. The ASDEX divertor tokamak. *Nuclear Fusion*, 25:9, 1985.

[31] First Light Fusion Ltd. First Light Fusion. https://firstlightfusion.com/, 2024. Accessed on: May 6, 2024.

[32] General Fusion. General Fusion. https://generalfusion.com/, 2024. Accessed on: May 6, 2024.

[33] Helion Energy. Helion Energy. https://www.helionenergy.com/, 2024. Accessed on: May 6, 2024.

[34] D. Kirtley *et al.* Fundamental Scaling of Adiabatic Compression of Field Reversed Configuration Thermonuclear Fusion Plasmas. *Journal of Fusion Energy*, 42, 2023.

[35] R. Hameed *et al.* Reaching to a featured formula to deduce the energy of the heaviest particles producing from the controlled thermonuclear fusion reactions. *Journal of Physics: Conference Series*, 1003:012076, 2018.

[36] D. Van Eester *et al.* A fast tool for ICRH NBI modelling within the EU-IM framework. *Journal of Plasma Physics*, 87:2, 2021.

[37] G. McCracken *et al. Fusion*. Elsevier Inc., 2012.

[38] S. Pfalzner. *An Introduction to Inertial Confinement Fusion*. Taylor and Francis Group, 2006.

[39] K. Miyamoto. *Controlled fusion and plasma physics*. Taylor and Francis Group, 2007.

[40] A.G. Ghiozzi *et al.* Modeling of frequency-sweeping Alfvén modes in the TJ-II stellarator. *Nuclear Fusion*, 64(3):036005, 2024.

[41] M. Wakatani. *Stellarator and heliotron devices*. Oxford University Press, 1998.

[42] A. B. Zylstra *et al.* Experimental achievement and signatures of ignition at the national ignition facility. *Phys. Rev. E*, 106:025202, 2022.

[43] E. Stallard. UK's nuclear fusion site ends experiments after 40 years. *BBC News*, 2023.

[44] D. Gallart. Computational Analysis of Ion Cyclotron Resonance Frequency Heating for JET Experiments . *PhD Thesis - Univerity Politechnique Catalunya*, 2021.

[45] EUROfusion News. Breaking New Ground: JET Tokamak's Latest Fusion Energy Record Shows Mastery of Fusion Processes. *EUROfusion News*, 2024.

[46] C. Maggi. Foreword to the Nuclear Fusion Special Issue of Papers Presenting Results from the JET Tritium and Deuterium / Tritium Campaign. *Nuclear Fusion*, 63:11, 2023.

[47] L. R. Grisham *et al.* Recent improvements to the ITER neutral beam system design. *Fusion Engineering and Design*, 87:11, 2012.

[48] J. P. Freidberg. *Plasma physics and fusion energy*. Cambridge University Press, 2010.

[49] G. Gantenbein *et al.* Experimental Investigations and Analysis of Parasitic RF Oscillations in High-Power Gyrotrons. *IEEE Transactions on Plasma Science*, 38(6):1168–1177, 2010.

[50] D. M. Pozar. *Microwave Engineering*. John Wiley & Sons Inc, 2004.

[51] S. Koizumi *et al.* Physics and Applications of CVD Diamond. 2008.

[52] S. Porro *et al.* Surface analysis of CVD diamond exposed to fusion plasma. *Diamond and Related Materials*, 19(7):818–823, 2010.

[53] J.A. Pittard *et al.* Deuterium retention in CVD diamond: Combined experimental and computational study. *Fusion Engineering and Design*, 188:113403, 2023.

[54] T. H. Stix. *Waves in plasmas*. Plasma Physics Laboratory, Princeton University, 1990.

[55] J. R. Myra *et al.* Radio frequency wave interactions with a plasma sheath: The role of wave and plasma sheath impedances. *Physics of Plasmas*, 26(5):052503, 2019.

[56] J. Marki *et al.* Sheath heat transmission factors on TCV. *Journal of Nuclear Materials*, 363-365:382–388, 2007.

[57] D. F. H. Start *et al.* Bulk ion heating with ICRH in JET DT plasmas. *Nuclear Fusion*, 39:3, 1999.

[58] Ye. O. Kazakov *et al.* A new ion cyclotron range of frequency scenario for bulk ion heating in deuterium-tritium plasmas: How to utilize intrinsic impurities in our favour. *Physics Of Plasmas*, 22:082511, 2015.

[59] Ye. O. Kazakov *et al.* On resonant ICRF absorption in three-ion component plasmas: a new promising tool for fast ion generation. *Nuclear Fusion*, 55:032001, 2015.

[60] Ye. O. Kazakov *et al.* Effect of impurities on the transition between minority ion and mode conversion ICRH heating in (^{3}He)–H tokamak plasmas. *Nuclear Fusion*, 53:053014, 2013.

[61] J. A. Bittencourt. *Fundamentals of Plasma Physics*. Springer, 2004.

[62] R. Dumont. Waves in plasmas: Lecture notes. *CEA, IRFM*, page 117, 2017.

[63] K.G. Budden. *Radio Waves in the Ionosphere*. Cambridge University Press, 1961.

[64] L. G. Eriksson *et al.* Monte Carlo operators for orbit-averaged Fokker–Planck equations. *Physics of Plasmas*, 1(2):308–314, 1994.

[65] D. Anderson *et al.* Distortion of ion velocity distributions in the presence of ICRH: A semi-analytical analysis. *Nuclear Fusion*, 27(6):911–919, 1987.

[66] D. F. H. Start *et al.* D-T Fusion with Ion Cyclotron Resonance Heating in the JET Tokamak. *American Physical Society*, 80:4681, 1998.

[67] D. F. H. Start *et al.* Bulk ion heating with ICRH in JET DT plasmas. *Nuclear Fusion*, 39:321, 1999.

[68] M. J. Mantsinen *et al.* Analysis of bulk ion heating with ICRH in JET high-performance plasmas. *Plasma Physics and Controlled Fusion*, 41:843, 1999.

[69] M. J. Mantsinen *et al.* Evidence for regions of nearly suppressed velocity space diffusion caused by finite Larmor radius effects during ICRF heating. *Nuclear Fusion*, 39:459, 1999.

[70] M. J. Mantsinen *et al.* First observation of pT fusion in JET tritium plasmas with ICRF heating of protons. *Nuclear Fusion*, 41:1815, 1999.

[71] L.-G. Eriksson *et al.* ICRF heating of JET plasmas with the third harmonic deuterium resonance. *Nuclear Fusion*, 38:265, 1998.

[72] L.-G. Eriksson *et al.* Theoretical analysis of ICRF heating in JET DT plasmas. *Nuclear Fusion*, 39:337, 1999.

[73] S. E. Sharapov *et al.* Stability of alpha particle driven Alfvén eigenmodes in high performance JET DT plasmas. *Nuclear Fusion*, 39:373, 1999.

[74] A. Salmi *et al.* JET experiments to assess the clamping of the fast ion energy distribution during ICRF heating due to finite Larmor radius effects. *Plasma Physics and Controlled Fusion*, 48:717, 2006.

[75] M. J. Mantsinen *et al.* Bulk ion heating with ICRF waves in tokamaks. *AIP Conference Proceedings*, 1689:030005, 2015.

[76] M. J. Mantsinen *et al.* Third harmonic ICRF heating of deuterium beam ions on ASDEX Upgrade. *43rd EPS Conference on Plasma Physics*, P1.035, 2016.

[77] S. E. Sharapov *et al.* The effects of electron cyclotron heating and current drive on toroidal Alfvén eigenmodes in tokamak plasmas. *Plasma Physics and Controlled Fusion*, 60:014026, 2017.

[78] J. Galdon-Quiroga *et al.* Velocity space resolved absolute measurement of fast ion losses induced by a tearing mode in the ASDEX Upgrade tokamak. *Nuclear Fusion*, 58:036005, 2018.

[79] M. J. Mantsinen *et al.* Modelling of ICRF heating in ASDEX Upgrade discharges with pure wave heating relevant to the ITER baseline scenario. *45th EPS Conference on Plasma Physics*, P1.1072, 2018.

[80] J. Manyer *et al.* Modelling of dual-frequency ICRF heating in ASDEX Upgrade discharges relevant to the ITER baseline scenario. *47th EPS Conference on Plasma Physics*, P5.1055, 2021.

[81] M. J. Mantsinen *et al.* Analysis of combined fast wave current drive and neutral beam injection in the DIII-D tokamak. *Physics of Plasmas*, 9:1318, 2002.

[82] L.-G. Eriksson *et al.* On the role of ion heating in ICRF heated discharges in Tore Supra. *Nuclear Fusion*, 41:91, 2001.

[83] Equipe Tore Supra and A. Becoulet *et al.* Heating and Current Drive System for Tore Supra Steady-State Operation. *J. Plasma Fusion Resesearch SERIES*, 3:51, 2000.

[84] D. Van Eester *et al.* Simple 1D Fokker–Planck modelling of ion cyclotron resonance frequency heating at arbitrary cyclotron harmonics accounting for Coulomb relaxation on non-Maxwellian populations. *Plasma Physics and Controlled Fusion*, 53:092001, 2011.

[85] D. Kalupin *et al.* Numerical analysis of JET discharges with the European Transport Simulator. *Nuclear Fusion*, 53:12, 2013.

[86] A. C. A. Figueiredo *et al.* Modelling of JET hybrid scenarios with the European Transport Solver. *40th EPS Conference on Plasma Physics*, 2:163, 2013.

[87] G. L. Falchetto *et al.* Multi-machine analysis of EU experiments using the EUROfusion Integrated Modelling (EU-IM) framework. *46th EPS Conference on Plasma Physics*, 1:1081, 2019.

[88] P. Strand *et al.* Towards a Predictive Modelling Capacity for DT Plasmas: European Transport Simulator (ETS) Verification and Validation. *27th IAEA Fusion Energy Conference*, 50:38, 2018.

[89] L. G. Eriksson *et al.* Applying the ICRF code PION to JET data. *JET Joint Undertaking*, 43, 1999.

[90] T. Hellsten *et al.* Power deposition for ion cyclotron heating in large tokamaks. *Nuclear Fusion*, 28:285, 1988.

[91] T. Hellsten *et al.* Proceedings of the Joint Varenna-Lausanne International Workshop, Chexbres. *Theory of Fusion Plasmas (Editrice Compositori for Societa italiana di fisica)*, 1988.

[92] T. Hellsten *et al.* A modelling scheme for the direct electron heating profiles during ion cyclotron resonance heating. *Nuclear Fusion*, 29:2165, 1989.

[93] D. Anderson *et al.* Bulk ion heating with ICRH in JET D-T plasmas. *Plasma Physics and Controlled Fusion*, 29:891, 1987.

[94] S. Succi *et al.* Computational models for wave-particle interactions. *Computer Physics Communications*, 40:137, 1986.

[95] The Kepler Project. *https://kepler-project.org/users/documentation.html*, 2008.

[96] P. U. Lamalle. Nonlocal theoretical generalisation and tridimensional numerical study of the coupling of an ICRH antenna to a tokamak plasma. *PhD Thesis - Université de Mons*, 1994.

[97] D. Van Eester *et al.* Simple 1D Fokker-Planck modelling of ion cyclotron resonance frequency heating at arbitrary cyclotron harmonics accounting for Coulomb relaxation on non-Maxwellian populations. *Plasma Physics and Controlled Fusion*, 53:9, 2011.

[98] F. L. Hinton *et al.* Theory of plasma transport in toroidal confinement systems. *Reviews of Modern Physics*, 48:239, 1976.

[99] T. S. Hahm. Nonlinear gyrokinetic equations for tokamak microturbulence. *The Physics of Fluids*, 31:2670, 1998.

[100] G. V. Pereverzev *et al.* ASTRA - Automated System for TRansport Analysis in a Tokamak. *IPP Report*, 2002.

[101] C. Xu *et al.* Ramp-Up-Phase Current-Profile Control of Tokamak Plasmas via Nonlinear Programming. *IEEE Transactions on Plasma Science*, 38:2, 2010.

[102] T. H. Stix. Heating of toroidal plasmas by neutral injection. *Plasma Physics*, 14:367, 1972.

[103] M. Porkolab *et al.* Recent progress in ICRF physics. *Plasma Physics and Controlled Fusion*, 40:A35, 1998.

[104] L. Garzotti *et al.* Scenario development for D–T operation at JET. *Nuclear Fusion*, 59:076037, 2019.

[105] O. Asunta *et al.* Modelling neutral beams in fusion devices: Beamlet-based model for fast particle simulations. *Computer Physics Communications*, 188:33, 2015.

[106] D. Gallart *et al.* Modelling of JET hybrid plasmas with emphasis on performance of combined ICRF and NBI heating. *Nuclear Fusion*, 58:10, 2018.

[107] D. Van Eester *et al.* A variational principle for studying fast-wave mode conversion. *Plasma Physics and Controlled Fusion*, 40:11, 1998.

[108] M. Brambilla. Numerical simulation of ion cyclotron waves in tokamak plasmas. *Plasma Physics and Controlled Fusion*, 41:1, 1999.

[109] E. J. Doyle *et al.* Plasma confinement and transport. *Nuclear Fusion*, 47(6):S18, 2007.

[110] J. Jacquinot and the JET team. Deuterium-tritium operation in magnetic confinement experiments: results and underlying physics. *Plasma Physics and Controlled Fusion*, 41(3A):A13, 1999.

[111] F. J. Casson *et al.* Theoretical description of heavy impurity transport and its application to the modelling of tungsten in JET and ASDEX upgrade. *Plasma Physics and Controlled Fusion*, 57:014031, 2015.

[112] M. Goniche *et al.* Ion cyclotron resonance heating for tungsten control in various JET H-mode scenarios. *Plasma Physics and Controlled Fusion*, 59:055001, 2017.

[113] E. Lerche *et al.* Optimization of ICRH for core impurity control in JET-ILW. *Nuclear Fusion*, 56:036022, 2016.

[114] F. Casson *et al.* Predictive multi-channel flux-driven modelling to optimise ICRH tungsten control in JET. *Nuclear Fusion*, 60(6):066029, 2020.

[115] W. Kerner *et al.* Theory of Alfvén eigenmode instabilities and related alpha particle transport in JET deuterium-tritium plasmas. *Nuclear Fusion*, 38(9):1315–1332, 1998.

[116] W. Heidbrink. Basic physics of Alfvén instabilities driven by energetic particles in toroidally confined plasmas. *Physics of Plasmas*, 15(5):055501, 2008.

[117] D. Van Eester *et al.* Recent ^{3}He Radio Frequency Heating Experiments on JET. 694, 12 2003.